# Accurate and Precise Displacement Estimation for Ultrasound Elastography

Morteza Mirzaei

A Thesis
In the Department
of
Electrical and Computer Engineering

Presented in Partial Fulfillment of the Requirements
For the Degree of
Doctor of Philosophy (Electrical and Computer Engineering) at
Concordia University
Montréal, Québec, Canada

July 2021

# Concordia University
School of Graduate Studies

This is to certify that the thesis prepared

By: **Morteza Mirzaei**
Entitled: **Accurate and Precise Displacement Estimation for Ultrasound Elastography**

and submitted in partial fulfillment of the requirements for the degree of

**Doctor of Philosophy (Electrical Engineering)**

complies with the regulations of this University and meets the accepted standards with respect to originality and quality.

Signed by the final examining commitee:

Dr. Ramin Sedaghati _____ Chair

Dr. Robert Rohling _____ External Examiner

Dr. Marta Kersten _____ External to Program

Dr. Habib Benali _____ Examiner

Dr. Shahin Hashtrudi Zad _____ Examiner

Dr. Hassan Rivaz _____ Thesis supervisor

Dr. Amir Asif _____ Thesis Supervisor

Approved _____
Dr.Wei-Ping Zhu, Graduate Program Director

July 6, 2021

Date of Defense

Dr. Mourad Debbabi, Dean, Engineering and Computer Science

# Abstract


## Accurate and Precise Displacement Estimation for Ultrasound Elastography

**Morteza Mirzaei, Ph.D.**
**Concordia University, 2021**

Elastography is a technique for detecting pathological tissue alterations by extracting mechanical properties of the tissue. It can be performed using different imaging modalities, including magnetic resonance imaging and ultrasound. Unlike biopsy that is invasive and considers a small portion of tissue, elastography is a non-invasive technique that interrogates a larger part of the tissue and reduces the probability of missing abnormalities. UltraSound Elastography (USE) is an approach for detecting mechanical properties of tissue by using ultrasound imaging. Ultrasound as an imaging tool has emerged in the latter half of the 20th century and has become one of the most popular imaging modalities. The main advantages of ultrasound imaging lie in its noninvasive nature, low cost, convenience, and wide availability. USE may help in early diagnosis which substantially increases the success probability of treatment. In recent years, USE has been explored for several clinical applications including ablation guidance and monitoring, differentiating benign thyroid nodules from malignant ones and breast lesion characterization. Surgical treatment of liver cancer, assessment of non-alcoholic fatty liver disease, assessment of fibrosis in chronic liver diseases, detecting prostate cancer, differentiating abnormal lymph nodes in benign conditions and brain tumor surgery are other relevant clinical applications of USE.

An important challenging step for USE is Time Delay Estimation (TDE) between pre- and post-deformed tissue. TDE is an ill-posed problem since the 2D displacement of one sample cannot be uniquely calculated based on its intensity. Moreover, presence of noise due to speckles, out-of-plane movement, blood flow and other biological motions affect the accuracy of TDE. The other limiting factors for TDE are low resolution of ultrasound data, low sampling rate and lack of carrier signal in the lateral direction. In this thesis, we propose high level techniques for increasing the accuracy and preciseness of the estimated displacement.

# Acknowledgments

First and foremost, I would like to thank my dear supervisors, Dr. Hassan Rivaz and Dr. Amir Asif, for their exceptional technical supervision and excellent cooperation during my research. I have learned a lot, and it is not limited just for academic career. I greatly appreciate you for all your support and I thank you very much for all your guidance throughout my studies at Concordia University.

I deeply express my gratitude to the committee members, Dr. Habib Benali, Dr. Marta Kersten, Dr. Shahin Hashtrudi Zad and Dr. Robert Rohling, for evaluating this dissertation and their thoughtful feedback.

My sincere thanks goes to my lovely parents and my siblings for their emotional support, although we were mostly away from each other.

# Contents

# List of Figures

# List of Tables

# List of Abbreviations

**USE** UltraSound Elastography

**RF** Radio Frequency

**NCC** Normalized Cross Correlation

**STNCC** Spatial Temporal Normalized Cross Correlation

**CNCC** Channel data Normalized Cross Correlation

**GLUE** GLobal Ultrasound Elastography

**OVERWIND** tOtal Variation rEgularization and WINDow-based time-delay estimation

**CGLUE** Channel data for GLobal Ultrasound Elastography

**LSQ** Least SQuare

**VSSA** Virtual Source Synthetic Aperture

**MUSCULAR** Mechanical-based qUasi-StatiC Ultrasound eLAstogRaphy

**SA** Synthetic Aperture

**TDE** Time Delay Estimation

**DP** Dynamic Programming

# Chapter 1

# Introduction and Literature Review

Audible range of human-being is between 20 Hz to 20 kHz, and any sound wave above 20 kHz is called an ultrasound wave [3]. For medical diagnostic applications, a major advantage accrues from the ability of ultrasound to penetrate biological tissue and to return signals that contain information about tissue's acoustic structure [4]. In the following section, the basic principles of medical ultrasound imaging are summarized.

## 1.1 Ultrasound Imaging

Ultrasound imaging is one of the most commonly used imaging modalities since it is inexpensive, safe, convenient and widely available including at the bedside. An ultrasound machine is shown in Fig. 1.1. For ultrasound wave, electrical excitation of a crystal generates vibration with high frequency. More specifically, crystals transform the electrical exciting signal into a mechanical movement. The same transducer receives the back scattered wave and converts it to electrical signals.

Acoustic waves in general are described as propagating energy in 3D space. For the purposes of analysis, this propagation is categorized into two fundamental modes: longitudinal and transverse, that are shown in Fig. 1.2. In longitudinal waves, the direction of wave propagation is parallel to particle displacement. However, for transverse waves, the direction of particle displacement is perpendicular to energy flow [1]. In soft tissues, couplings between particles in the direction of wave propagation are higher than those in the transverse direction, which supports longitudinal waves with high velocities and attenuates transverse particle movements [5]. However, recent developments in USE use shear wave to extract stiffness of tissue. By receiving reflected pulse and mapping time-of-arrival to round-trip distance, an ultrasound image is generated. If the surface of discontinuity is large, the wave reflects in a single path with an angle equal to angle of incidence as shown in Fig. 1.3.

In the human body, the discontinuities are often small (compared to the wavelength of the waves), which causes scattering. Scattering is a more complex reflection

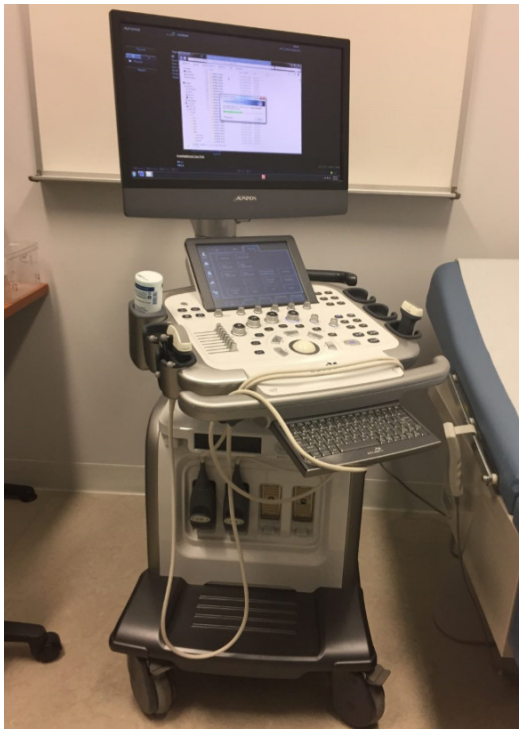

(a)

Figure 1.1: Ultrasound machine at the PERFORM Centre.

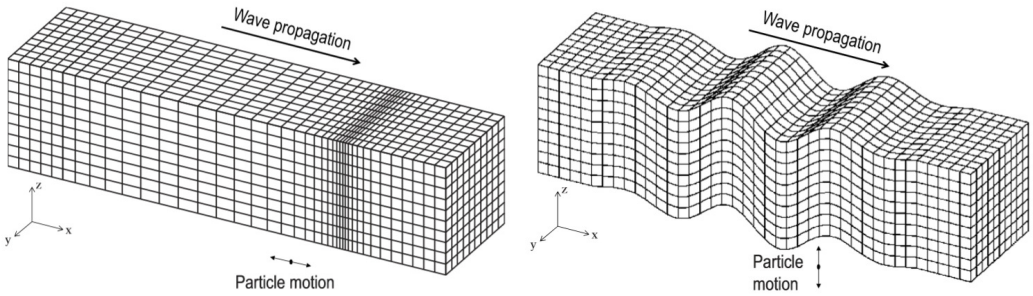


(a) (b)

Figure 1.2: Ultrasound wave propagation in tissue (from [1]).

of ultrasonic waves in which the reflection is not in a single path as shown in Fig. 1.4. For discontinuities with dimensions close to the wavelength, reflections are non-uniform and cannot be modeled. However, for objects in tissue smaller than about a tenth of the wavelength of the ultrasound energy, the wave reflects equally in all directions [5]. Another problem of imaging is attenuation wherein energy is absorbed or refracted as ultrasound propagates. As the transmitted pulse propagates, echoes are scattered in the tissue, and detected by the transducer elements. Beamforming the signals by applying appropriate time-delays to recorded data of each element and averaging the detected signals allows localization of the scattering structures [6].

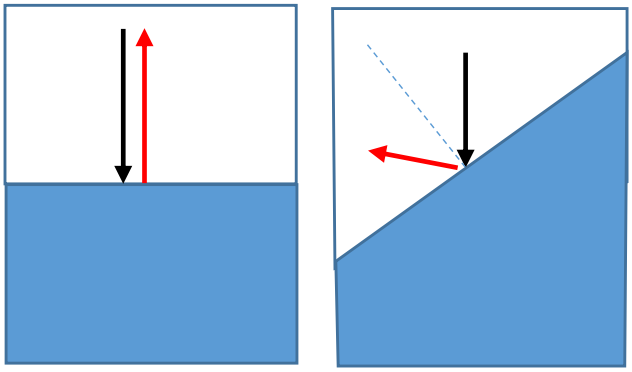

Figure 1.3: Specular reflection.

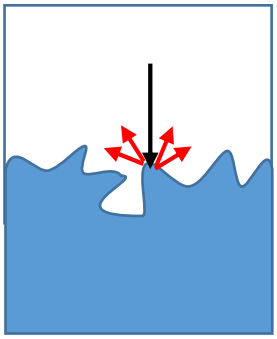

Figure 1.4: Scattering.

The raw echo data that is received by transducer is called RF data. It is shown that for an application such as USE, utilizing RF data significantly improves results.

## 1.2 Ultrasound Elastography

USE techniques have received substantial attention in recent years due to their ability in detecting bio-mechanical tissue alterations non-invasively, which can substantially improve the capabilities of ultrasound imaging in both diagnosis and image guided interventions. Pathological changes are generally known to be correlated with changes in tissue stiffness. Many cancers, such as scirrhous carcinoma of the breast, appear as extremely hard nodules [7]. It is also worth noting that some lesions like prostate or breast tumors do not possess echogenic properties (i.e. ability to reflect the the ultrasound wave), which makes them ultrasonically detectable. However, they have different stiffness than normal tissue. Since the echogenicity and the stiffness of tissue are generally uncorrelated, it is expected that imaging tissue stiffness or strain will provide new information that is related to pathological tissue structure [7].

Different classifications for USE are proposed in the literature, however, it can be broadly grouped into dynamic and quasi-static USE. How ever, displacement estimation is the main step for both classes. In both classes, The scatterers in tissue are displaced by external stimuli or internal forces, and shear modulus or Young's modulus can be calculated by estimating tissue motion.

### 1.2.1 Dynamic Methods

Dynamic methods, such as shear wave imaging (SWI) [13, 14] and acoustic radiation force imaging (ARFI) [15, 16], use Acoustic Radiation Force (ARF) to generate displacement in the tissue. Transient USE is another common dynamic method in which low-frequency vibrations are applied to the tissue [17]. Internal or endogenous deformations that are often created by the pumping action of the heart are the other method of deformation. The mechanical properties of the cardiac tissue can be estimated from the velocity of this wave [10–12]. These methods can be used to estimate quantitative mechanical properties of tissue. For ARFI, the impulsive force generates a localized displacement of the tissue. By removing the force, the tissue relaxes to its original position. A number of parameters can be used to characterize the response of the tissue, including the peak displacement, the time it takes to reach peak displacement, and the recovery time. The excitation is performed at one location and the response is measured, and then the excitation line is translated and the response is measured. The alternations of stimulation and detection are performed to construct images of the tissue response. This process can be parallelized to push and track the tissue displacements simultaneously along multiple lines of sight.

In the case of SWI, mechanical generation of shear waves and measurement of wave propagation should be considered. Different methods are employed to generate shear wave, then by measuring its velocity, mechanical properties of tissue are extracted.

### 1.2.2 Quasi-static Methods

For quasi-static USE, excitation is performed by simply pressing an ultrasound probe against tissue [18,19], which can be done by utilizing a robotic arm [20,21] or a handheld probe (i.e. free-hand palpation) [22,23]. Another approach is to use the ablation probe to generate displacements [24].

The main reason for the name of quasi-static is the low velocity of the deformation such that static mechanics can be assumed [19]. Free-hand quasi-static USE does not require additional hardware other than an ultrasound machine, and as such, is very convenient and has even been applied in image-guided surgery [25] and radiotherapy [26]. Compared to SWI and ARFI, displacements in quasi-static USE are usually substantially larger, leading to a higher signal to noise ratio in displacement estimation. The disadvantage is that it cannot readily generate quantitative tissue properties and an inverse problem approach is applied to infer quantitative properties in tissue [8, 9, 27, 28].

### 1.2.3 Displacement Estimation

The problem of displacement estimation is ill-posed since the intensity of one sample provides one equation. Most biological tissues are nearly incompressible, i.e., the volume of the tissue does not change by compressing it. Therefore, axial compression will also lead to lateral and out of plane deformations. Even after neglecting out of plane motion, each sample moves in two directions which results in two unknown variables, and two unknowns cannot be uniquely determined from one equation [29]. To make the problem a well-posed one, different methods for quasi-static USE are proposed in the literature, which in turn can be broadly categorized into window-based and regularized optimization-based approaches. Recently, artificial intelligence is also exploited in displacement estimation. In [30–32], the general modes of deformation are extracted by Principal Component Analysis (PCA) and a network is trained to estimate the displacement approximately 10 times faster than [33] as a regularized optimization-based approach. Deep neural networks and more specifically Convolutional Neural Network (CNN) models have been also successfully trained for displacement estimation [34–36] and USE [37, 38].

### 1.2.4 Clinical Application

In recent years, USE has been explored for several clinical applications, including ablation guidance and monitoring [39], differentiating benign thyroid nodules from malignant ones [40–42] and breast lesion characterization [43–45]. Surgical treatment of liver cancer [46–48], assessment of non-alcoholic fatty liver disease [49], assessment of fibrosis in chronic liver diseases [50,51], detecting prostate cancer [52,53], differentiating abnormal lymph nodes in benign conditions [54] and brain tumor surgery [55,56] are other relevant clinical applications of USE.

### 1.2.5 Thesis Statement

USE is based on deforming the tissue and estimating tissue motion between pre- and post-compressed ultrasound data. Signal de-correlation and low resolution of ultrasound data in addition to limited number of samples and lack of carrier signal in lateral direction are the main challenges of estimating displacement. We have developed multiple techniques to address some of theses limitations.

In Chapter 2, a 3D window-based technique is proposed. Window-based tracking methods are one of the most popular tracking techniques that assume displacements of spatially neighboring samples are the same and look for a similar window in the other image. In traditional window-based methods, 2D spatial windows were considered and information of spatially neighbors was utilized. In this chapter, we use 3D windows to benefit from additional information made available by including samples in the third dimension. In this chapter, two approaches named STNCC and CNCC are proposed. In STNCC, the third dimension is temporally neighboring samples and in

CNCC time-delayed pre-beam-formed data that is collected by neighboring channels are utilized as the third dimension.

In Chapter 3, OVERWIND time-delay estimation method as a regularized optimization-based method is proposed. In OVERWIND, a cost function containing two parts is introduced for optimal displacement estimation. In the first part of the proposed cost function, the difference of two images as pre- and post-compressed RF data are penalized. By assuming that neighboring samples have the same displacement, small windows are considered around each sample and all samples in these windows are forced to have the same displacement in the pre- and post-compression RF data. Therefore, this method increases robustness against noise by utilizing information from neighboring samples. The second term of cost function deals with regularization which penalizes displacement of neighbor samples. Herein, we use L1 norm regularization which assigns a smaller penalty to discontinuities compared to the more commonly used L2 norm regularization. This modification adds nonlinear terms to the cost function, and therefore, we use iterative methods to optimize the cost function.

In Chapter 4, CGLUE is proposed for USE. The novelty of CGLUE is using time-gain and time delay corrected pre-beamformed channel data instead of RF data. The channel data contains more information than RF data which intuitively informs that their comparison results in better displacement estimation than RF data. We also prove that utilizing channel data in data term decreases bias and variance of error. In Chapter 5, we beamform the row data utilizing VSSA. Despite the capability of proposed USE methods in estimating both axial and lateral displacements, the latter is of lower quality compared to the former for three main reasons: low sampling rate, lack of carrier signal and low resolution in the lateral direction. In this chapter, we propose to use VSSA imaging that implements Synthetic Aperture (SA)-based beamforming on focused transmitted signals. On the one hand, this enables us to benefit from advantages of SA such as high resolution and the capability to increase the sampling frequency to increase the resolution and number of A-lines. On the other hand, we can take advantageous of line-by-line imaging in high penetration depth.

In Chapter 6, we propose a novel method for 2D displacement estimation method for more precise and accurate lateral displacement estimation called MUSCULAR. In MUSCULAR, we add physics-based constraints as a regularization part to the cost function, as well as absolute intensity differences and displacement continuity of neighboring samples. We show that the additional physics-based constraints substantially improve the accuracy of the 2D displacement estimation, and outline a computationally efficient way to exploit physics-based constraints.

The last chapter concludes the thesis and proposes some ideas for future work. Despite the proposed USE methods to increase accuracy of tracking tissue motion, still the estimation is lateral direction is not as good as the axial one. Low resolution and lack of carrier signal in lateral direction is two of the important factors. However, increasing resolution in lateral direction does not necessarily increase the estimation accuracy. We outline avenues for future work to address these issues.

### 1.2.6 List of Publications

- **Journal Papers**

  1. M. Mirzaei, A. Asif, and H. Rivaz, "Virtual source synthetic aperture for accurate lateral displacement estimation in ultrasound elastography," IEEE Transactions on Ultrasonics, Ferroelectrics, and Frequency Control, 2020. (Chapter 5 of the thesis.)

  2. M. Mirzaei, A. Asif, and H. Rivaz, "Accurate and precise time-delay estimation for ultrasound elastography with pre-beamformed channel data," IEEE Transactions on Ultrasonics, Ferroelectrics, and Frequency Control, 2020. (Chapter 4 of the thesis.)

  3. M. Mirzaei, A. Asif, and H. Rivaz, "Combining total variation regularization with window-based time delay estimation in ultrasound elastography," IEEE transactions on medical imaging, vol. 38, no. 12, pp. 2744-2754, 2019. (Chapter 3 of the thesis.)

  4. M. Mirzaei, A. Asif, M. Fortin, and H. Rivaz, "3d normalized cross-correlation for estimation of the displacement field in ultrasound elastography," Ultrasonics, vol. 102, p. 106053, 2020. (Chapter 2 of the thesis.)

  5. M. Mirzaei, A. Asif and H. Rivaz, "2D Displacement Estimation for Qausi-Static Ultrasound Elastography," submitted to IEEE transactions on medical imaging. (Chapter 6 of the thesis.)

- **Conference Papers**

  1. M. Mirzaei, A. Asif, and H. Rivaz, "Ultrasound elastography utilizing pre-beamformed data," in 2019 IEEE 16th International Symposium on Biomedical Imaging (ISBI 2019), pp. 1725-1728, IEEE, 2019.

  2. M. Mirzaei, A. Asif, and H. Rivaz, "Synthetic aperture with high lateral sampling frequency for ultrasound elastography," in 2020 IEEE 42nd Annual International Conference of the IEEE Engineering in Medicine & Biology Society (EMBC 2020), pp. 2071-2074, IEEE, 20202.

# Chapter 2

# Window-based Elastography

**This chapter is based on our published paper [57].**

---

Estimation of tissue displacement is often referred to as Time Delay Estimation (TDE), which usually relies on raw RF data. Since one sample of RF data does not provide enough information to calculate displacement, most methods are based on dividing the RF data into several overlapping windows and calculating the displacement of each window [58]. The underlying assumption here is that displacement of all samples within the window is the same, and therefore, additional information from the neighboring samples is exploited to calculate the displacement of the sample at the center of the window. This additional information helps reduce the estimation variance.

Maximization of the NCC of windows was one of the first approaches used for TDE, which is still a very popular approach because it is easy-to-implement and is computationally efficient [59–61]. Phase correlation wherein zero crossing of phase determines displacement [62, 63] and sum of absolute difference of windows [64] are other major window-based techniques for USE.

Window-based techniques are easy to implement, but one of the most important disadvantages of these algorithms is false peaks. False peaks occur when a secondary NCC peak or zero crossing of phase or sum of absolute difference, exceeds true ones. False peaks are a common error in window-based USE methods since all windows of post-compressed image should be searched to find the best match. To overcome false peaks, time-domain cross correlation with prior estimates (TDPE) is introduced in [60]. In TPDE, only a small part of post-compressed image should be searched for correlated window and the searching area is limited to a neighborhood around the previous time-delay estimate. By utilizing TDPE, the problem of false peaks can be addressed, but still window-based algorithms are sensitive to signal de-correlation which can be caused by the out of plane or lateral displacement which are common problems especially in free-hand palpation. Another major source for signal de-correlation is blood flow and other biological motions that are common in *in-vivo* data.

In all of the aforementioned studies, the RF lines of just two images are compared

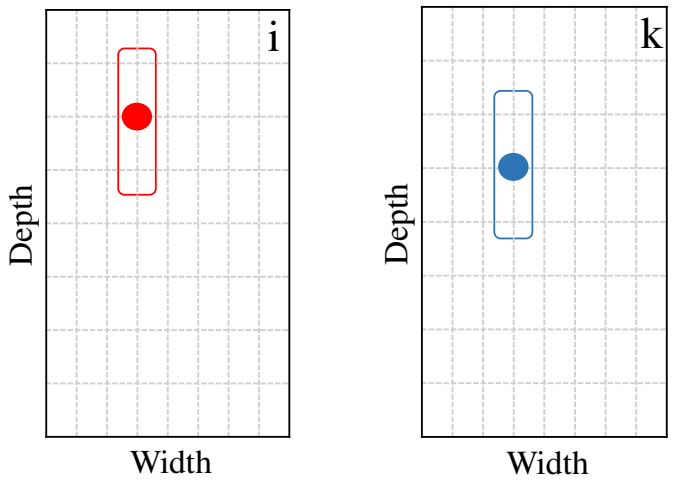


(a) (b)

Figure 2.1: Two frames of ultrasound RF data corresponding to (a) pre- and (b) post-compression. The images are severely down-sampled for visual illustration.

with each other and the displacement fields across small spatial windows are assumed to be constant as it is shown in Fig. 2.1.

In [57] we propose to utilize 3D information instead of 2D data and for the third dimension we have two options. In the first method, inspired by [65], we extend 2D spatial information to the temporal domain. We consider the cine ultrasound RF data as 3D, where the third dimension is the time domain. In other words, based on high frame rate of ultrasound machine, we consider a set of temporally neighboring frames as pre-compressed data and a set of temporally neighboring frames as post-compressed data as shown in Fig. 2.2.

In the second approach, we consider time-delayed pre-beamformed data (channel data) for USE. In ultrasound imaging, for generating an RF line several crystals record reflected waves. Time gain and also time delay due to transmission will be compensated and all data will be summed up to make one RF line. In this work we propose to use time gain and also time delay compensated channel data instead of RF data for USE, where in for each RF line its corresponding channels will be considered as third dimension as it is shown in Fig.2.3.

We maximize NCC in between 3D windows, and therefore, we name our first proposed algorithms as STNCC and the second one as CNCC. These simple and intuitive ideas substantially improves results of TDE. It is important to note that although the windows that we utilize to calculate NCC are 3D, the estimated displacement field is 2D.

STNCC and CNCC are more robust to signal de-correlation compared to NCC as shown in the simulation experiments. We also show that as the amplitude of noise increases, STNCC exhibits much less susceptibility as compared to NCC. In addition, STNCC and CNCC are less sensitive to the window size in comparison to NCC.

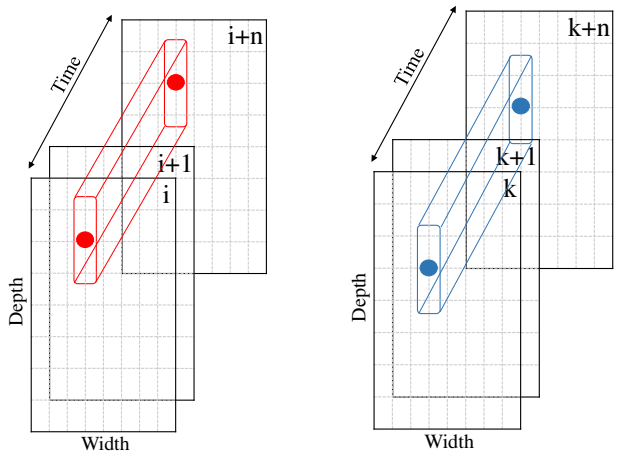


Figure 2.2: Two sequence of data used for spatial and temporal estimation of normalized correlation.

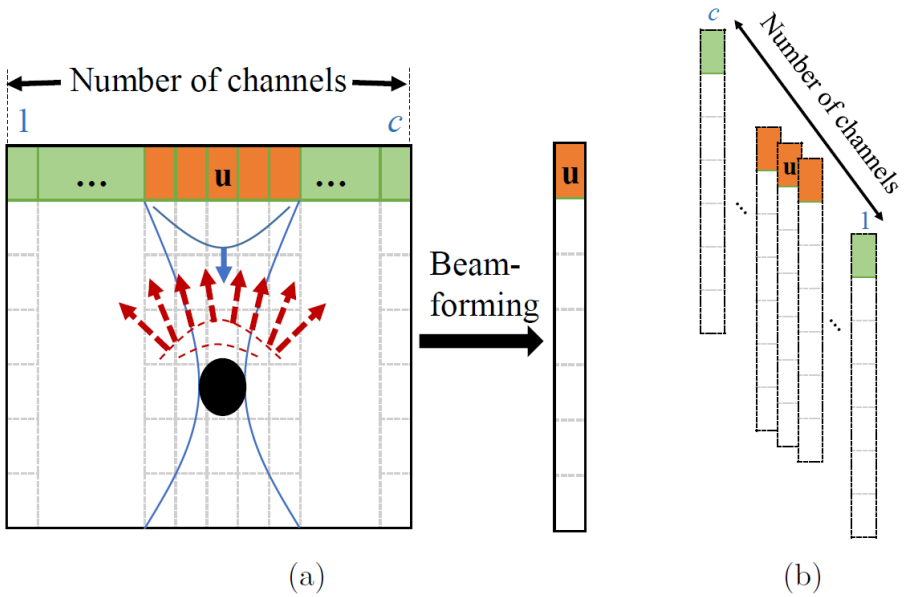


Figure 2.3: All of received data (shown in red dashed-arrows) will be beamformed to generate one line corresponding to 'u'(a). We rearrange time-delayed information of neighboring elements as shown in (b) to utilize them for CNCC.

## 2.1 Methods

Most USE methods consider two images $I_1$ and $I_2$ as pre- and post-compressed images and calculate displacement of tissue using RF data of these images. The pre-compressed RF data set is divided into several windows and for each window one should look for a window in the post-compressed RF data set that maximizes NCC as shown in Fig. 2.1.

NCC for two windows $A$ and $B$ is calculated as

$$NCC(A,B) = \frac{\Sigma_{j=1}^{j=W} A(j)B(j)}{\sqrt{\Sigma_{j=1}^{j=W} A(j)^2 \Sigma_{j=1}^{j=W} B(j)^2}}, \tag{2.1}$$

where $W$ is the number of samples in the windows and $j$ represents samples of windows. The peak of NCC corresponds to the displacement of windows in the pre-compressed image. Maximization of NCC only provides an integer displacement estimate, and interpolation should be performed to find a more accurate sub-pixel displacement estimate [66–68].

In [57] we introduced two novel techniques to use temporal or channels information. Hence instead of two 2D windows, two 3D boxes should be considered as shown in Figs. 2.2 and 2.3. In these techniques, one should look for a box in the second sequence that has the maximum NCC with the box of first sequence and peak of NCC represents displacement of the center of first box. The only assumption of these algorithms is that all samples within the box have equal displacements. This is a good assumption for STNCC since the frame rate of ultrasound machines are more than 30 fps (more than 500 fps if plane-wave imaging is used) and consecutive frames (the third dimension of data for STNCC) and their displacement will be very close to each other. It is also worthwhile to mention that by considering temporal neighbors for STNCC, temporal behavior of the estimated strains improves significantly. Temporal accuracy plays an important role in poroelastic USE [69], viscoelasticity measurement of the tissue [70], dynamic USE methods such as shear-wave USE [39, 71] and vibro-USE [72]. The results of temporal behavior of the estimated strains by STNCC are reported in the supplementary material. For CNCC the assumption of same displacement for all samples of a box is exactly the same assumption that was made for 2D Rf data.

By considering the third dimension of size $n$ for each box, the NCC of the two boxes is defined as

$$NCC(A,B) = \frac{\Sigma_{l=1}^{l=n} \Sigma_{j=1}^{j=W} A_l(j)B_l(j)}{\sqrt{\Sigma_{l=1}^{l=n} \Sigma_{j=1}^{j=W} A_l(j)^2 \Sigma_{l=1}^{l=n} \Sigma_{j=1}^{j=W} B_l(j)^2}} \tag{2.2}$$

where $A_l$ and $B_l$ are windows in the $l^{th}$ layer of the third dimension for the first and second boxes. $W$ is the number of samples in a 2D window and $j$ shows samples of 2D windows. The peak of STNCC or CNCC provides an integer displacement estimate and has to be interpolated to generate a subpixel displacement estimation. To

avoid false peaks and to reduce the computational complexity of the algorithm, the search area is determined based on the displacement of the neighboring boxes. By calculating the displacement field, strain of the tissue can be determined by differentiating displacement field in the axial direction. Differentiating amplifies the noise, and therefore, least square techniques are common method to obtain the strain field.

### 2.1.1 Data Acquisition

In this Section we describe the data that is utilized in different experiments of this chapter and then results of STNCC and CNCC are provided in the Results Section and compared with NCC in two separate subsections. For sake of comparison, contrast to noise ratio (CNR) is used to provide quantitative means for assessing the proposed method according to

$$\mathrm{CNR} = 20\log_{10}\Big(\frac{2(\bar{s}_b - \bar{s}_t)^2}{\sigma_b^2 + \sigma_t^2}\Big), \tag{2.3}$$

where $\bar{s}_t$ and $\bar{s}_b$ are the spatial strain average of the target and background, and $\sigma_b^2$ and $\sigma_t^2$ are the spatial strain variance of the target and background windows in the strain image, respectively.

In all simulations and experiments, 7 frames are considered for STNCC and outputs of STNCC are compared with strains of middle frames that are estimated by NCC.

In all experiments (except the back muscle experiment) windows of size $10\lambda$ where $\lambda$ is wavelength with 86% overlap of windows are considered and 3-point parabolic interpolation is utilized to find the 2D sub-sample location of the correlation peak. For the back muscle experiment, overlap of windows is reduced to 70% and 30% to show its effect on STNCC and NCC.

#### Simulation Data

A simulated phantom is generated by utilizing the Field II ultrasound simulation software [73]. FEM-based deformations are computed using the ABAQUS software package (Johnston, RI, USA). The simulated phantom is homogeneous except for a cylindrical inclusion with zero stiffness which is placed in the middle of the phantom as an inclusion. The ground truth strain is shown in Fig. 2.4 where the white part represents the inclusion. The inclusion simulates a blood vein that easily compresses under force. Zero stiffness can be obtained by considering a hole inside the phantom. It will not lead to infinite strain because the surrounding medium supports the hole from collapsing. The Young module of background is equal to $4kPa$ in our simulation.

To make the simulation experiment more realistic, images are normalized and uniform noises are added to images as

$$I_{ij} = \frac{I_{ij}}{\max_{i,j}(I_{ij})} + \text{noise}. \tag{2.4}$$

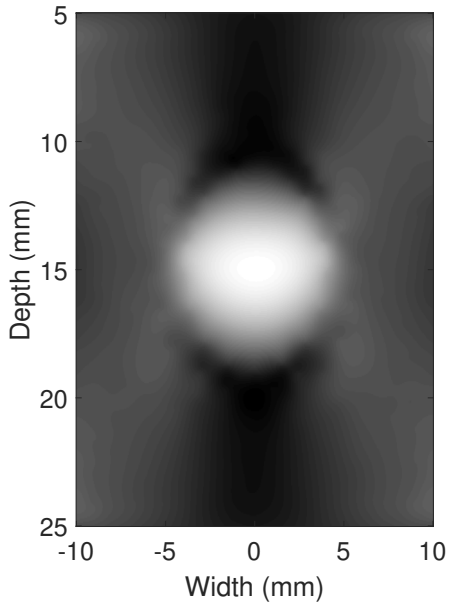


Figure 2.4: Ground truth strain in the simulation phantom. The displacement is estimated using the ABAQUS FEM software.

For calculating contrast to noise ratio, for each level of noise we ran a Monte Carlo simulation by estimating strain 100 times with different random noise. The SNR of the noisy data is calculated as

$$\mathrm{SNR} = 10\log_{10}\left(\frac{\mathrm{mean}\left(I_{ij}^2\right)}{\mathrm{mean}\left(\mathrm{noise}^2\right)}\right). \tag{2.5}$$

### Phantom Data

We use conventional beamformed RF data and time-delayed channel data for comparison of STNCC and CNCC with NCC. Conventional beamformed RF data is acquired from a tissue mimicking breast phantom (CIRS, Norfolk, VA, USA) with an Antares Siemens ultrasound machine (Siemens, Issaquah, WA, USA) and VF 13-5 probe at the center frequency of 7.27 MHz, sampling frequency of 40 MHz and frame rate of 37 fps.
Channel data is acquired from a tissue mimicking phantom (059 tissue mimicking breast phantom, CIRS tissue simulation & phantom technology, Norfolk, VA, USA) using an E-Cube R12 ultrasound machine (Alpinion, Bothell, WA, USA) with a L3-12H probe at the center frequency of 11.5 MHz, sampling frequency of 40 MHz.

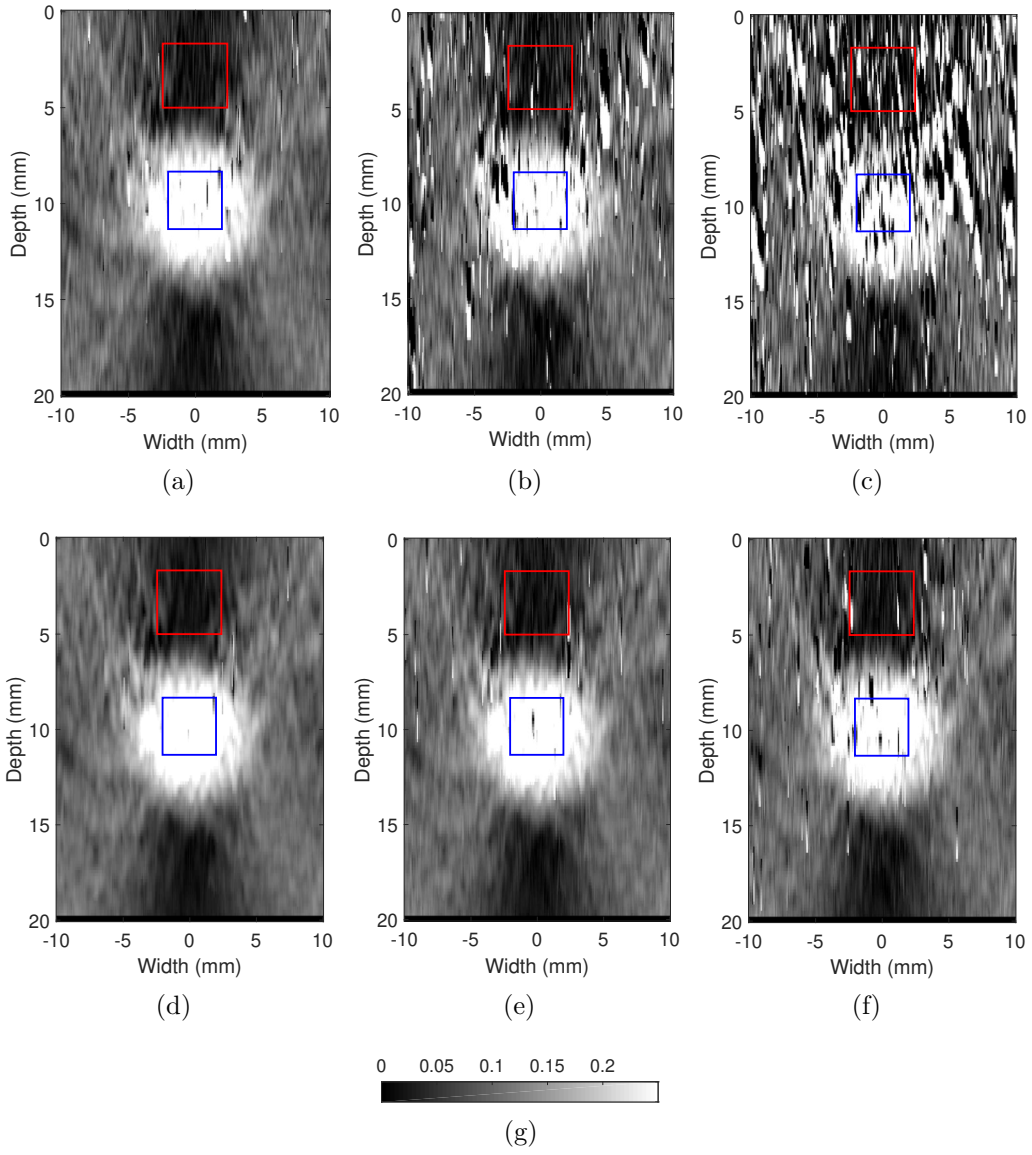


Figure 2.5: Strain images of the simulation phantom calculated using NCC and STNCC. The first row shows strain images that are calculated using NCC, and the second row depicts strain images computed using STNCC. In the first, second and third columns, the SNR values of data are 6.55 dB, 3.56 dB and 2.17 dB, respectively.

#### *In-vivo* Data

The liver data is acquired from a patient undergoing open surgical radio frequency thermal ablation for liver cancer before ablation. This data was collected at the Johns Hopkins hospital with an Antares ultrasound machine (Siemens, Issaquah, WA, USA) with a VF10-5 linear probe with a center frequency of 6.6 MHz, sampling frequency of 40 MHz and frame rate of 30 fps. The study was approved by the ethics institutional review board at Johns Hopkins. Fig. 2.9 (a) shows the B-Mode image, where the tumor is marked with red arrows.

## 2.2 Results

### 2.2.1 STNCC

In this part, results of the proposed STNCC method are presented and compared against NCC for simulated phantom and experimental data in separate subsections.

#### Simulation Results

The phantom is compressed by 0.5% and the compression rate between two consecutive frames is 0.02%. To make simulation experiment more realistic, noise is added to the images in three steps with zero mean and standard deviation of 0.086, 0.144 and 0.202. Fig. 2.5 shows outputs of STNCC and NCC for different levels of noise.

It is clear that results of STNCC are closer to ground truth and outperform results of NCC. Higher signal to noise ratio and contrast to noise ratio of STNCC that are represented in Table 2.1 also validate better performance of STNCC. For each level of noise we ran a Monte Carlo simulation by estimating strain 100 times with different random noise. The mean and variance of CNR for these 100 experiments are reported at Table 2.1.

Table 2.1: The mean and variance of CNR for 100 strain images of the simulated phantom for different methods and noise levels. Windows that are considered for calculating CNR are shown in blue and red lines in Figure 2.5.

| SNR of noisy data mean (var.) | | CNR mean (var.) |
|---|---|---|
| 6.55 ($6.91\times10^{-5}$) | STNCC | 28.28 (6.4) |
| | NCC | 21.96 (13.12) |
| 3.56 ($8.14\times10^{-5}$) | STNCC | 24.88 (8.96) |
| | NCC | 9.84 (23.20) |
| 2.17($7.53\times10^{-5}$) | STNCC | 18.56 ( 17.92) |
| | NCC | -4.12 (67.84) |

As one can see in Fig. 2.5 and Table 2.2, not only does STNCC outperform NCC for each range of noise, but it also has more robust performance against increasing amplitude of noise.

Table 2.2: Effect of increasing noise on CNR values.

| SNR of noisy data | Method | CNR% |
|---|---|---|
| From 6.55 to 3.56 | STNCC | -12.02 |
| | NCC | -55.19 |
| From 3.56 to 2.17 | STNCC | -25.40 |
| | NCC | -141.86 |

In the next experiment, we compressed the simulated phantom by 1%, 1.5% and 2% and repeated the experiment for these amounts of compression. For representing CNR, simulation is run 100 times for each case and it is shown in Fig. 2.6 that for all three compression rate and for all three different noise levels, STNCC has better performance than NCC.

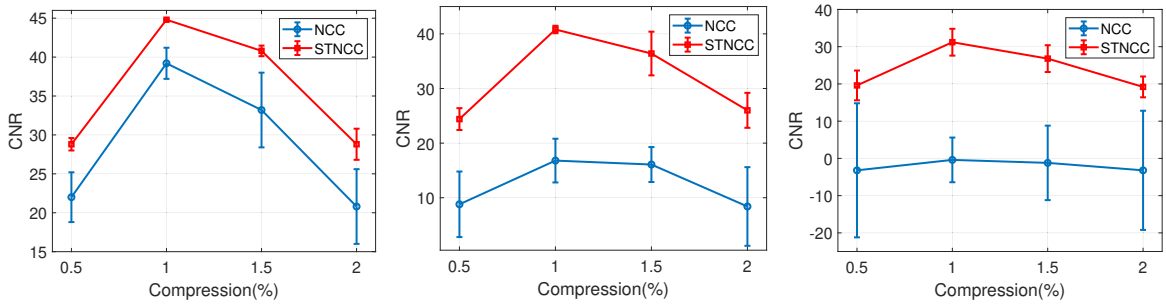


Figure 2.6: CNR values for different levels of compression and noise. The SNR of data in (a), (b) and (c) are respectively 6.55 dB, 3.56 dB and 2.17 dB.

### Phantom Results

Similar to the previous section, the images are normalized and uniform noise is added to images in three steps with zero mean and standard deviation of 0.028, 0.144 and 0.202. The estimated strains obtained from STNCC and NCC are shown in Fig. 2.7.

As one can see, results of STNCC outperform NCC. Also, STNCC is more robust to increasing magnitude of noise. For computing CNR for each level of noise, experiments are repeated for 100 times and mean and variance of CNR is presented in Table 2.3.

Edge spread functions of strains obtained by NCC and STNCC are shown in Fig. 2.8. For calculating edge spread function, two rectangular with length of 60 and width

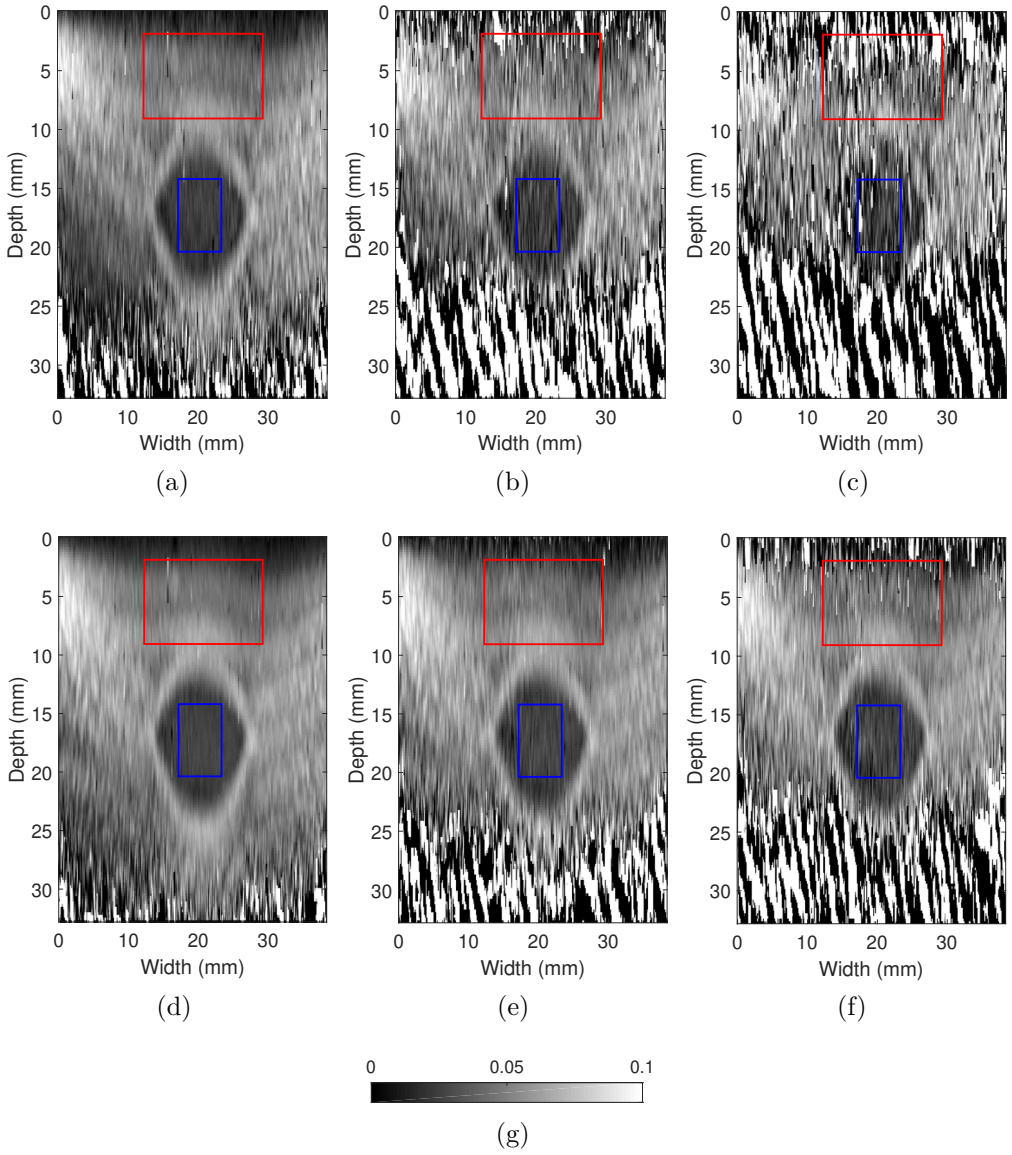


Figure 2.7: Comparison of strains that are calculated using NCC and STNCC for phantom data. The first and second rows show strain images calculated using NCC and STNCC, respectively. In the first, second and third columns, the SNR of data are 13.95 dB, 5.62 dB and 2.91 dB, respectively.

of 10 pixels are considered in strain of NCC and STNCC as shown in Figure 2.8 (a). The edge spread function is calculated by averaging intensity of pixels across width of these rectangular and it is clear in Figure 2.8 (b) that the edge spread function of STNCC is smoother than NCC.

Table 2.3: Mean and variance of CNR in 100 strain images for the conventionally beamformed RF data of the phantom at different noise levels. Windows that are considered for calculating CNR are shown in Figure 2.7.

| SNR of noisy data mean (var.) | | CNR mean (var.) |
|---|---|---|
| 13.95($4.04\times10^{-5}$) | STNCC | 24.64 ( 1.12) |
| | NCC | 21.48 (1.92) |
| 5.62($3.81\times10^{-5}$) | STNCC | 19.44 (6.56) |
| | NCC | -13.08 ( 8.32) |
| 2.91($4.17\times10^{-5}$) | STNCC | -8.48 (8) |
| | NCC | -24.80 (8.48) |

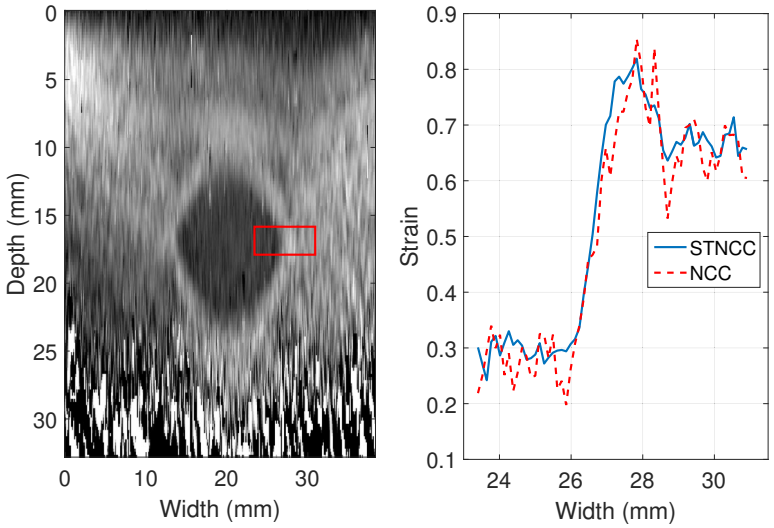


(a) (b)

Figure 2.8: Edge spread function for strain images that are calculated using NCC and STNCC. The red box in (a) shows the region of strain image where edge profiles are plotted. (b) shows the edge profiles.

### *In-vivo* Results

The estimated strains are presented in Figure 2.9 (b)-(c). Visual comparison of the strain images shows that STNCC generates a strain image with less noise. This is corroborated with quantitative results of Table 2.4, which shows CNR. Compared to NCC, STNCSS improves CNR by 71.11%.

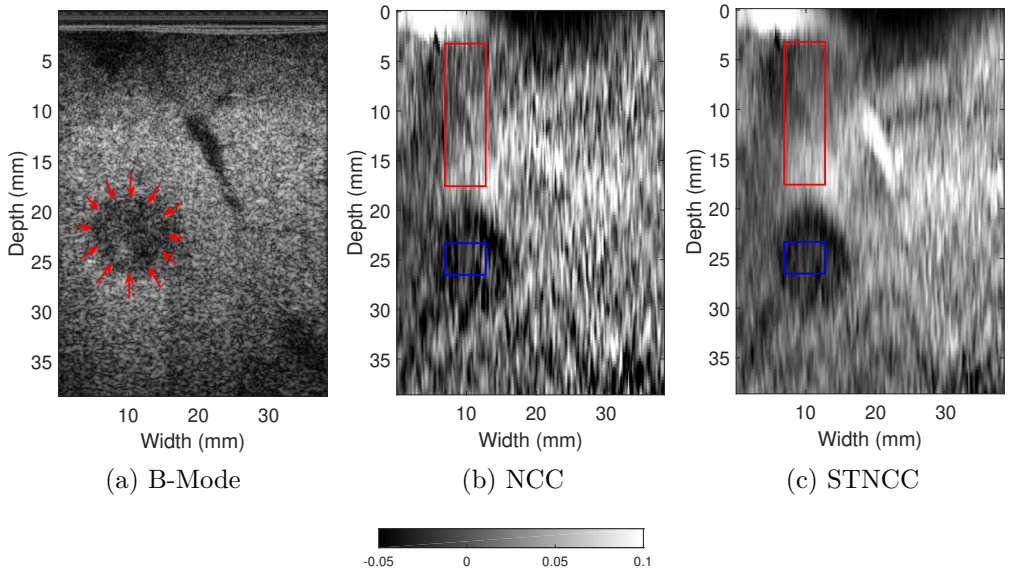


(a) B-Mode (b) NCC (c) STNCC

Figure 2.9: B-mode image of the liver with a tumor (marked with red arrows). Strain images calculated using NCC and STNCC are shown in (b) and (c) respectively.

Table 2.4: CNR values in strain images of Figure 2.9. Windows that are considered for calculating CNR are shown in Figure 2.9.

| | CNR |
|---|---|
| STNCC | 21.56 |
| NCC | 12.60 |

### 2.2.2 CNCC

#### Simulation Results

The phantom is compressed by 1% and time-delayed channel data is acquired from Filed II software for CNCC experiment. Same channel data are summed-up to generate corresponding RF data. Strain fields estimated by NCC and CNCC are illustrated in Fig. 2.10.

To further clarify better performance of CNCC, a histogram analysis is done for CNR comparison in Fig. 2.11. We have moved the small blue colored window within the big blue window to take 12 target windows. At the same time, the small red colored window is swiped within the large red window to consider 32 background windows. CNR is calculated for every combination of target and background windows. It is clear that for small values, NCC has higher frequencies than CNCC but for higher values of CNR, CNCC has higher frequency.

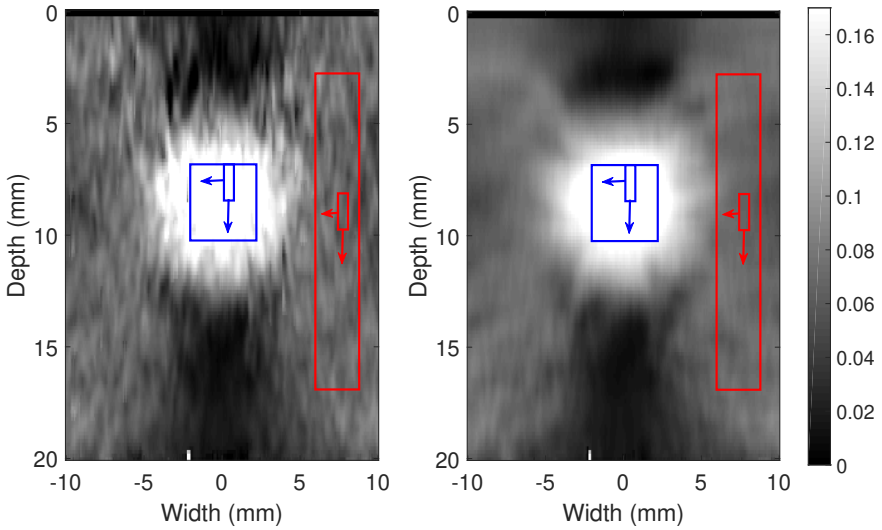


(a) (b)

Figure 2.10: Strain images of simulated phantom calculated using NCC and CNCC are shown in (a) and (b) respectively.

### Phantom Results

For fair comparison of CNCC and NCC, channel data that are utilized for providing results of CNCC are beamformed with the same ultrasound machine and then fed to NCC. Estimated strains of CNCC and normal NCC are shown in Fig. 2.12. For comprehensive CNR comparison, histogram analysis is done which is shown in Fig. 2.13. We have moved the small red colored window within the big red window to take 12 target windows. At the same time, the small blue colored window is swiped within the large blue window to consider 24 background windows. CNR is calculated for every combination of target and background windows. Fig. 2.13 shows distribution

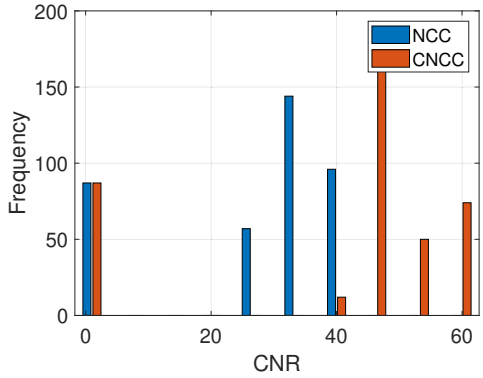


Figure 2.11: Histogram distribution of CNR for estimated strain of simulated phantom by NCC and CNCC.

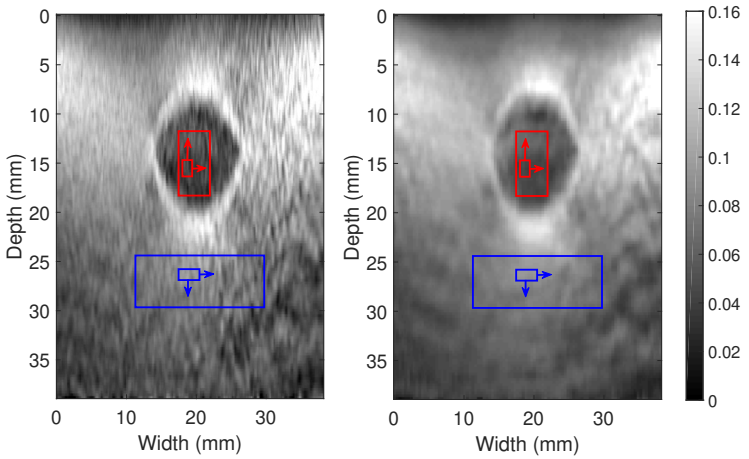


(a) (b)

Figure 2.12: Strain images of experimental phantom calculated using NCC and CNCC are shown in (a) and (b) respectively.

of the aforementioned 288 CNR values. It is clear that for small CNR values, NCC has higher frequencies than CNCC but for higher values of CNR, CNCC has higher frequency.

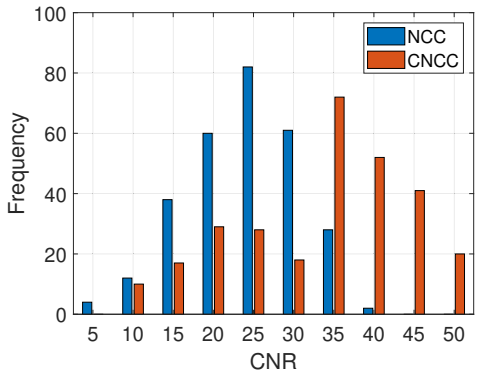


Figure 2.13: Histogram distribution of CNR for estimated strain of experimental phantom by NCC and CNCC.

## 2.3 Conclusions

Ultrasound systems are capable of acquiring images at a very high frame rate. This capability is not exploited in previous window-based USE algorithms where the windows were only in the spatial domain. As well as a high frame rate, we know that for generating one RF line multiple channels are employed to record data. In this chapter, a novel idea was proposed to consider third dimension information which

can be two sequence of images instead of just two images or considering all channels that play role in producing one RF line. In these methods, 3D boxes in the first series are matched to those of the second series. It was shown using simulation, phantom and *in-vivo* experiments that extension of information to third direction substantially improves the quality of displacement estimation.

# Chapter 3

# Combining total variation regularization with window-based time delay estimation in ultrasound elastography

**This chapter is based on our published paper [74].**

---

Optimizing a regularized cost function is another approach for USE to impose smoothness regularization to make the problem well-posed [75–81]. These methods were computationally complex, but real-time USE based on regularized cost functions have recently been developed by exploiting Dynamic Programming and Analytic Minimization (DPAM) [2,46] and GLUE [33]. These methods result in dense displacement and strain fields with the same size as the RF data. The main disadvantage of these methods is that utilizing quadratic regularization term leads to over-smoothed displacement fields. In recent research, temporal information is also considered in the optimization [82].

Inspired by [29] in utilizing both window based and regularized optimization based techniques for optical flow research field, we combine window-based and regularized optimization-based methods to increase robustness of the algorithm against noise which is abundant in free-hand USE due to out-of-plane movement, blood flow and other biological motions common in *in-vivo* data. The second major novelty of this paper is that we use total variation regularization (also known as the L1 norm regularization), which results in substantially sharper displacement maps. An iterative method is utilized for estimating the displacement, which further increases accuracy and robustness of the estimation against noise. We call our method OVERWIND and show that it outperforms both window-based and standard regularization-based approaches.

## 3.1 Methods

Let $I_1$ and $I_2$ be the two frames of RF data collected as the tissue is undergoing some deformation. TDE entails estimating the displacement field between these two images. In this section, we first briefly describe the closely related previous work (GLUE) [33] and then present OVERWIND and derive equations to calculate TDE using this method.

### 3.1.1 GLUE: GLobal Ultrasound Elastography

In GLUE, the displacements are divided into integer and subsample displacement estimates. The initial integer displacement estimates come form Dynamic Programming (DP) [78]. The goal of GLUE is to calculate the subsample displacement component by minimizing the following cost function:

$$\begin{aligned} C(\Delta a_{1,1}, \Delta l_{1,1}, , \ldots, \Delta a_{m,n}, \Delta l_{m,n}) = \quad & \Sigma_{j=1}^{n} \Sigma_{i=1}^{m} \{ D(i, a_{i,j}, \Delta a_{i,j}, j, l_{i,j}, \Delta l_{i,j}) \\ & + R(i, a_{i,j}, \Delta a_{i,j}, j, l_{i,j}, \Delta l_{i,j}) \} \end{aligned} \tag{3.1}$$

where the data term $D$ is:

$$D(i, a_{i,j}, \Delta a_{i,j}, j, l_{i,j}, \Delta l_{i,j}) = [I_1(i,j) - I_2(i + a_{i,j} + \Delta a_{i,j}, j + l_{i,j} + \Delta l_{i,j})]^2$$

and the regularization term $R$ is:

$$\begin{aligned} R(i, a_{i,j}, \Delta a_{i,j}, j, l_{i,j}, \Delta l_{i,j}) \quad & = \alpha_1 (a_{i,j} + \Delta a_{i,j} - a_{i-1,j} - \Delta a_{i-1,j})^2 \\ & + \alpha_2 (a_{i,j} + \Delta a_{i,j} - a_{i,j-1} - \Delta a_{i,j-1})^2 \\ & + \beta_1 (l_{i,j} + \Delta l_{i,j} - l_{i-1,j} - \Delta l_{i-1,j})^2 \\ & + \beta_2 (l_{i,j} + \Delta l_{i,j} - l_{i,j-1} - \Delta l_{i,j-1})^2. \end{aligned}$$

In these equations, $I_1$ and $I_2$ are pre- and post-compressed RF data of size $m \times n$. Notation $a_{i,j}$ and $l_{ij}$ are axial and lateral integer displacements that are estimated using DP and $\Delta a_{i,j}$ and $\Delta l_{i,j}$ are axial and lateral subsample displacements that should be calculated. Finally, $\alpha_1$, $\alpha_2$, $\beta_1$ and $\beta_2$ are regularization parameters.

GLUE calculates the displacement estimates of all samples of the RF data simultaneously. As such, GLUE is relatively robust to local signal decorrelations since correlated areas guide the decorrelated regions. However, its displacement maps are very smooth, which leads to blurry strain images. In the next subsection, we increase robustness and also tackle the problem of blurriness by introducing OVERWIND, which replaces the data term with a window-based term, and substitutes the regularization term with total variation regularization.

### 3.1.2 Utilizing Window-Based Data Terms

Inspired by [29], we combine window- and optimization-based methods to increase robustness of elastogram against noise by utilizing information available in the neighborhood of the reference sample. Therefore, for pixel $(i, j)$, we consider a window of size $(2w_a + 1) \times (2w_l + 1)$ around sample $(i, j)$ and assume that all samples in this neighborhood have the same displacement as sample $(i, j)$, an assumption that is similar to the one used in the window-based methods. Therefore, the data term in Eq. (3.1) is replaced by

$$D(i, a_{i,j}, \Delta a_{i,j}, j, l_{i,j}, \Delta l_{i,j}) = \begin{array}{l} \frac{1}{(2w_a+1)(2w_l+1)} \Sigma_{k=-w_a}^{w_a} \Sigma_{r=-w_l}^{w_l} (I_1(i+k, j+r) \\ -I_2(i+k+a_{i,j}+\Delta a_{i,j}, j+r+l_{i,j}+\Delta l_{i,j}))^2 \end{array}$$

The unknown variables $\Delta a$ and $\Delta l$ are now inside the "nonlinear function"$I_2$, which means that the cost function cannot be optimized efficiently. To make the data term quadratic, we replace $I_2(i+k+a_{i,j}+\Delta a_{i,j}, j+r+l_{i,j}+\Delta l_{i,j})$ with its first order Taylor series expansion around $(i+k+a_{i,j}, j+r+l_{i,j})$. Furthermore, to simplify the notation, we denote $\frac{1}{(2w_a+1)(2w_l+1)} \Sigma_{k=-w_a}^{w_a} \Sigma_{r=-w_l}^{w_l}(.)$ as $\frac{1}{L}\Sigma_{k,r}(.)$ and $I_2(i+k+a_{i,j}, j+r+l_{i,j})$ as $I_2(.)$, so the data term can be rewritten as

$$D(i, a_{i,j}, \Delta a_{i,j}, j, l_{i,j}, \Delta l_{i,j}) = \frac{1}{L}\Sigma_{k,r}\Big(I_1(i+k, j+r) - I_2(.) - \Delta a_{i,j} I'_{2a}(.) - \Delta l_{i,j} I'_{2l}(.)\Big)^2 \tag{3.2}$$

where $I'_{2a}(.)$ and $I'_{2l}(.)$ are derivatives of $I_2$ in axial and lateral directions, respectively.

### 3.1.3 Using L1 Norm Regularization

The second issue of GLUE arises from the L2 norm regularization, which penalizes high gradients of displacement, and as such, prevents discontinuities in the displacement field. To cope with this problem, a non-quadratic regularization term should be utilized. The L1 norm regularization, which has a form of $\delta(s) = |s| = \sqrt{s^2}$ has optimal characteristic in terms of allowing sharp transitions. Although this regularization is convex, it is not differentiable at $s = 0$, which means that it cannot be efficiently optimized. A commonly used technique to address this problem is to slightly perturb the regularization term around $s = 0$ [83]. In this paper, we use $\delta_x(s) = 2\lambda_x\sqrt{\lambda_x^2 + s^2}$ for regularization, where $\lambda_x$ is a scaling parameter.

An inherent feature of regularization is that it reduces estimation variance at the cost of increased bias. In other words, we penalize the difference between $a_{i,j} + \Delta a_{i,j}$ and $a_{i-1,j} - \Delta a_{i-1,j}$, which leads to an underestimated displacement estimation. To prevent this kind of underestimation bias, $\varepsilon_a$ and $\varepsilon_l$ can be considered in the regularization term, where $\varepsilon_a$ is the average of integer axial displacement difference between subsequent samples $i$ and $i-1$ and $\varepsilon_l$ is the average of integer lateral displacement difference between samples $j$ and $j-1$ which are available from DP.

Inserting the proposed non-quadratic and unbiased regularization term, we have:

$$\begin{aligned} R(i,a_{i,j},\Delta a_{i,j},j,l_{i,j},\Delta l_{i,j}) &= \alpha_1\delta_1(a_{i,j}+\Delta a_{i,j}-a_{i-1,j}-\Delta a_{i-1,j}-\varepsilon_a) \\ &+\alpha_2\delta_2(a_{i,j}+\Delta a_{i,j}-a_{i,j-1}-\Delta a_{i,j-1}) \\ &+\beta_1\delta_3(l_{i,j}+\Delta l_{i,j}-l_{i-1,j}-\Delta l_{i-1,j}) \\ &+\beta_2\delta_4(l_{i,j}+\Delta l_{i,j}-l_{i,j-1}-\Delta l_{i,j-1}-\varepsilon_l). \end{aligned} \tag{3.3}$$

Considering Eqs. (3.2) and (3.3), the final cost function can be presented as

$$\begin{aligned} &C(\Delta a_{1,1},\ldots,\Delta a_{m,n}) = \Sigma_{j=1}^{n}\Sigma_{i=1}^{m}\Big[\tfrac{1}{L}\Sigma_{k,r}\Big(I_1(i+k,j+r) \\ &-I_2(.)-\Delta a_{i,j}I'_{2a}(.)-\Delta l_{i,j}I'_{2l}(.)\Big)^2 \\ &+\alpha_1\delta_1(a_{i,j}+\Delta a_{i,j}-a_{i-1,j}-\Delta a_{i-1,j}-\varepsilon_a) \\ &+\alpha_2\delta_2(a_{i,j}+\Delta a_{i,j}-a_{i,j-1}-\Delta a_{i,j-1}) \\ &+\beta_1\delta_3(l_{i,j}+\Delta l_{i,j}-l_{i-1,j}-\Delta l_{i-1,j}) \\ &+\beta_2\delta_4(l_{i,j}+\Delta l_{i,j}-l_{i,j-1}-\Delta l_{i,j-1}-\varepsilon_l)\Big]. \end{aligned}$$

To find the optimal $\Delta a_{i,j}$ and $\Delta l_{i,j}$ values, one needs to differentiate $C$ with respect to $\Delta a_{i,j}$ and $\Delta l_{i,j}$ and set the derivatives to zero, i.e. $\frac{\partial C}{\partial \Delta a_{i,j}} = 0$, and $\frac{\partial C}{\partial \Delta l_{i,j}} = 0$. To cope with the nonlinearity that $\delta'_x(s)$ will introduce to equations, we can use iterative methods wherein we assume $\vartheta = \dfrac{1}{\sqrt{\lambda_x^2+s^2}}$ is fixed and equations are linear in each iteration. After every iteration, $\vartheta$ will use the updated value in the previous iteration. In this case by stacking all $2mn$ unknown parameters in a vector as $\Delta d_{2m\times n} = [\Delta a_{1,1}, \Delta l_{1,1}\Delta a_{1,2}, \Delta l_{1,2}, \cdots, \Delta a_{m,n}, \Delta l_{m,n}]^T$ , the following linear equation should be solved to obtain the optimal subsample displacements

$$(H+D)\Delta d = \frac{1}{L}\Sigma_{k,r}(P\mu) - Dd - b_1\varepsilon_a - b_2\varepsilon_l \tag{3.4}$$

where

$$H = \mathrm{diag}\{h(1,1),\cdots,h(1,n),\cdots,h(m,1),\cdots,h(m,n)\}$$

and $h(i,j)$ is a $2\times 2$ matrix as

$$h(i,j) = \begin{bmatrix} \frac{1}{L}\Sigma_{k,r}(I'_{2a}(.))^2 & \frac{1}{L}\Sigma_{k,r}(I'_{2a}(.)I'_{2l}(.)) \\ \frac{1}{L}\Sigma_{k,r}(I'_{2a}(.)I'_{2l}(.)) & \frac{1}{L}\Sigma_{k,r}(I'_{2l}(.))^2 \end{bmatrix}.$$

$P$ is a diagonal matrix as

$$P = \mathrm{diag}\{e(1,1),\cdots,e(1,n),\cdots,e(m,1),\cdots,e(m,n)\}$$

where $e(i,j)$ is a $2\times 2$ matrix as

$$e(i,j)=\begin{bmatrix} I'_{2a}(.) & 0 \\ 0 & I'_{2l}(.) \end{bmatrix}.$$

$\mu$ is a vector as

$$\mu=[g_{1,1},g_{1,2},\cdots,g_{m,n}]^{\mathrm{T}}\otimes[1,1]^{\mathrm{T}}$$

where $g_{i,j}$ is subtraction of two images as

$$g_{i,j}=I_1(i+k,j+r)-I_2(.)$$

and $\otimes$ is Kronecker tensor product. The matrix $D$ can be organized as

$$D=\begin{bmatrix} Q_1 & R_1 & 0 & 0 & \dots & \dots & 0 \\ R_1 & S_1 & R_2 & 0 & 0 & \dots & 0 \\ 0 & R_2 & S_2 & R_3 & 0 & \ddots & \vdots \\ \vdots & \ddots & \ddots & \ddots & \ddots & \ddots & \vdots \\ 0 & 0 & 0 & R_{m-3} & S_{m-3} & R_{m-2} & 0 \\ 0 & 0 & 0 & \ddots & R_{m-2} & S_{m-2} & R_{m-1} \\ 0 & \dots & \dots & 0 & 0 & R_{m-1} & Q_2 \end{bmatrix}$$

where $Q_1$, $Q_2$ and $S_z,\ z\in\{1,\cdots,m-2\}$ are pentadiagonal matrices with the following structure

$$\begin{bmatrix} * & 0 & * & & & & \\ 0 & * & 0 & * & & \multicolumn{2}{c}{\multirow{2}{*}{0}} \\ * & 0 & * & 0 & * & & \\ & \ddots & \ddots & \ddots & \ddots & \ddots & \\ & & * & 0 & * & 0 & * \\ & \multicolumn{2}{c}{\multirow{2}{*}{0}} & * & 0 & * & 0 \\ & & & & * & 0 & * \end{bmatrix}$$

with the main diagonals (md) given in Eqs. (3.8) and (3.9). The first upper/lower diagonals are zero, while the second upper/lower diagonals (sd) are

$$\begin{aligned} Q_{1\mathrm{sd}} &= -\Big[\Theta_2(1,2),\Gamma_2(1,2),\cdots,\Theta_2(1,n),\Gamma_2(1,n)\Big]^T, \\ Q_{2\mathrm{sd}} &= -\Big[\Theta_2(m,2),\Gamma_2(m,2),\cdots,\Theta_2(m,n),\Gamma_2(m,n)\Big]^T, \\ S_{z\mathrm{sd}} &= -[\Theta_2(z+1,2),\Gamma_2(z+1,2),\cdots,\Theta_2(z+1,n),\Gamma_2(z+1,n)]^T \end{aligned}$$

$$
Q_{1\mathrm{md}} = \begin{bmatrix}
\Theta_1(2,1) + \Theta_2(1,2) \\
\Gamma_1(2,1) + \Gamma_2(1,2) \\
\Theta_1(2,2) + \Theta_2(1,2) + \Theta_2(1,3) \\
\Gamma_1(2,2) + \Gamma_2(1,2) + \Gamma_2(1,3) \\
\vdots \\
\Theta_1(2,n-1) + \Theta_2(1,n-1) + \Theta_2(1,n) \\
\Gamma_1(2,n-1) + \Gamma_2(1,n-1) + \Gamma_2(1,n) \\
\Theta_1(2,n) + \Theta_2(1,n) \\
\Gamma_1(2,n) + \Gamma_2(1,n)
\end{bmatrix},
$$

$$
Q_{2\mathrm{md}} = \begin{bmatrix}
\Theta_1(m,1) + \Theta_2(m,2) \\
\Gamma_1(m,1) + \Gamma_2(m,2) \\
\Theta_1(m,2) + \Theta_2(m,2) + \Theta_2(m,3) \\
\Gamma_1(m,2) + \Gamma_2(m,2) + \Gamma_2(m,3) \\
\vdots \\
\Theta_1(m,n-1) + \Theta_2(m,n-1) + \Theta_2(m,n) \\
\Gamma_1(m,n-1) + \Gamma_2(m,n-1) + \Gamma_2(m,n) \\
\Theta_1(m,n) + \Theta_2(m,n) \\
\Gamma_1(m,n) + \Gamma_2(m,n)
\end{bmatrix}, \tag{3.8}
$$

where

$$
\begin{aligned}
\Theta_1(i,j) &= \frac{\alpha_1 \lambda_1}{\sqrt{\lambda_1^2 + (a_{i,j} + \Delta a_{i,j} - a_{i-1,j} - \Delta a_{i-1,j} - \varepsilon)^2}}, \\
\Theta_2(i,j) &= \frac{\alpha_2 \lambda_2}{\sqrt{\lambda_2^2 + (a_{i,j} + \Delta a_{i,j} - a_{i,j-1} - \Delta a_{i,j-1})^2}}, \\
\Gamma_1(i,j) &= \frac{\beta_1 \lambda_3}{\sqrt{\lambda_3^2 + (l_{i,j} + \Delta l_{i,j} - l_{i-1,j} - \Delta l_{i-1,j})^2}}, \\
\Gamma_2(i,j) &= \frac{\beta_2 \lambda_4}{\sqrt{\lambda_4^2 + (l_{i,j} + \Delta l_{i,j} - l_{i,j-1} - \Delta l_{i,j-1})^2}}.
\end{aligned}
$$

$R_\kappa,\ \kappa \in \{1, \cdots, m-1\}$, are diagonal matrices with the main diagonal given by

$$
-\Big[\Theta_1(\kappa+1,1), \Gamma_1(\kappa+1,1), \cdots, \Theta_1(\kappa+1,n), \Gamma_1(\kappa+1,n)\Big]^T.
$$

Finally vectors $b_1$ and $b_2$ are defined in Eq. (3.10).

In the final step, the estimated displacement field is spatially differentiated to calculate strain. In particular, a least squares regression technique is used to limit the effect of noise on the gradient operator.

$$S_{z\mathrm{md}} = \begin{bmatrix} \Theta_1(z+1,1) + \Theta_1(z+2,1) + \Theta_2(z+1,2) \\ \Gamma_1(z+1,1) + \Gamma_1(z+2,1) + \Gamma_2(z+1,2) \\ \Theta_1(z+1,2) + \Theta_1(z+2,2) + \Theta_2(z+1,2) + \Theta_2(z+1,3) \\ \Gamma_1(z+1,2) + \Gamma_1(z+2,2) + \Gamma_2(z+1,2) + \Gamma_2(z+1,3) \\ \vdots \\ \Theta_1(z+1,n-1) + \Theta_1(z+2,n-1) + \Theta_2(z+1,n-1) + \Theta_2(z+1,n) \\ \Gamma_1(z+1,n-1) + \Gamma_1(z+2,n-1) + \Gamma_2(z+1,n-1) + \Gamma_2(z+1,n) \\ \Theta_1(z+1,n) + \Theta_1(z+2,n) + \Theta_2(z+1,n) \\ \Gamma_1(z+1,n) + \Gamma_2(z+2,n) + \Gamma_2(z+1,n) \end{bmatrix}, \tag{3.9}$$

---

$$\begin{gathered} b_1 = [\Theta_1(2,1), 0, \cdots, \Theta_1(2,n), 0, \Theta_1(3,1) - \Theta_1(2,1), 0, \cdots, \Theta_1(3,n) - \Theta_1(2,n), 0, \cdots, \\ \Theta_1(m,1) - \Theta_1(m-1,1), 0, \cdots, \Theta_1(m,n) - \Theta_1(m-1,n), 0, -\Theta_1(m,1), 0, \cdots, -\Theta_1(m,n), 0] \\ b_2 = [0, \Gamma_2(2,1), \cdots, 0, \Gamma_2(2,n), 0, \Gamma_2(3,1) - \Gamma_2(2,1), \cdots, 0, \Gamma_2(3,n) - \Gamma_2(2,n), \cdots, 0, \\ \Gamma_2(m,1) - \Gamma_2(m-1,1), \cdots, 0, \Gamma_2(m,n) - \Gamma_2(m-1,n), 0, -\Gamma_2(m,1), \cdots, 0, -\Gamma_2(m,n)] \end{gathered} \tag{3.10}$$

---

### 3.1.4 Data Acquisition and Comparison Methods

#### Simulation Data

The first simulation experiment has a sharp change in the displacement field to highlight the differences between GLUE and OVERWIND. All samples of the image have a displacement of zero, except for a rectangle in the middle which is moved by two pixels as shown in Fig. 3.2(a).

In the next step, a homogeneous phantom with a cylindrical inclusion with zero stiffness as shown in Fig. 3.1 is considered. The inclusion simulates a vein which has little resistance to compression. Ultrasound images are generated using the Field II ultrasound simulation software [73] by considering slightly more than 10 scatterers per $mm^3$ to satisfy Rayleigh scattering regime [84]. Deformations are computed using the ABAQUS FEM software package (Providence, RI, USA). For computing displacement of scatterers, the phantom is meshed and compressed using finite element simulation to get the 3D displacement of each node of the mesh. The displacement of each scatterer is then calculated by interpolating the displacement of its neighboring nodes.

#### Phantom Data

The phantom experiment was carried out at PERFORM centre, Concordia Univeristy. RF data is acquired from a model 059 tissue mimicking breast phantom (CIRS, Norfolk, VA, USA) using an E-Cube R12 ultrasound machine (Alpinion, Bothell, WA,

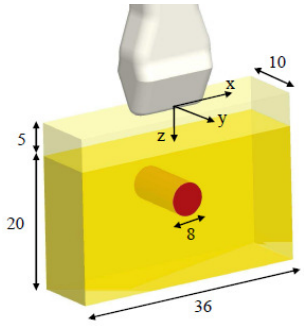


Figure 3.1: Schematic of the simulated phantom by Field II with the simulated vein in the middle with zero stiffness (from [2]).

USA) with a L3-12H probe operating at the center frequency of 7.27 MHz and sampling frequency of 40 MHz.

### *In-vivo* Data

For the clinical study, we analyze data from three patients with liver cancer. The data were collected at the Johns Hopkins hospital with an Antares ultrasound machine (Siemens, Issaquah, WA, USA) using a VF10-5 linear probe with a center frequency of 6.6 MHz and sampling frequency of 40 MHz. The study was approved by the ethics institutional review board at Johns Hopkins University.

### Comparison Methods

OVERWIND combines window-based methods with regularized optimization-based techniques. To illustrate its performance, we compare it to NCC (a pure window-based method) and GLUE (a pure regularized optimization-based method) on data collected from simulations, phantom and *in-vivo* experiments. For comparison to GLUE, the publicly available GLUE code is used. NCC is straightforward to implement, but suffers from sensitivity to signal de-correlation and false peaks which occur when a secondary NCC peak or zero crossing of phase or sum of absolute difference exceeds the true ones. To reduce the chance of false peaks, time-domain cross correlation with prior estimates (TDPE) is introduced in [60] which is also utilized in this paper to complement NCC with windows of size $(10 \times 4)$ $\lambda$ and 86% overlap of windows. In addition, 3-point parabolic interpolation is used to find the 2D sub-sample location of the correlation peak. The results of NCC with a spline-based interpolation method to find the subsample displacement estimates are shown in the Supplementary Material In TPDE, only a small part of post-compressed RF data should be searched for correlated window and the searching area is limited to a neighborhood around the previous time-delay estimate. To improve the results of NCC, we up-sample the RF data using 2D splines by a factor of 10 in both dimensions and down-sample estimated displacement from NCC using 2D splines by a factor of 1/10. This significantly

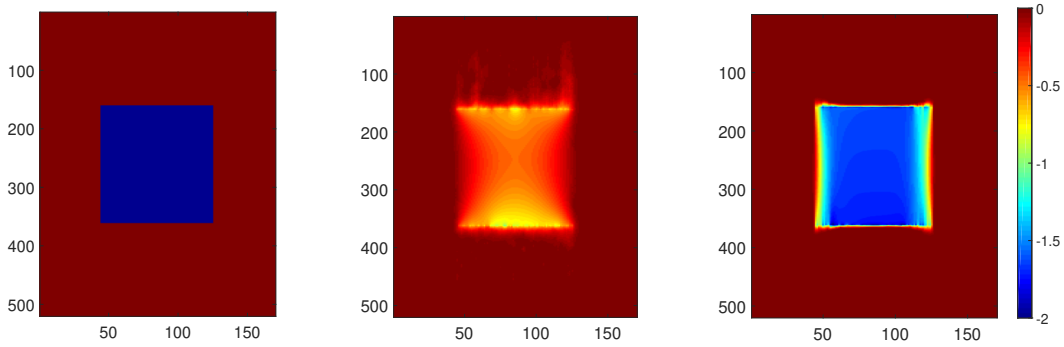


(a) Ground truth (b) GLUE (c) OVERWIND

Figure 3.2: Comparison of GLUE and OVERWIND in a simulation experiment.

improved the results at a cost of increased computational complexity by a factor of more than 100.

The Contrast to Noise Ratio (CNR) is also considered to highlight differences in the outputs of the two approaches quantitatively. The CNR is computed according to [7]:

$$\text{CNR} = 20\log_{10}\left(\frac{2(\bar{s}_b - \bar{s}_t)^2}{\sigma_b^2 + \sigma_t^2}\right), \tag{3.5}$$

where $\bar{s}_t$ and $\bar{s}_b$ are averages of strain in the target and background windows, $\sigma_b^2$ and $\sigma_t^2$ are variances of the strain in the target and background windows, and $\bar{s}$ and $\sigma$ are the average and variance of strain over small windows, respectively. It is important to note that each window should be large enough to ensure statistically meaningful values of mean and variance, and should be located in a region where the ground truth strain is uniform within the window.

## 3.2 Results

### Simulation Results

For the first simple simulation experiment, the estimated displacement fields obtained from GLUE and OVERWIND are shown in Fig. 3.2(b) and (c), respectively. This example clearly illustrates the limitation of the L2 norm in GLUE, which puts very heavy penalty in sharp changes in the displacement field because of the power 2. Whereas the L1 norm in OVERWIND tolerates sharp changes in displacement, and as such, creates a displacement field that is very sharp.

In the second simulation study, the simulated phantom is compressed by 1% and the resulting strain images estimated by NCC, GLUE and OVERWIND are shown in Fig. 3.3. The OVERWIND strain image is the closest one to the ground-truth strain, especially around the inclusion where its edges are substantially sharper. To better compare the results, the Edge Spread Functions (ESF) of the estimated strain fields

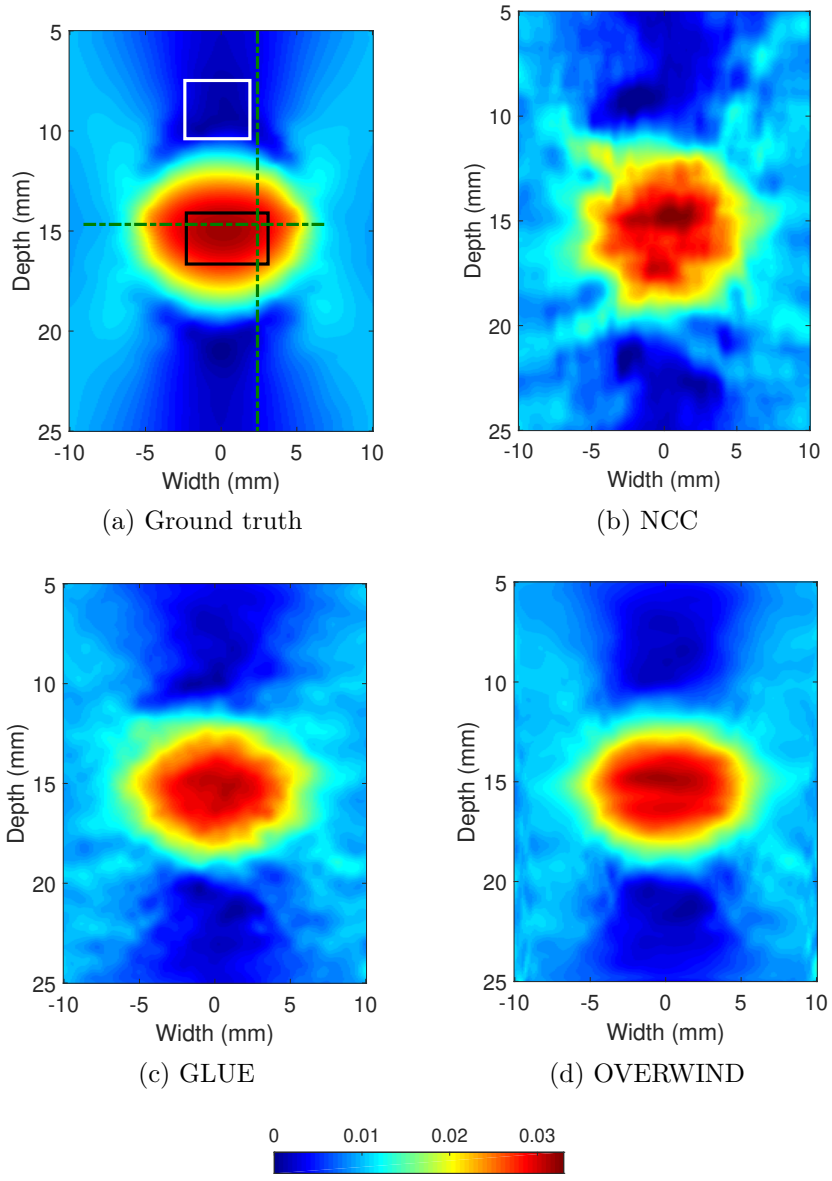


(a) Ground truth (b) NCC

(c) GLUE (d) OVERWIND

Figure 3.3: Strain estimated by three methods in the FEM simulated phantom.

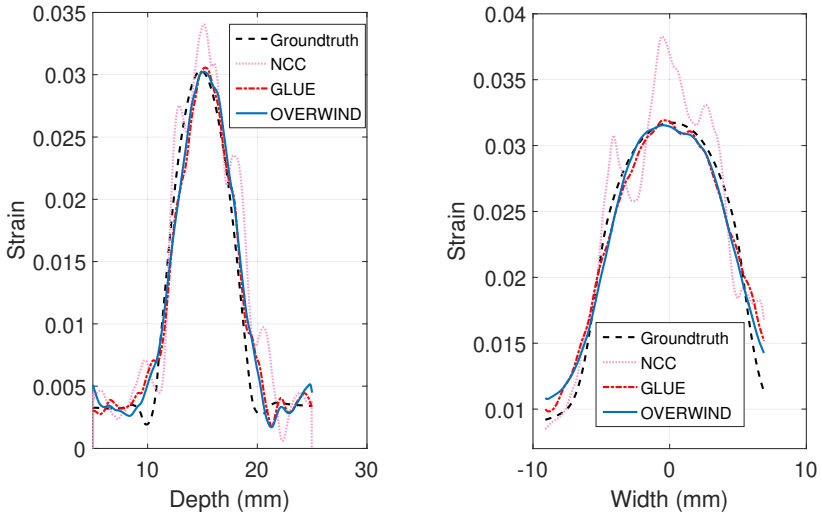


(a) Vertical (b) Horizontal

Figure 3.4: Edge spread function of NCC, GLUE and OVERWIND for the FEM simulated phantom across two perpendicular lines shown in Fig. 3.3 (c).

across two vertical and horizontal lines of Fig. 3.3 (a) are depicted in Fig. 3.4. It is further clarified from these plots that the ESF of OVERWIND is substantially closer to the ground truth as compared to both NCC and GLUE. The ESF of all horizontal and vertical lines in this experiment are shown in the Supplementary Material.

To compare the sensitivity of different methods against noise, we add two levels of Gaussian noise with peak signal-to-noise ratio (PSNR) values of 20 and 16.4 to the simulated RF data. NCC fails to estimate strain given the large energy of noise, and therefore, only the results of GLUE and OVERWIND are shown in Fig. 3.5. It is clear that the strain image of OVERWIND substantially outperforms that of GLUE.

To quantitatively compare the results, the CNR of strain images are shown in Table 3.1. For calculating these values, we ran a Monte Carlo simulation by estimating strains 1000 times with different random noise realizations. The mean and standard deviation (SD) of CNR for these 1000 experiments are reported for different levels of noise. As seen from Figs. 3.3 and 3.5, and Table 3.1 not only OVERWIND outperforms GLUE for each level of noise, but also has more robust performance against increasing the amplitude of noise.

### Phantom Results

For the phantom data, strain images estimated by NCC, GLUE and OVERWIND are shown in Fig. 3.6. The estimated strain by GLUE suffers from artifacts and regularization weights should be increased to remove these artifacts. However, by increasing the regularization weights, more blurriness especially on the edges of the

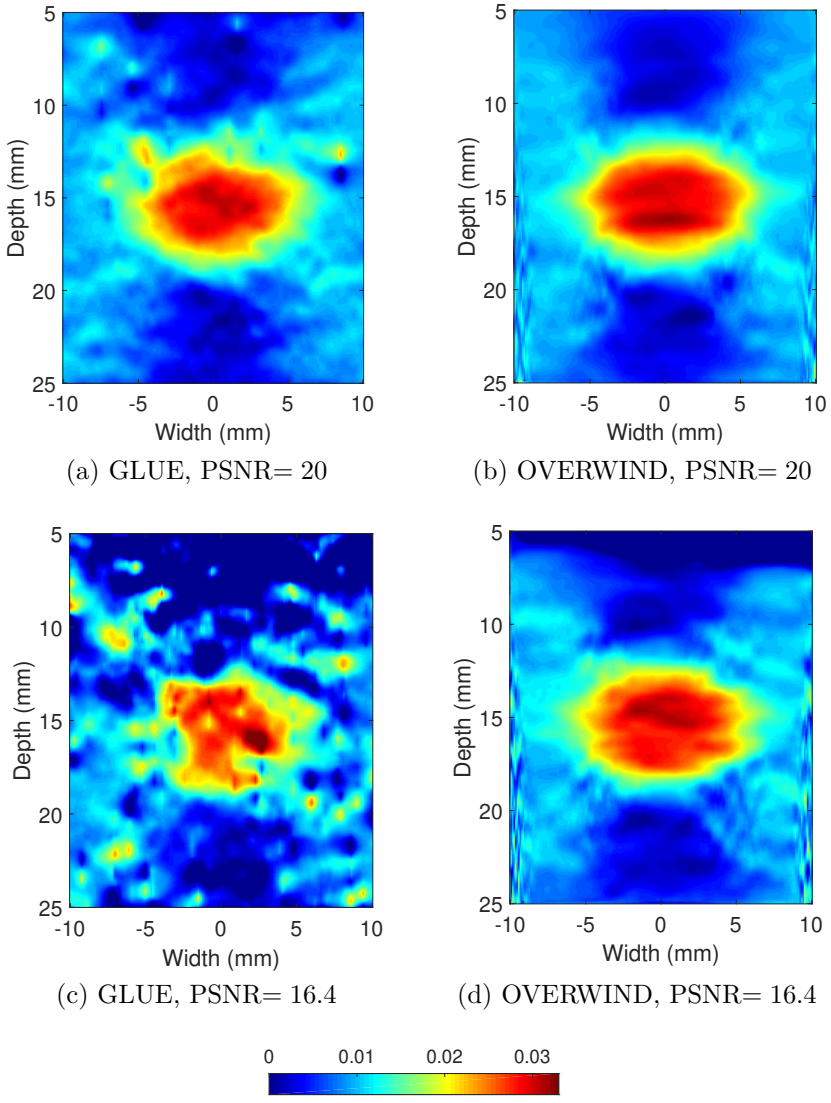


(a) GLUE, PSNR= 20

(b) OVERWIND, PSNR= 20

(c) GLUE, PSNR= 16.4

(d) OVERWIND, PSNR= 16.4

Figure 3.5: Estimated strain images in the FEM simulation experiment by adding Gaussian noise to pre- and post-compressed RF data.

Table 3.1: Mean and standard deviation of CNR for 1000 strain images of the simulated phantom for different methods and noise levels. Windows that are considered for calculating CNR are shown in white and black lines in Fig. 3.3. The mean improvement of OVERWIND compared to GLUE is also reported for each level of noise.

| PSNR | | CNR mean (SD) |
|---|---|---|
| $\infty$ (No noise) | NCC | 49.29 (0) |
| | GLUE | 54.85 (0) |
| | OVERWIND | 58.2 (0) |
| 20 | NCC | fails |
| | GLUE | 50.95 (2.89) |
| | OVERWIND | 56.27 (3.30) |
| 16.4 | NCC | fails |
| | GLUE | fails |
| | OVERWIND | 50.56 (5.06) |

inclusion is generated. OVERWIND produces a much smoother image than other methods while preserving the sharpness of edges. It can be seen from this figure that the strain values at the right and left side of the phantom are not equal. This is caused by applying a compression that is not purely axial and likely contains some in-plane rotation, which is possible in hand-held compressions.

For a comprehensive CNR comparison, the results of histogram analysis are shown in Fig. 3.7. The target and background windows considered for CNR calculation are shown in Fig. 3.6 (a). We have moved the small red window within the large red window to take 9 target windows. At the same time, the small blue window is swiped within the large blue window to consider 24 background windows. CNR is calculated for every combination of target and background windows, resulting in 216 values. Fig. 3.7 shows the distribution of the aforementioned CNR values. It is clear from these histograms that OVERWIND produces strain images with higher CNR. The mean of 216 CNR values are 15.40, 6.31 and 6.28 for OVERWIND, GLUE and NCC, respectively.

### *In-vivo* Results

NCC fails in estimating strains for this *in-vivo* data and therefore only the results of GLUE and OVERWIND are presented in Figs. 3.8, 3.9 and 3.10. While the strain images clearly show the tumor in these three patients, the B-mode image hardly shows the tumor especially in patients 1 and 3.

The OVERWIND strain images are much smoother than GLUE while preserving the sharp edges of the tumors and the veins. For quantitative comparison of two methods, the CNR of the strains are calculated and the results are presented in Table

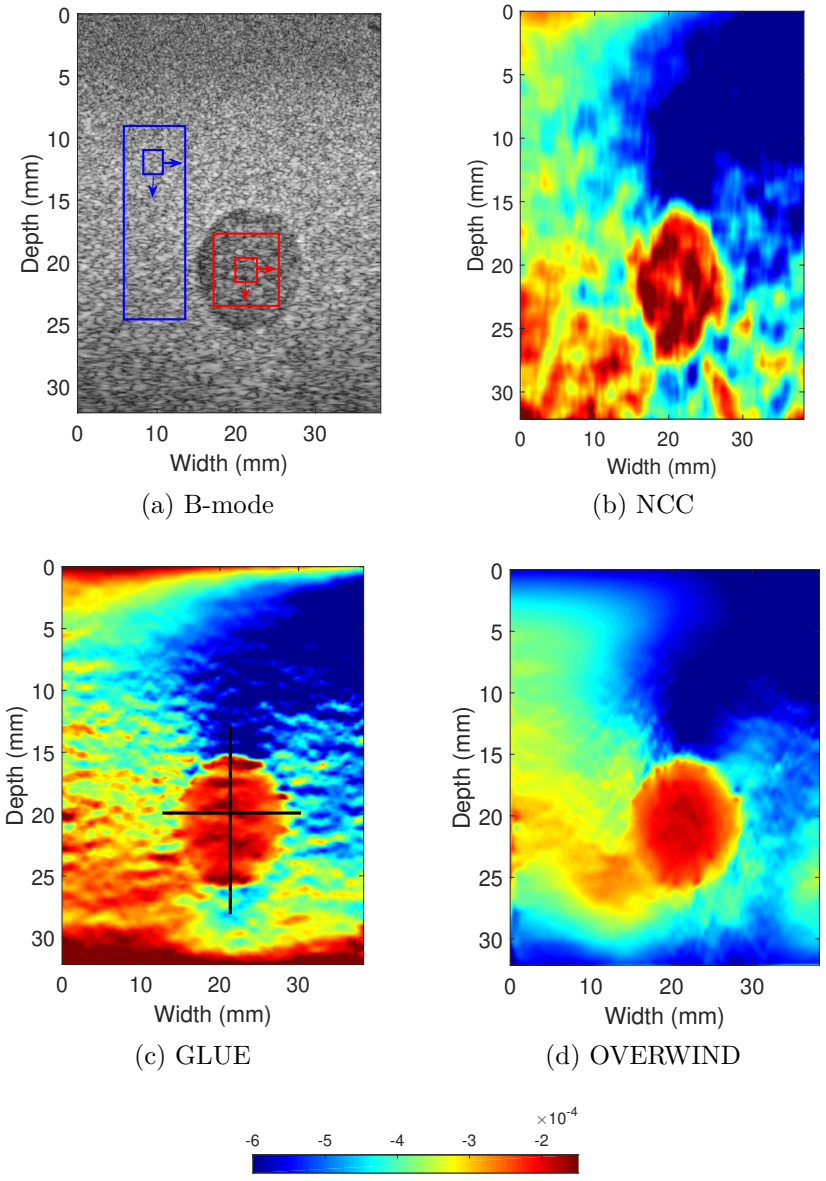


(a) B-mode (b) NCC

(c) GLUE (d) OVERWIND

Figure 3.6: B-mode and strain images of the CIRS phantom.

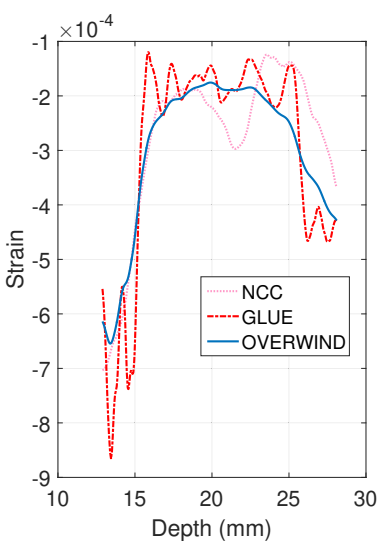


(a) Vertical ESF

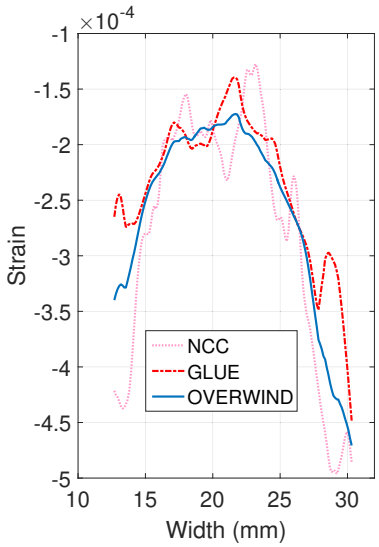


(b) Horizontal ESF

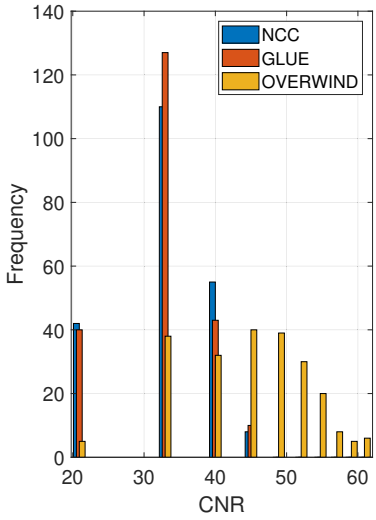


(c) CNR Histogram

Figure 3.7: Edge spread function of estimated strains by NCC, GLUE and OVERWIND in the CIRS phantom experiment across two perpendicular lines specified in Fig. 3.6 (c) are shown in (a) and (b). Histograms of CNR (c) for estimated strains by NCC, GLUE and OVERWIND for all 216 combination of target and background windows that are shown in Fig. 3.6 (a).

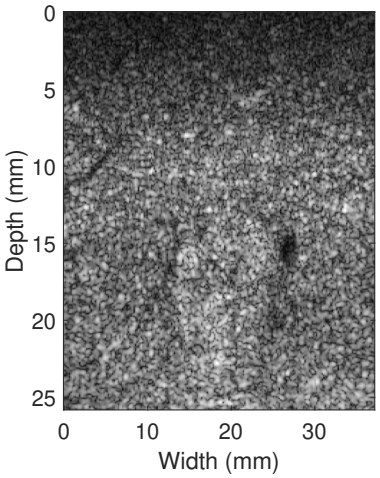


(a) B-mode

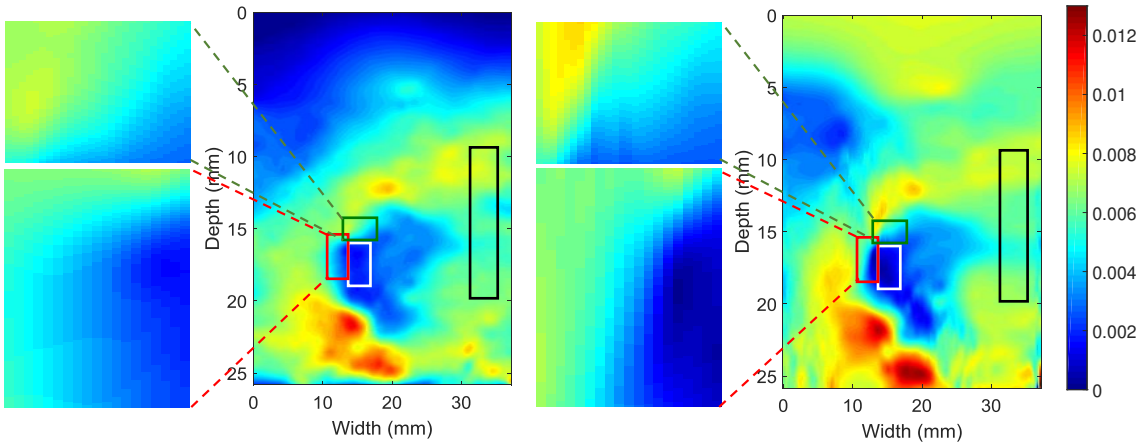


(b) GLUE (c) OVERWIND

Figure 3.8: B-mode and strain images of patient 1 (P1).

3.2, which also corroborate better performance of OVERWIND.

In the last experiment, data collected from patient 3 shows the left anterior branch of portal vein. This vein is marked by the symbol 'A' in Fig. 3.10-(a) and has low pressure. Therefore, it compresses easily during free-hand palpation, which results in high strain values. The boundaries of the veins are substantially sharper in the OVERWIND strain image.

## 3.3 Conclusions

In this chapter we proposed a novel method for real time USE. We coupled the two well-known window-based and regularized optimization-based methods to increase robustness against noise. Another advantage of the proposed method was utilizing the total variation L1 norm regularization instead of the L2 norm regularization, which

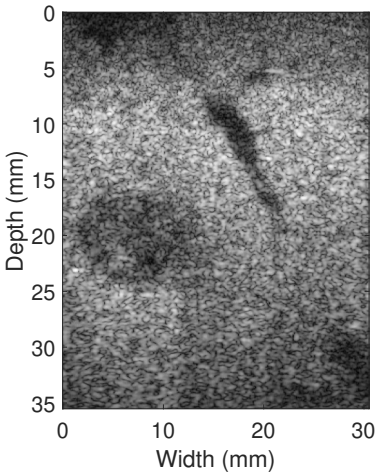


(a) B-mode

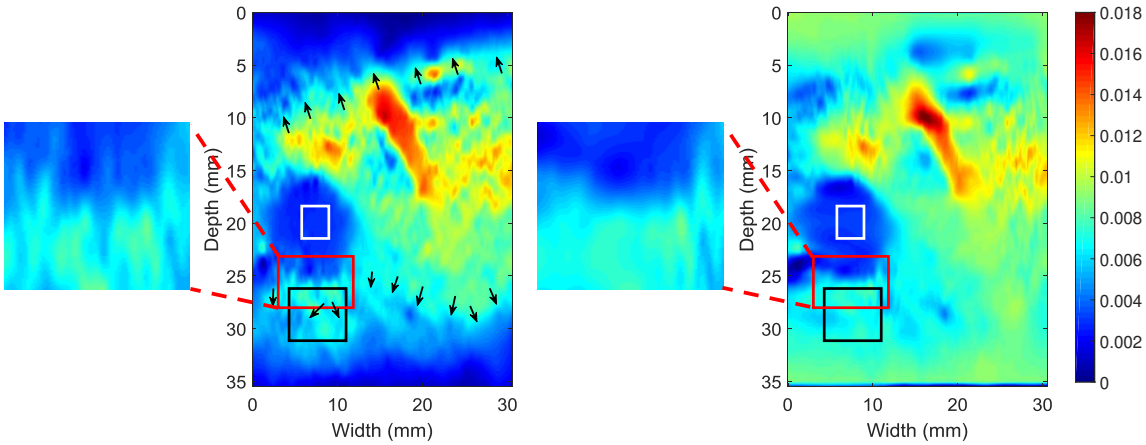


(b) GLUE (c) OVERWIND

Figure 3.9: B-mode and strain images of patient 2 (P2).

Table 3.2: CNR values in calculated strain fields of two patients. Windows that are considered for calculating CNR are shown in Figs. 3.8, 3.9 and 3.10.

| | CNR | |
|---|---|---|
| | OVERWIND | GLUE |
| P1 | 38.11 | 35.39 |
| P2 | 40.81 | 30.89 |
| P3 | 27.28 | 16.53 |

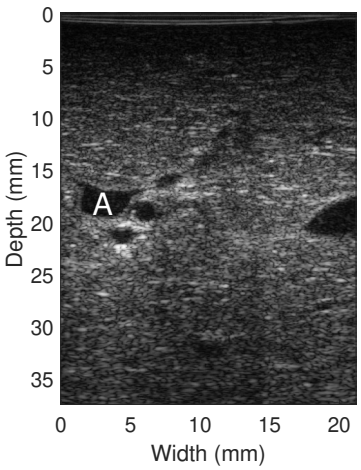


(a) B-mode

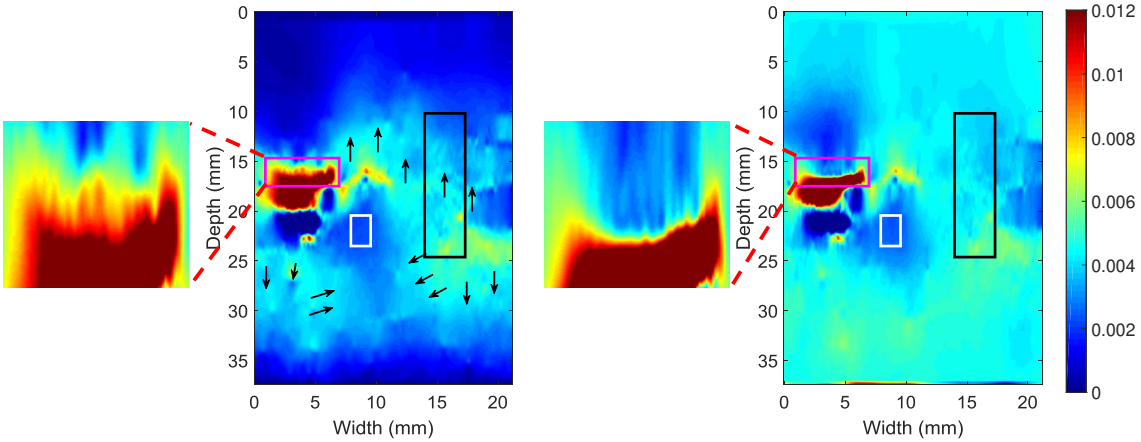


(b) GLUE (c) OVERWIND

Figure 3.10: B-mode and strain images of patient 3 (P3).

results in sharper strain images. We compared the performance of our approach with GLUE and NCC on data collected from simulations, phantom set-ups, and *in-vivo* experiments.

# Chapter 4

# Channel Data for Ultrasound Elastography

**This chapter is based on our published papers [85, 86].**

---

To the best of authors knowledge, all previously developed methods use RF or B-mode data for USE. In this chapter, we propose to use pre-beamformed channel data. An ultrasound image comprises of multiple scan lines (RF lines). For generating each line, an array of transducers transmit the acoustic energy pulse while timing the piezoelectric crystals to focus the beam (as shown with blue curves in Fig.4.1). Reflections are collected by the same piezoelectric crystals and digitized. Based on the classic Nyquist-Shannon sampling theorem, the sampling rate must be at least twice the bandwidth, in order to avoid aliasing [87]. Time gain and time-delay due to transmission are compensated for the sampled data (i.e, channel data) as shown in part A of Fig. 4.1. By integrating data, a RF line is generated as shown in part B of Fig. 4.1. TDE is often performed using RF data, however in this paper we use time-gain and time-delay corrected channel data (shown in section A of Fig. 4.1) instead of RF data (shown in section B of Fig. 4.1). We name our method CGLUE and prove that the error of estimated displacement with CGLUE is less than GLUE.

## 4.1 Methods

Let $I_1$ and $I_2$ of size $(m, n, c)$ be two sets of time-gain and time-delay compensated channel data collected as the tissue undergoing some deformation. $I_{1b}$ and $I_{2b}$ of size $(m, n)$ are the corresponding beamformed RF data. In these data sets, $m$ and $n$ are depth and width of the imaged tissue and $c$ is the number of channels that receive the reflected data. The goal of TDE is estimating the displacement field between these two data sets. In this section, we first briefly review our previous work, GLUE [33], and then present CGLUE. More importantly, we derive an analytically proof of the superiority of CGLUE over GLUE by comparing the error for the estimated TDEs.

In GLUE and CGLUE, the displacements are estimated in two steps as integer and subsample displacement estimates. The initial integer displacement estimates come from DP, which is a recursive optimization based method for image registration. In this method, different integers are nominated for displacement of each RF sample. The cost function incorporates similarity of RF samples and displacement continuity and optimizing this cost function leads to integer displacement of RF samples [78].

### 4.1.1 GLUE: GLobal Ultrasound Elastography

The goal of GLUE is to calculate the subsample displacement part by minimizing the following cost function:

$$\begin{aligned} C(\Delta a_{11}, \Delta l_{11}, \ldots, \Delta a_{mn}, \Delta l_{mn}) = \quad & \sum_{j=1}^{n} \sum_{i=1}^{m} \{D(i, a_{ij}, \Delta a_{ij}, j, l_{ij}, \Delta l_{ij}) \\ & + R(i, a_{ij}, \Delta a_{ij}, j, l_{ij}, \Delta l_{ij})\} \end{aligned} \tag{4.1}$$

where the data term $D$ is:

$$D(i, a_{ij}, \Delta a_{ij}, j, l_{ij}, \Delta l_{ij}) = [I_{1b}(i, j) - I_{2b}(i + a_{ij} + \Delta a_{ij}, j + l_{ij} + \Delta l_{ij})]^2 \tag{4.2}$$

and the regularization term $R$ is:

$$\begin{aligned} R(i, a_{ij}, \Delta a_{ij}, j, l_{ij}, \Delta l_{ij}) = \quad & \alpha_1 (a_{ij} + \Delta a_{ij} - a_{i-1j} - \Delta a_{i-1j})^2 \\ & + \alpha_2 (a_{ij} + \Delta a_{ij} - a_{ij-1} - \Delta a_{ij-1})^2 \\ & + \beta_1 (l_{ij} + \Delta l_{ij} - l_{i-1j} - \Delta l_{i-1j})^2 \\ & + \beta_2 (l_{ij} + \Delta l_{ij} - l_{ij-1} - \Delta l_{ij-1})^2. \end{aligned} \tag{4.3}$$

In these equations, $I_{1b}$ and $I_{2b}$ are pre- and post-compressed beamformed RF data of size $m \times n$. The symbols $a_{ij}$ and $l_{ij}$ are axial and lateral integer displacements for sample $(i, j)$ that are estimated by DP while $\Delta a_{ij}$ and $\Delta l_{ij}$ are subsample axial and lateral displacements that should be calculated. Finally, $\alpha_1$, $\alpha_2$, $\beta_1$ and $\beta_2$ are regularization parameters.

In the next section, CGLUE is proposed that modifies the data term by utilizing channel data instead of beamformed data.

### 4.1.2 CGLUE: Channel data for GLobal Ultrasound Elastography

By considering pre-beamformed channel data, the data term of Eq. (4.2) is replaced by

$$D(i, a_{ij}, \Delta a_{ij}, j, l_{ij}, \Delta l_{ij}) = \tfrac{1}{c} \sum_{k=1}^{c} \Big( I_1(i, j, k) - I_2(i + a_{ij} + \Delta a_{ij}, j + l_{ij} + \Delta l_{ij}, k) \Big)^2.$$

Optimizing the cost function based on the proposed data term is not a trivial problem due to nonlinearity of $I_2$. To linearize $I_2$ with respect to unknown variables, we replace

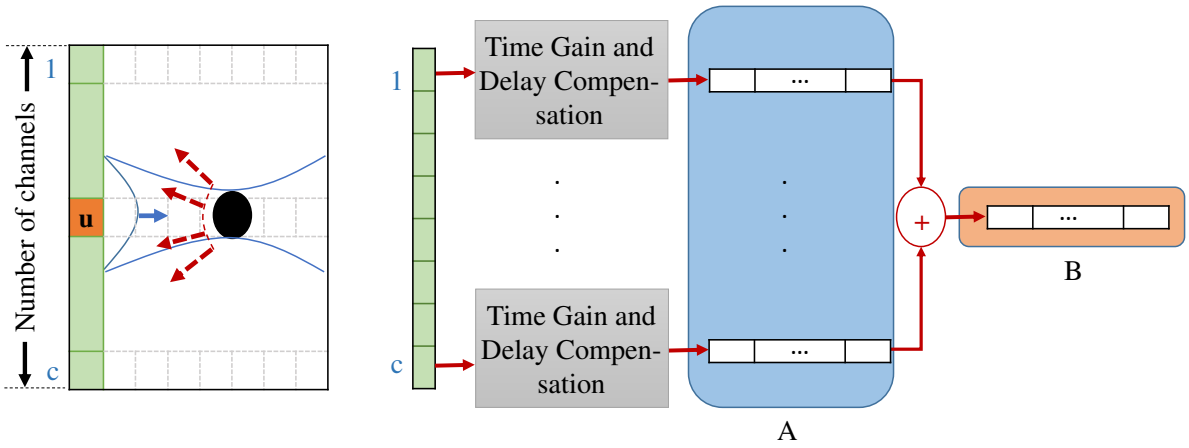


Figure 4.1: Schematic of transmission and receive of signal for reconstructing one line of RF data.

$I_2(i + a_{ij} + \Delta a_{ij}, j + l_{ij} + \Delta l_{ij}, k)$ with its first order Taylor series expansion around $(i+a_{ij}, j+l_{ij}, k)$. Furthermore, to simplify the notation, we denote $I_2(i+a_{ij}, j+l_{ij}, k)$ as $I_2(.)$, so the data term can be rewritten as

$$D(i, a_{ij}, \Delta a_{ij}, j, l_{ij}, \Delta l_{ij}) = \frac{1}{c} \sum_{k=1}^{c} \Big( I_1(i, j, k) - I_2(.) - \Delta a_{ij} I'_{2a}(.) - \Delta l_{i,j} I'_{2l}(.) \Big)^2 \tag{4.4}$$

where $I'_{2a}(.)$ and $I'_{2l}(.)$ are derivatives of $I_2$ in the axial and lateral directions, respectively.

The regularization term in Eq. (4.3) reduces estimation variance at the cost of increased bias by penalizing the difference between $a_{ij} + \Delta a_{ij}$ and $a_{i-1j} - \Delta a_{i-1j}$, which leads to an underestimated displacement estimation. Therefore, as proposed in [2, 74], we consider $\varepsilon_a$ and $\varepsilon_l$ in the regularization term, where $\varepsilon_a$ is the average of integer axial displacement difference between subsequent samples $i$ and $i-1$ and $\varepsilon_l$ is the average of integer lateral displacement difference between samples $j$ and $j-1$ which are available from DP. Therefore, the regularization term can be modified as

$$\begin{aligned} R(i, a_{ij}, \Delta a_{ij}, j, l_{ij}, \Delta l_{ij}) = \quad & \alpha_1 (a_{ij} + \Delta a_{ij} - a_{i-1j} - \Delta a_{i-1j} - \varepsilon_a)^2 \\ & + \alpha_2 (a_{ij} + \Delta a_{ij} - a_{ij-1} - \Delta a_{ij-1})^2 \\ & + \beta_1 (l_{ij} + \Delta l_{ij} - l_{i-1j} - \Delta l_{i-1j})^2 \\ & + \beta_2 (l_{ij} + \Delta l_{ij} - l_{ij-1} - \Delta l_{ij-1} - \varepsilon_l)^2. \end{aligned} \tag{4.5}$$

By considering the cost function $C$ as a summation of data and regularization terms that are proposed in Eqs. (4.4) and (4.5), differentiating it with respect to $\Delta a_{ij}$ and $\Delta l_{ij}$, and stacking all $2mn$ unknown parameters in a vector as

$$\Delta d_{2m \times n} = [\Delta a_{11}, \Delta l_{11} \Delta a_{12}, \Delta l_{12}, \cdots, \Delta a_{mn}, \Delta l_{mn}]^T,$$

we have

$$\underbrace{(H+V)}_{X}\Delta d = \underbrace{\frac{1}{c}\sum_{k=1}^{c}(P\mu) - Vd - b \otimes \begin{bmatrix}\varepsilon_a \\ \varepsilon_l\end{bmatrix}}_{y}, \tag{4.6}$$

where $X$ and $y$ are two known matrices, $\otimes$ is Kronecker tensor product and $\Delta d$ can be calculated by the lower-upper (LU) decomposition (e.g. the $X\backslash y$ command in MATLAB).

The matrix $V$ is a $2mn \times 2mn$ matrix as

$$V = \begin{bmatrix} Q & R & 0 & & & & \\ R & S & R & 0 & & \mathbf{0} & \\ 0 & R & S & R & 0 & & \\ & \ddots & & \ddots & & \ddots & \\ & & 0 & R & S & R & 0 \\ & \mathbf{0} & & \ddots & R & S & R \\ & & & & 0 & R & Q \end{bmatrix}$$

in which $Q, S$ are pentadiagonal matrices as shown in Eqs. (4.7), (4.8) and $R$ is a diagonal matrix as

$$R = \mathrm{diag}\{-\alpha_1, -\beta_1, \cdots, -\alpha_1, -\beta_1\}.$$

The matrix $H$ is a diagonal matrix as

$$H = \mathrm{diag}\{h(1,1), \cdots, h(1,n), \cdots, h(m,1), \cdots, h(m,n)\}$$

where $h(i,j)$ is a $2 \times 2$ matrix as

$$h(i,j) = \frac{1}{c}\begin{bmatrix} \sum_{k=1}^{c}(I'_{2a}(.))^2 & \sum_{k=1}^{c}(I'_{2a}(.)I'_{2l}(.)) \\ \sum_{k=1}^{c}(I'_{2a}(.)I'_{2l}(.)) & \sum_{k=1}^{c}(I'_{2l}(.))^2 \end{bmatrix}.$$

$P$ is a diagonal matrix given by

$$P = \mathrm{diag}\{e(1,1), \cdots, e(1,n), \cdots, e(m,1), \cdots, e(m,n)\}.$$

$e(i,j)$ is a matrix of size $2 \times 2$ as

$$e(i,j) = \begin{bmatrix} I'_{2a}(.) & 0 \\ 0 & I'_{2l}(.) \end{bmatrix}.$$

$\mu$ is a vector as

$$\mu = [g_{1,1}, g_{1,2}, \cdots, g_{m,n}]^{\mathrm{T}} \otimes [1,1]^{\mathrm{T}},$$

$g_{i,j}$ is difference of two images as

$$g_{i,j} = I_1(i+k, j+r) - I_2(.)$$

and $\otimes$ is Kronecker tensor product.

The vector $d$ contains integer displacements as

$$d = [a_{11}, l_{11}, a_{12}, l_{12}, \cdots, a_{mn}, l_{mn}]^{\mathrm{T}}$$

and finally the vector $b$ is a $mn \times mn$ vector as

$$b = [1, 0, \cdots, 0, -1]^{\mathrm{T}}.$$

$$Q = \begin{bmatrix}
\alpha_1+\alpha_2 & 0 & -\alpha_2 & 0 & & & & & \\
0 & \beta_1+\beta_2 & 0 & -\beta_2 & 0 & & & \mathbf{0} & \\
-\alpha_2 & 0 & \alpha_1+2\alpha_2 & 0 & -\alpha_2 & 0 & & & \\
0 & -\beta_2 & 0 & \beta_1+2\beta_2 & 0 & -\beta_2 & 0 & & \\
 & \ddots & \ddots & & \ddots & & \ddots & \ddots & \\
 & & 0 & -\alpha_2 & 0 & \alpha_1+2\alpha_2 & 0 & -\alpha_2 & 0 \\
 & & & 0 & -\beta_2 & 0 & \beta_1+2\beta_2 & 0 & -\beta_2 \\
 & \mathbf{0} & & & 0 & -\alpha_2 & 0 & \alpha_1+\alpha_2 & 0 \\
 & & & & & 0 & -\beta_2 & 0 & \beta_1+\beta_2
\end{bmatrix} \tag{4.7}$$

$$S = \begin{bmatrix}
2\alpha_1+\alpha_2 & 0 & -\alpha_2 & 0 & & & & & \\
0 & 2\beta_1+\beta_2 & 0 & -\beta_2 & 0 & & & \mathbf{0} & \\
-\alpha_2 & 0 & 2\alpha_1+2\alpha_2 & 0 & -\alpha_2 & 0 & & & \\
0 & -\beta_2 & 0 & 2\beta_1+2\beta_2 & 0 & -\beta_2 & 0 & & \\
 & \ddots & \ddots & & \ddots & & \ddots & \ddots & \\
 & & 0 & -\alpha_2 & 0 & 2\alpha_1+2\alpha_2 & 0 & -\alpha_2 & 0 \\
 & & & 0 & -\beta_2 & 0 & 2\beta_1+2\beta_2 & 0 & -\beta_2 \\
 & \mathbf{0} & & & 0 & -\alpha_2 & 0 & 2\alpha_1+\alpha_2 & 0 \\
 & & & & & 0 & -\beta_2 & 0 & 2\beta_1+\beta_2
\end{bmatrix} \tag{4.8}$$

### 4.1.3 Error Analysis

To analytically compare the errors of GLUE and CGLUE, we derive equations for the error of TDE as functions of noise in the data. Let $\hat{d}_{ij} = (\hat{a}_{ij}, \hat{l}_{ij})$ denote the ground truth displacement of sample $(i, j)$. For simplicity of mathematical derivations, we assume that the motion is only in the axial direction and $\hat{l}_{ij} = 0$ without loss of generality. Also by assuming the ultrasound noise to be an additive noise [88, 89], the

data at sample $(i, j, k)$ is

$$\begin{aligned} I_1(i,j,k) &= \hat{I}(i,j,k) + n_1(i,j,k) \\ I_2(i,j,k) &= \hat{I}(i - \hat{a}_{ij}, j, k) + n_2(i,j,k) \end{aligned} \tag{4.9}$$

where $n_1(i, j, k)$ and $n_2(i, j, k)$ can have any distribution with expected values of $\mu_1, \mu_2$ and variances of $\sigma_1, \sigma_2$. In this section we denote the estimated displacements as $a_{ij}$ and $l_{ij}$, which represent summation of integer and subsample displacements.

**GLUE Error**

In beamforming the channel data corresponding to one element, the collected data with different channels should be time-delayed and time-gained with respect to their spatial distances from the element. The beamformed data is generated by adding the time-delayed and time-gained data across all channels. Since time-delay and time-gain compensation are linear operations and as such do not change the distribution of noise, therefore we consider beamforming as summation of channel data as follows

$$\begin{aligned} I_{1b}(i,j) &= \sum_{k=1}^{c} I_1(i,j,k) = \sum_{k=1}^{c} \hat{I}(i,j,k) + n_1(i,j,k) \\ I_{2b}(i,j) &= \sum_{k=1}^{c} I_2(i,j,k) = \sum_{k=1}^{c} \hat{I}(i - \hat{a}_{i,j}, j, k) + n_2(i,j,k). \end{aligned} \tag{4.10}$$

The cost function for GLUE can be written as

$$\begin{aligned} C &= \sum_{j=1}^{n} \sum_{i=1}^{m} \Big( I_{1b}(i,j) - I_{2b}(i + a_i, j) \Big)^2 \\ &= \sum_{j=1}^{n} \sum_{i=1}^{m} \left[ \sum_{k=1}^{c} \Big( \hat{I}(i,j,k) + n_1(i,j,k) - \hat{I}(i + a_{ij} - \hat{a}_{ij}, j, k) - n_2(i + a_{ij}, j, k) \Big) \right]^2 \\ &\quad + R. \end{aligned} \tag{4.11}$$

By applying the first order Taylor series approximation for nonlinear functions, we have

$$\begin{aligned} C = \sum_{j=1}^{n} \sum_{i=1}^{m} \Bigg[ & \sum_{k=1}^{c} \Big( \hat{I}(i,j,k) + n_1(i,j,k) - \hat{I}(i,j,k) - (a_{ij} - \hat{a}_{ij}) \hat{I}'_a(i,j,k) \\ & - n_2(i + a_{ij}, j, k) \Big) \Bigg]^2 + R. \end{aligned} \tag{4.12}$$

By differentiating the cost function and setting the derivative to zero, we have

$$a_{ij} = \hat{a}_{ij} + \frac{\sum_{k=1}^{c} n_1(i,j,k) - n_2(i + a_{ij}, j, k)}{\sum_{k=1}^{c} \hat{I}'_a(i,j,k)}. \tag{4.13}$$

The expected value and variance of the $a_{i,j}$ at sample $(i, j)$ are

$$\begin{aligned} E_g[a_{ij}] &= \hat{a}_{ij} + \frac{c(\mu_1 - \mu_2)}{\sum_{k=1}^{c} \hat{I}'_a(i,j,k)} \\ var_g[a_{ij}] &= \frac{c(\sigma_1 + \sigma_2)}{\Big(\sum_{k=1}^{c} \hat{I'}_a(i,j,k)\Big)^2}. \end{aligned} \tag{4.14}$$

**CGLUE Error**

Considering Eq. (4.9), the cost function of CGLUE is

$$\begin{aligned} C &= \frac{1}{c} \sum_{j=1}^{n} \sum_{i=1}^{m} \sum_{k=1}^{c} \Big(I_1(i,j,k) - I_2(i + a_{ij}, j, k)\Big)^2 + R \\ &= \frac{1}{c} \sum_{j=1}^{n} \sum_{i=1}^{m} \sum_{k=1}^{c} \Big(\hat{I}(i,j,k) + n_1(i,j,k) - \hat{I}(i + a_{ij} - \hat{a}_{ij}, j, k) - n_2(i + a_{ij}, j, k)\Big)^2\Big) \end{aligned} \tag{4.15}$$

Following the same approach as the one used in previous section for estimating the displacement, we have

$$a_{ij} = \hat{a}_{ij} + \frac{\sum_{k=1}^{c} \hat{I}'_a(i,j,k)\Big(n_1(i,j,k) - n_2(i + a_{ij}, j, k)\Big)}{\sum_{k=1}^{c} \hat{I}'^2_a(i,j,k)}. \tag{4.16}$$

The expected value and variance of the $a_{ij}$ are

$$\begin{aligned} E_c[a_{ij}] &= \hat{a}_{ij} + \frac{(\mu_1 - \mu_2) \sum_{k=1}^{c} \hat{I}'_a(i,j,k)}{\sum_{k=1}^{c} \hat{I}'^2_a(i,j,k)} \\ var_c[a_{ij}] &= \frac{\sigma_1 + \sigma_2}{\sum_{k=1}^{c} \hat{I}'^2_a(i,j,k)}. \end{aligned} \tag{4.17}$$

**Statistical error analysis**

To compare the expected values and variances, we rewrite $(\sum_{k=1}^{c} \hat{I'}_a(i,j,k))^2$ as $(\mathbf{1}.\hat{I'}_a(i,j))^2$ where $\mathbf{1}$ and $\hat{I'}_a(i,j)$ are vectors of size $1 \times c$ as $\mathbf{1} = [1, \ldots, 1]$ and $\hat{I'}_a(i,j) = [\hat{I'}_a(i,j,1), \ldots, \hat{I'}_a(i,j,c)]$. The operator '.' is the inner product of the two vectors. According to Cauchy Schwarz inequality we have

$$\begin{aligned} \Big(\sum_{k=1}^{c} \hat{I'}_a(i,j,k)\Big)^2 &= \Big(\mathbf{1}.\hat{I'}_a(i,j)\Big)^2 \\ &\leq \Big(\sum_{k=1}^{c} 1^2\Big)\Big(\sum_{k=1}^{c} \hat{I}'^2_a(i,j,k)\Big) = c \sum_{k=1}^{c} \hat{I}'^2_a(i,j,k), \end{aligned} \tag{4.18}$$

therefore

$$E_c[a_{ij}] = \hat{a}_{ij} + \frac{(\mu_1 - \mu_2)\sum_{k=1}^{c} \hat{I}'_a(i,j,k)}{\sum_{k=1}^{c} \hat{I}'^2_a(i,j,k)} \leq \hat{a}_{ij} + \frac{c(\mu_1 - \mu_2)}{\sum_{k=1}^{c} \hat{I}'_a(i,j,k)} = E_g[a_{ij}].$$

and also

$$var_c[a_{ij}] = \frac{\sigma_1 + \sigma_2}{\sum_{k=1}^{c} \hat{I}'^2_a(i,j,k)} \leq \frac{c(\sigma_1 + \sigma_2)}{\Big(\sum_{k=1}^{c} \hat{I}'_a(i,j,k)\Big)^2} = var_g[a_{ij}].$$

### 4.1.4 Data Acquisition

In this section, the data that is utilized in different experiments of this chapter are described and then results of CGLUE are compared with GLUE in Results Section to illustrate improved performance of the CGLUE. For phantom and *ex-vivo* data where ground truth is not known, the bias and variance of the error cannot be compared quantitatively. However, we know that the strain maps should not have large fluctuations in a homogeneous medium as shown in the FEM and analytical strain maps. For the sake of comparison, the CNR is used to provide a quantitative mean for assessing the proposed method according to [90]

$$\text{CNR} = 20\log_{10}\left(\frac{2(\bar{s}_b - \bar{s}_t)^2}{\sigma_b^2 + \sigma_t^2}\right), \tag{4.19}$$

where $\bar{s}_t$ and $\bar{s}_b$ are the spatial strain averages of the target and background, $\sigma_b^2$ and $\sigma_t^2$ are the spatial strain variances of the target and background, respectively [7].

For estimating the axial strain, the displacement field should be differentiated. To reduce noise effect of differentiating, it is common to use LSQ estimation for strain estimating. For estimating strain of each sample, a few neighboring samples in a window of size $\rho$ should be considered and a line is fitted to their displacements. The tangent of the line is considered as the strain for the middle sample. Considering more data points for least square makes the strain smooth at the cost of losing resolution. For each experiment, three different window sizes (with $\rho = 3$, $\rho = 35$ and $\rho = 65$) are utilized for least square estimation to illustrate the superior performance of the CGLUE.

#### Simulation Data

A simulated phantom is generated by utilizing the Field II ultrasound simulation software [73] by randomly distributing slightly more than 10 scatterers per $mm^3$ to satisfy the Rayleigh scattering regime. The simulated phantom is homogeneous with a Young's modulus of 16 $kPa$. Two cylindrical inclusions with Young's modulus of 40 $kPa$ and 70 $kPa$ are included in the phantom. For compressing the phantom and

computing its ground truth displacement, FEM-based deformations are computed using the ABAQUS software package (Johnston, RI, USA) with mesh size of 0.05 $mm^2$. It should be mentioned that we had to interpolate the position of scatterers to generate the ground truth for the deformed digital phantom. However, this interpolation itself can introduce bias and variance, which is inevitable for any FEM simulation. Therefore, to overcome this issue, we have simulated another phantom with four uniform layers wherein the displacements can be calculated analytically (without FEM) with Poisson ratio of 0.49 to test the validity of the results of GLUE and CGLUE. Ultrasound images are simulated utilizing the Field II software. The probe consists of 192 elements with width of 0.22 mm and height of 5 mm for each element and also kerf of 0.05 mm. For each transmission, the reflected data is recorded by 64 channels. The center and sampling frequencies are 8 MHz and 100 MHz, respectively.

### Phantom Data

The phantom data is acquired from a tissue mimicking breast phantom (059 tissue mimicking breast phantom, CIRS tissue simulation & phantom technology, Norfolk, VA, USA) using an E-Cube R12 ultrasound machine (Alpinion, Bothell, WA, USA) with a L3-12H probe at the center frequency of 11.5 MHz and sampling frequency of 40 MHz.

### *Ex-vivo* Data

To highlight the improved performance of CGLUE, an *ex-vivo* experiment is organized by placing a small piece of olive in a lamb liver. We purchased a fresh liver from a local butcher and made a very small hole in the liver. We then inserted a small piece of olive with roughly size of $(10 \times 5 \times 5)$ $mm^3$ into the liver through the hole. The data are collected by E-Cube R12 ultrasound machine (Alpinion, Bothell, WA, USA) with a L3-12H probe at the center frequency of 11.5 MHz and a sampling frequency of 40 MHz.

## 4.2 Results

### Simulation Results

The time delay profile for the simulated phantom is estimated by GLUE and CGLUE and the strain is estimated by the LSQ method for windows of lengths 3, 35 and 65. As shown in Fig. 4.2, CGLUE exhibits substantially better performance in all scenarios.

To provide a better comparison, we illustrate the Edge Spread Function (ESF) of the estimated strains across a vertical line shown in Fig. 4.2 (a). As it is clear form Fig. 4.3, the ESF of the CGLUE is closer to the ground truth as compared to GLUE in all cases. The noticeable point is that the estimated strain by CGLUE with $\rho = 3$

Table 4.1: Mean and variance of strain estimation error for GLUE and CGLUE with different levels of noise for FEM simulation study. For each level of noise the experiment is repeated 100 times and the reported values in this table are averages of the 100 experiments.

| SNR (dB) | | ME$\times 10^5$ | VE$\times 10^7$ |
|---|---|---|---|
| $\infty$ | GLUE | -28.23 | 10.69 |
| | CGLUE | -7.14 | 3.12 |
| 40 | GLUE | -28.95 | 10.81 |
| | CGLUE | -7.2 | 3.2 |
| 30 | GLUE | -29.2 | 10.97 |
| | CGLUE | -7.3 | 3.21 |
| 25 | GLUE | -41.2 | 11.04 |
| | CGLUE | -14.3 | 3.4 |

is smooth, however, the result of GLUE for $\rho = 3$ has much more fluctuations and increasing $\rho$ has a significant smoothing effect on the estimated strain.

We also have added different levels of noise to channel data and have calculated Mean of estimation Error (ME) and Variance of estimation Error (VE) based on the following formulas

$$\begin{aligned} \text{ME} &= \frac{\sum_{i=1}^{m}\sum_{j=1}^{n} S_e(i,j) - S_g(i,j)}{m \times n}, \\ \text{VE} &= \frac{\sum_{i=1}^{m}\sum_{j=1}^{n} (S_e(i,j) - S_g(i,j))^2}{m \times n} - \text{ME}^2, \end{aligned} \tag{4.20}$$

where $S_e$ and $S_g$ are estimated and ground truth strains and $m$, $n$ are the axial and lateral size of data. Table 4.1 shows bias and variance of estimation error for different levels of noise and different methods. For each level of noise, we have repeated the experiment 100 times and the results are reported in Table 4.1.

The estimated strain profiles for the simulated phantom with four uniform layers are shown in Fig. 4.4. ESFs across a vertical line are also shown in Fig. 4.5 which verify a low bias and a low variance of the TDE error corresponding to CGLUE and GLUE.

Similar to the previous experiment, we have added different levels of noise to the channel data and have calculated bias and variance of the strain error according to Eq. (4.20). Table 4.2 shows bias and variance of estimation error for GLUE and CGLUE with different levels of noise. For each level of noise, we have repeated the experiment 100 times and the results are reported in Table 4.2.

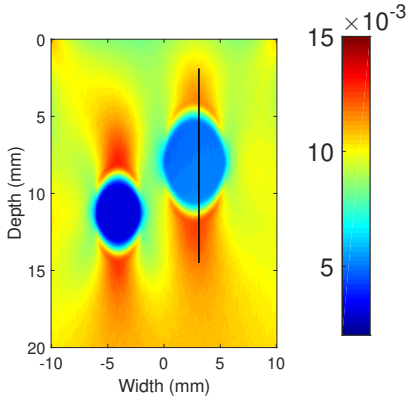


(a) Ground truth

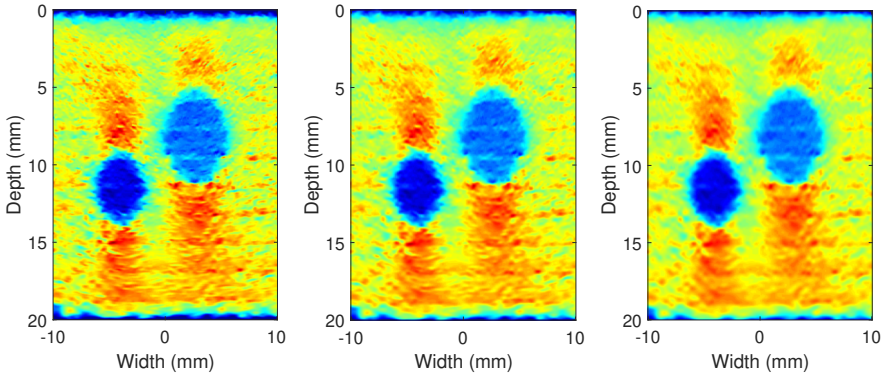


(c) GLUE, $\rho = 3$ (d) GLUE, $\rho = 35$ (e) GLUE, $\rho = 65$

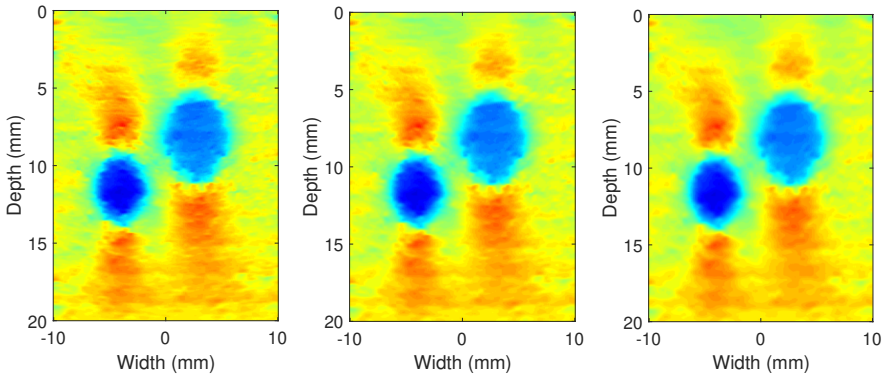


(f) CGLUE, $\rho = 3$ (g) CGLUE, $\rho = 35$ (h) CGLUE, $\rho = 65$

Figure 4.2: Strain images of the simulation phantom calculated using GLUE and CGLUE.

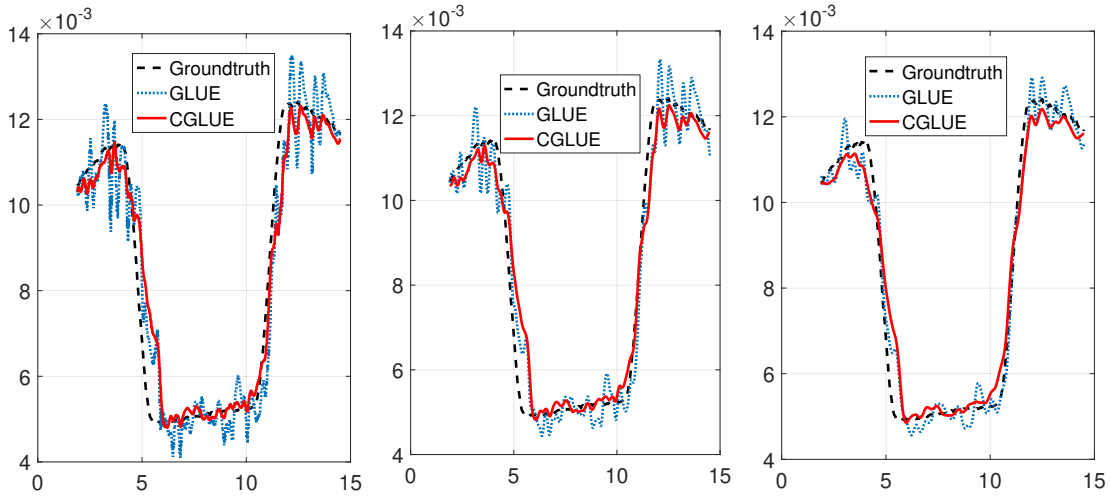


(a) $\rho = 3$ (b) $\rho = 35$ (c) $\rho = 65$

Figure 4.3: Strain profiles of the simulated phantom across the vertical line in Fig. 4.2(a) calculated by GLUE and CGLUE. Windows of length 3, 35 and 65 are used for estimating strain by LSQ in (a), (b) and (c), respectively.

### Phantom Results

The strain of phantom data is illustrated in Fig. 4.6. Three different windows are considered for LSQ with sizes of 3, 35 and 65. CGLUE provides a lower variance strain error estimation than that of GLUE in all cases. This is important as the background and inclusions of the experimental phantoms are uniform and linear elastic materials. Moreover, the smoother strain field of CGLUE for $\rho = 3$ shows that the corresponding TDE profile has lower variance than TDE profile for GLUE. The ESF profiles that are calculated across the yellow line in Fig. 4.6 (a) are also shown in Fig. 4.7 clarifies that CGLUE exhibits better performance than GLUE for all LSQ window sizes by generating smoother results. The length of LSQ windows do not impact results of CGLUE as much as GLUE, which implies a less noisy TDE field by CGLUE. To make sure that low variance strain error estimation does not result in a large bias error, the CNR is utilized to show the contrast between lesion and background. The calculated CNRs are reported in Table 4.3.

### *Ex-vivo* Results

Similar to the previous sections, three different windows are considered for estimating strain. The windows of LSQ have sizes of 3, 35 and 65. CGLUE displays the olive piece more clearly than GLUE by providing a higher contrast and lower noise in the background.

The ESFs of the estimated strains across the vertical line in Fig. 4.8 (a) are also shown in Fig. 4.9. According to Fig. 4.9, the TDE field obtained from CGLUE is much less noisy than the TDE field obtained from GLUE, since the resulted strain

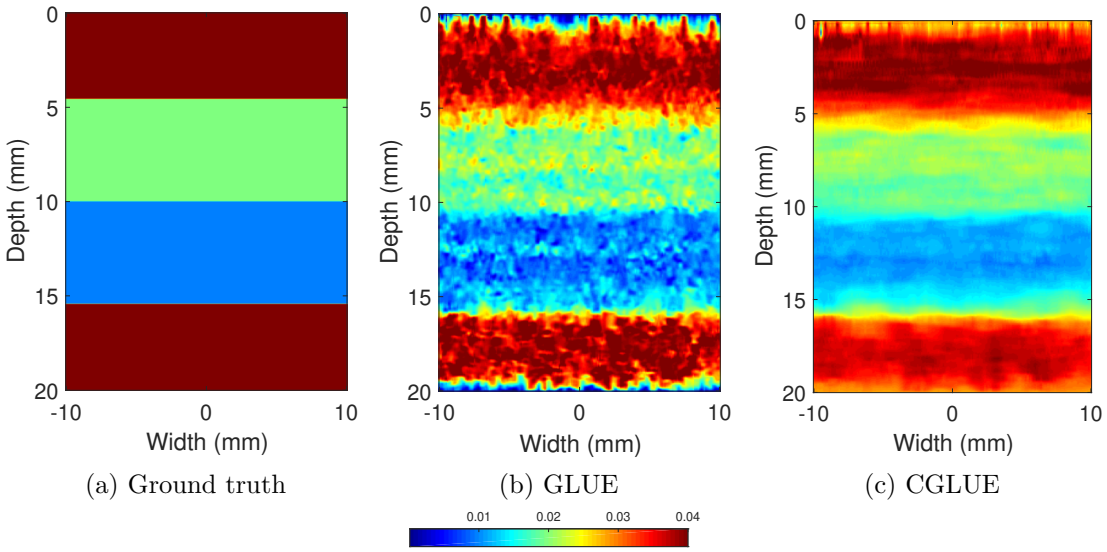


(a) Ground truth (b) GLUE (c) CGLUE

Figure 4.4: Ground truth strain of the simulated phantom is shown in (a). Estimated strains by GLUE and CGLUE are shown in (b) and (c), respectively.

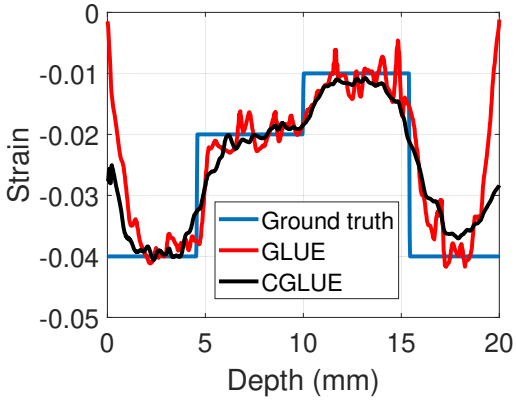


(a)

Figure 4.5: Strain profiles of the simulated uniform phantom across a vertical line, calculated by GLUE and CGLUE.

Table 4.2: Mean and variance of strain estimation error for different levels of noise for 4-layers uniform simulation study. For each level of noise, the experiment is repeated 100 times and the reported values in this table are averages of all experiments.

| SNR (dB) | | ME$\times 10^5$ | VE$\times 10^5$ |
|---|---|---|---|
| $\infty$ | GLUE | 30.45 | 3.20 |
| | CGLUE | -2.64 | 2.94 |
| 40 | GLUE | 30.51 | 3.21 |
| | CGLUE | -3.90 | 2.98 |
| 30 | GLUE | 30.79 | 3.26 |
| | CGLUE | -4.33 | 2.92 |
| 25 | GLUE | 46.34 | 3.63 |
| | CGLUE | 17.08 | 3.04 |

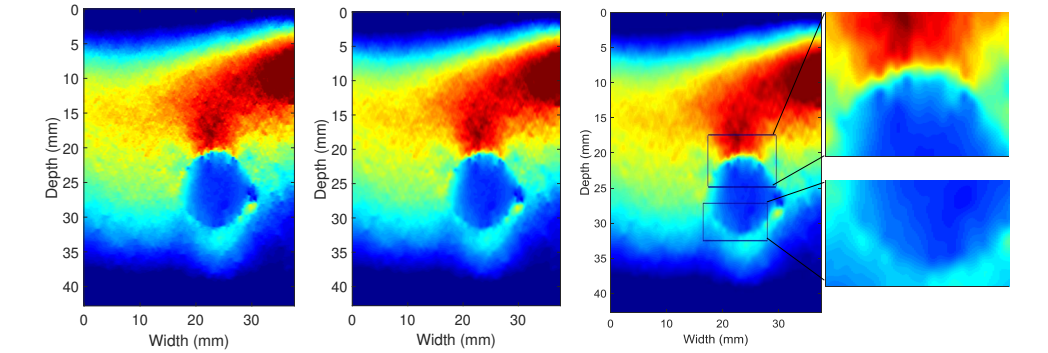


(a) GLUE, $\rho = 3$ (b) GLUE, $\rho = 35$ (c) GLUE, $\rho = 65$

(d) CGLUE, $\rho = 3$ (e) CGLUE, $\rho = 35$ (f) CGLUE, $\rho = 65$

Figure 4.6: Strain images of the tissue mimicking phantom calculated using GLUE and CGLUE.

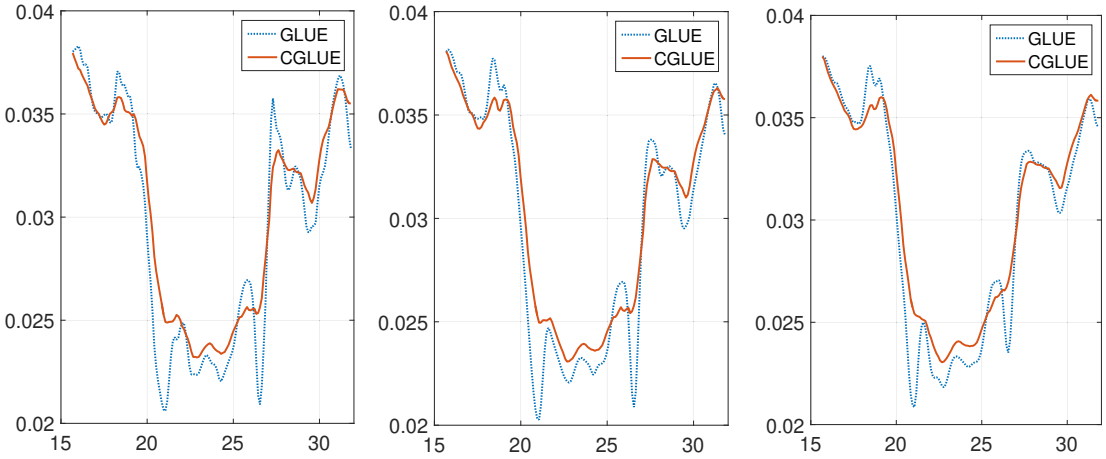


(a) $\rho = 3$ (b) $\rho = 35$ (c) $\rho = 65$

Figure 4.7: Strain profiles of the tissue mimicking phantom across the horizontal yellow line in Fig. 4.6(a) calculated by GLUE and CGLUE.

Table 4.3: CNR for strain images of the phantom data for different methods. Windows that are considered for calculating CNR are shown in red and blue lines in Fig. 4.6.

| $\rho$ | | CNR (dB) |
|---|---|---|
| 3 | GLUE | 4.54 (6.58) |
| | CGLUE | 5.39 (7.32) |
| 35 | GLUE | 4.69 (6.72) |
| | CGLUE | 5.44 (7.36) |
| 65 | GLUE | 4.81 (6.83) |
| | CGLUE | 5.50 (7.41) |

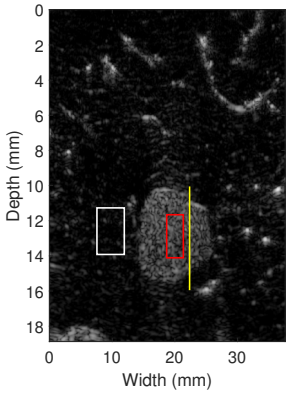


(a) B-mode

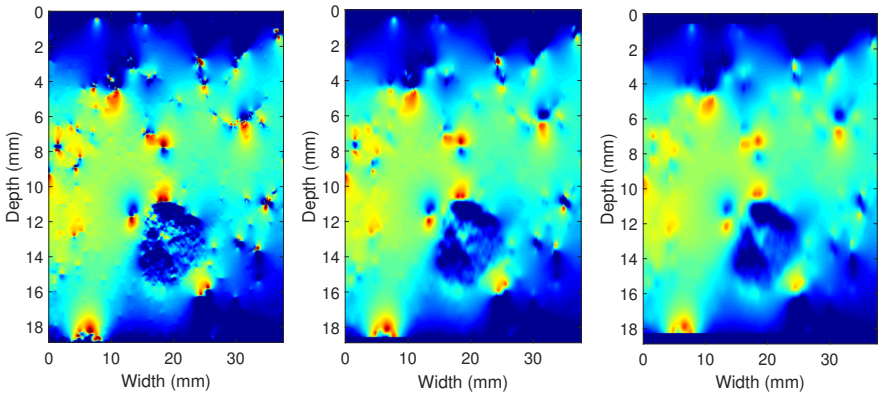


(b) GLUE, $\rho = 3$ (c) GLUE, $\rho = 35$ (d) GLUE, $\rho = 65$

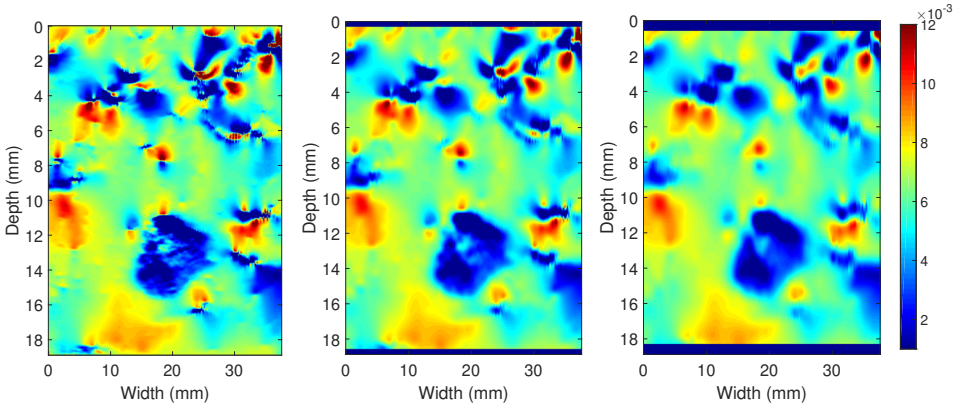


(e) CGLUE, $\rho = 3$ (f) CGLUE, $\rho = 35$ (g) CGLUE, $\rho = 65$

Figure 4.8: B-mode image of the lamb liver with small piece of olive placed in (a). Estimated strain images using GLUE and CGLUE for different LSQ window sizes are shown in (b)-(g).

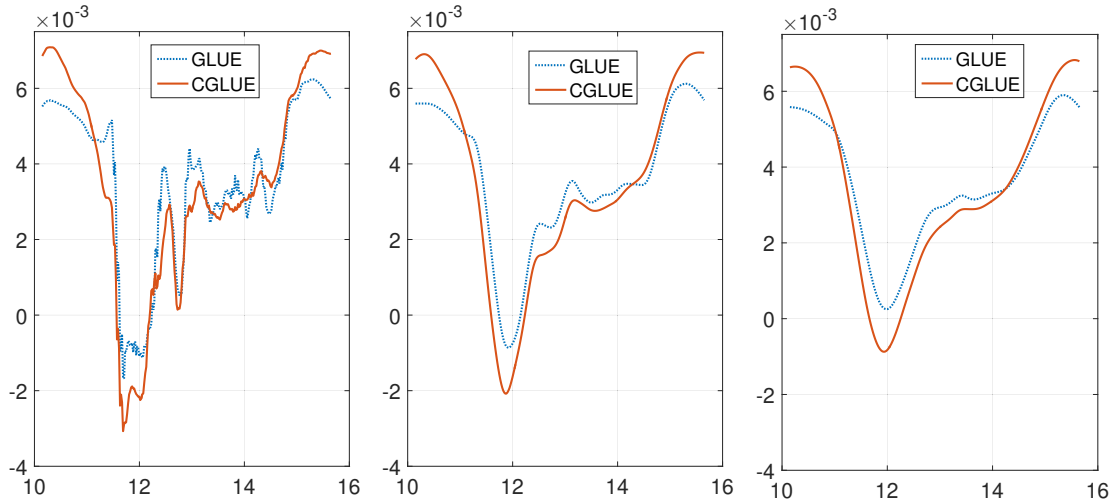


(a) $\rho = 3$ (b) $\rho = 35$ (c) $\rho = 65$

Figure 4.9: Strain profiles of the liver data across the vertical yellow line in Fig. 4.8(a) calculated by GLUE and CGLUE. Windows of length 3, 35 and 65 are used for estimating strain by LSQ in (a), (b) and (c), respectively.

of CGLUE with $\rho = 3$ is smoother than the strain of GLUE. Meanwhile, strain of CGLUE with $\rho = 35, 65$ are smoother than GLUE.

For quantitative comparison of CGLUE and GLUE, the calculated CNRs are reported in Table 4.4. The improvement of CGLUE with respect to GLUE in this experiment is much more than simulation and phantom experiments due to high level of noise that is present in *ex-vivo* data.

Table 4.4: CNR for strain images of the *ex-vivo* data for different methods. Windows that are considered for calculating CNR are shown in white and black lines in Fig. 4.8.

| $\rho$ | | CNR (dB) |
|---|---|---|
| 3 | GLUE | 10.20 (10.09) |
| | CGLUE | 31.76 (15.02) |
| 35 | GLUE | 20.09 (13.03) |
| | CGLUE | 49.88 (16.98) |
| 65 | GLUE | 28.84 (14.60) |
| | CGLUE | 63.24 (18.01) |

## 4.3 Conclusions

In this paper we proposed a novel method for USE and named it as CGLUE. We utilized time-gain and time-delay corrected channel data instead of RF data for USE. We proved that the proposed method decreases the bias and variance of error for estimated displacement as compared to the recently proposed method GLUE. The results of simulation, phantom and *ex-vivo* experiments were presented to illustrate better performance of CGLUE over GLUE. The estimated strain of CGLUE was smoother than the result of GLUE even for small LSQ window sizes. The smoothness of the estimated strains for small data sizes of LSQ further corroborates more accurate estimated displacement by CGLUE over GLUE.

# Chapter 5

# Virtual Source Synthetic Aperture for Accurate Lateral Displacement Estimation

**This chapter is based on our published paper [91].**

---

Different methods are proposed to perform TDE that can be broadly categorized as window-based, regularized optimization-based, and deep-learning approaches [38, 92]. Despite the capability of USE methods in estimating both axial and lateral displacements, the latter is of lower quality compared to the former for three main reasons: low sampling rate, lack of carrier signal and low resolution in the lateral direction [93, 94]. One of the most utilized techniques for increasing the data size in lateral direction is interpolation [95, 96]. It is shown by experimental results that spline interpolation has the best performance among different techniques of interpolation [93]. In these methods, the bandwidth should be large enough to have sufficient overlap between adjacent lines [95]. It is shown that the minimum density of A-lines for original data should be at least 2 A-line per beam width to have an acceptable interpolation [95]. Accordingly, not only interpolation does not change the resolution, it cannot be implemented for high resolution data to increase the number of samples. Besides low resolution, another disadvantage of interpolation especially for large factor interpolations is decreasing the robustness of the TDE, since interpolation can be a source of error [97].

SA imaging is used for lateral strain estimation in [98]. SA has narrow and fixed beam width in all field of view in contrast to line by line imaging, which has narrow beam width in the focal zone only. Moreover, SA has capability of increasing sampling rate in lateral direction without interpolation, which also improves the resolution. It is shown that the accuracy of TDE increases by decreasing the beam width [98]. Accordingly, SA is better than line by line imaging for lateral USE, with the disadvantage of lower transmission power and penetration depth, which could hinder clinical use

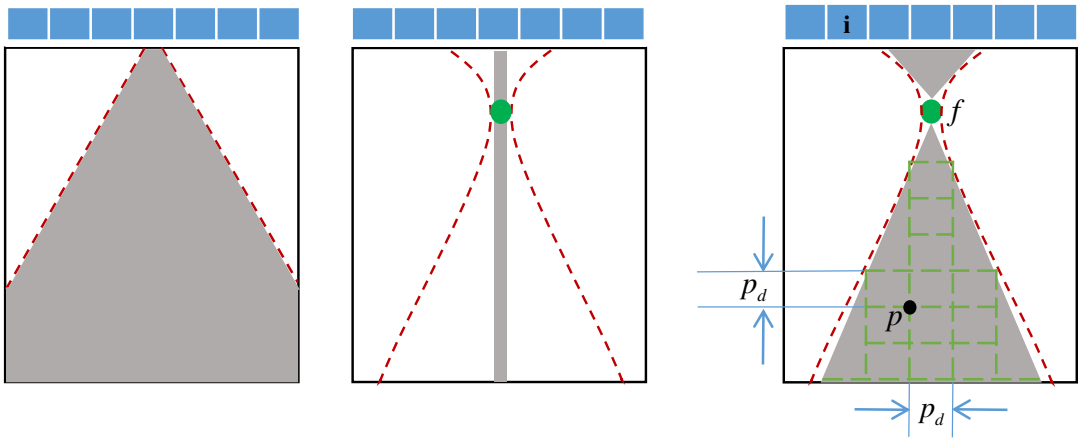


(a) SA (b) Line by line (c) VSSA

Figure 5.1: Schematics of different imaging modes. The red dashed lines show the beam pattern, while the gray areas show the regions that received data should be focused.

of SA [99, 100].

In this chapter, we propose to use VSSA imaging that implements SA-based beamforming on focused transmitted signals. On the one hand, this enables us to benefit from advantages of SA such as high resolution and the capability to increase the sampling frequency to increase the resolution and number of A-lines. On the other hand, we can take advantage of line by line imaging in high penetration depth. Then the beamformed data is fed to our recently published TDE method, OVERWIND [74] that has shown to outperform window-based and other regularized optimization-based techniques. We call the results of OVERWIND on VSSA with high sampling frequency in lateral direction as High Frequency OVERWIND (HF OVERWIND) and compare the results with OVERWIND on spline based interpolated data (Inter. OVERWIND) and also with OVERWIND on VSSA with low sampling frequency in lateral direction in which the number of A-lines is equal to the number of piezo-electrics (LF OVERWIND).

## 5.1 Methods

Most USE techniques like OVERWIND requires two sets of data collected as the tissue undergoes some deformation. Let $I_1$ and $I_2$ of size $(m, n)$ be the beamformed RF data where $m$ and $n$ are depth and width of the imaged tissue. The goal of TDE is estimating the displacement field between these two data sets. In this section, we first briefly review our recently developed USE method, OVERWIND [74], and then present the beamforming technique to increase the number of lines and resolution in the lateral direction to help OVERWIND in accurately estimating displacements.

### 5.1.1 OVERWIND: tOtal Variation Regularization and WINDowbased time delay estimation

The displacement estimation in OVERWIND comprises two steps for increasing the capabilities of the technique in estimating large deformations. In the first step, an integer estimation of the displacement is calculated using DP, which is a recursive optimization based method for image registration. In this method, we consider a range of displacements for each sample and optimize the cost function that incorporates similarity of RF samples and displacement continuity to estimate integer displacement of RF samples [78]. In the second step, the sub-sample displacements are calculated by minimizing the following cost function:

$$
\begin{aligned}
&C(\Delta a_{1,1}, \ldots, \Delta l_{m,n}) = \Sigma_{j=1}^{n} \Sigma_{i=1}^{m} \Big[ \tfrac{1}{L} \Sigma_{k,r} \Big( I_1(i+k, j+r) \\
&- I_2(.) - \Delta a_{i,j} I'_{2a}(.) - \Delta l_{i,j} I'_{2l}(.) \Big)^2 \\
&+ \alpha_1 \delta_1 (a_{i,j} + \Delta a_{i,j} - a_{i-1,j} - \Delta a_{i-1,j} - \varepsilon_a) \\
&+ \alpha_2 \delta_2 (a_{i,j} + \Delta a_{i,j} - a_{i,j-1} - \Delta a_{i,j-1}) \\
&+ \beta_1 \delta_3 (l_{i,j} + \Delta l_{i,j} - l_{i-1,j} - \Delta l_{i-1,j}) \\
&+ \beta_2 \delta_4 (l_{i,j} + \Delta l_{i,j} - l_{i,j-1} - \Delta l_{i,j-1} - \varepsilon_l) \Big],
\end{aligned}
$$

where $i$ and $j$ are indices of RF samples in the region of interest and the symbols $i+k$ and $j+r$ represent indices of RF samples inside the window that is considered around each sample. $\{a_{i,j},\ \Delta a_{i,j}\}$ and $\{l_{i,j}, \Delta l_{i,j}\}$ represent the integer and sub-sample displacement of $(i,j)$ in axial and lateral directions, respectively. $I_2(.)$ represent $I_2(i+k+a_{i,j}, j+r+l_{i,j})$ and $I'_{2a}(.)$ and $I'_{2l}(.)$ are derivatives of $I_2$ in axial and lateral directions, respectively. $\delta_x(s) = 2\lambda_x \sqrt{\lambda_x^2 + s^2}$ is an approximate of norm L1 for regularization which allows sharp transitions where $\lambda_x$ is a scaling parameter. Finally, $\alpha_1, \alpha_2, \beta_1$ and $\beta_2$ are regularization parameters to be tuned. These four parameters can be related to each other as explained in Discussion Section.

OVERWIND considers both displacements in axial and lateral directions, but the estimation in the former direction is more accurate since, among other reasons, ultrasound data usually has less samples in lateral direction compared to axial direction. One of the most common techniques to cope with this issue is interpolating data in lateral direction. Not only it does not change the resolution but also its performance can deteriorate for the high resolution data sets since the A-lines do not have high overlap with each other in the high resolution data [101, 102]. Another disadvantage of interpolation is low robustness for complex interpolation techniques.

In this paper, we propose to use VSSA imaging mode for USE, which has the ability of increasing sampling frequency in the lateral direction as much as axial direction and also has high resolution in lateral direction while allowing high penetration. In the next subsection we describe SA, line by line imaging, and then show how VSSA can benefit to relax two main limitations for lateral displacement estimation in USE.

### 5.1.2 SA: Synthetic Aperture

In SA, a single element transmits a wave through the tissue as shown in Fig. 5.1(a) and all elements record reflections. Each element generates an image of tissue (the gray area of Fig. 5.1(a)) by focusing the received beam at any point according to the expression

$$t_p(ij) = \frac{\sqrt{(x_p - x_i)^2 + (z_p)^2} + \sqrt{(x_p - x_j)^2 + (z_p)^2}}{c} \tag{5.1}$$

where $c$ is the speed of sound in soft tissue and $i$ and $j$ are the transmitter and receiver elements symbols. $x_i$, $x_j$ and $x_p$ are the horizontal positions of the transmitter $i$, receiver $j$ and point $p$ where the beam is focused and $z_p$ is depth of point $p$ by assuming the probe is at zero depth. During each transmission, all receivers in the aperture focus the received beam at all points of the aperture and summation of these data for all receivers generate a low-resolution image. The next element of the array transmits and the previously described operation is repeated to generate another low-resolution image. By repeating the experiment for all piezo-electrics as transmitter and adding up all low-resolution images, the final image is generated as per the following expression

$$y_p = \sum_{i=1}^{e} \sum_{j=1}^{e} t_p(ij), \tag{5.2}$$

where $e$ is the total number of elements in the transducer array. The main disadvantage of this technique for USE is the limitation in imaging deep areas since the emitted signal from one piezo-electric does not have enough power to penetrate deep areas.

### 5.1.3 Line-by-Line Imaging

In this imaging technique, a group of elements (i.e. transmission aperture) transmits the beam to increase the penetration of signal to image deeper areas. The transmitted beam focuses at a single point during each transmission. The data received at different channels is processed to generate one line of the US image. Fig. 5.1-(b) shows the pattern of transmission by dashed red lines, while the area that is imaged in each transmission is highlighted by gray. In this technique, the lateral resolution at the focal depth is high and close to the resolution of the SA imaging. Further away from this point, the resolution decreases. Moreover, the number of lines is limited to the number of elements (without interpolation).

### 5.1.4 VSSA: Virtual Source Synthetic Aperture

This imaging technique benefits from both SA and line by line imaging and has the ability of increasing sampling frequency and resolution in lateral direction in all imaged area while penetrating to deep fields which are essential for USE. Similar to line by line imaging, a group of elements transmits the beam by focusing at a single

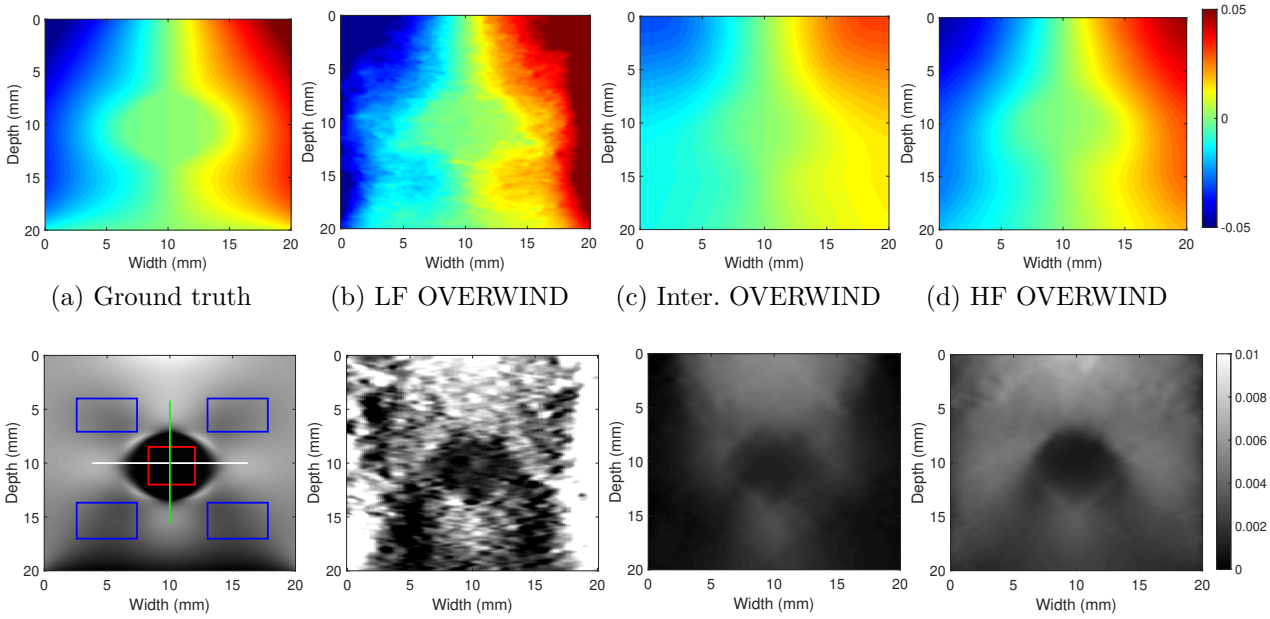


(a) Ground truth (b) LF OVERWIND (c) Inter. OVERWIND (d) HF OVERWIND

(f) Ground truth (g) LF OVERWIND (h) Inter. OVERWIND (i) HF OVERWIND

Figure 5.2: Estimated lateral displacement with LF OVERWIND, Inter. OVERWIND and HF OVERWIND for simulation data are shown in (b)-(d), respectively. The second row shows the corresponding strains.

point [103, 104]. Since the beam at the focal point is very narrow, we can assume the focal point as a virtual source that transmits the beam similar to SA as shown in Fig. 5.1-(c). Then each receiver focuses the received data at any point inside the aperture according to the following expression [105]

$$t_p(fj) = \frac{z_f \pm \sqrt{(x_p - x_f)^2 + (z_f - z_p)^2} + \sqrt{(x_j - x_p)^2 + z_p^2}}{c} \tag{5.3}$$

where $c$ is the speed of sound in soft tissue, $x_p$, $x_f$, $z_p$ and $z_f$ are the positions of the focal point $f$ and $p$ is the location at which the beam is focused. The $\pm$ term in Eq. 5.3 divides the imaging area into regions above and below the virtual source. Similar to SA, summation of focused data by different receivers generates a low-resolution image and by switching the transmissions new focal points will be the virtual sources and in each step a new low resolution image will be generated. Similar to SA, adding up these images will end up with a high-resolution image as

$$y_p = \sum_{f=1}^{e} \sum_{j=1}^{e} t_p(fj) \tag{5.4}$$

Similar to line by line imaging, the number of A-lines is usually equal to number of elements in VSSA, and interpolation is the most commonly used technique for

increasing the sampling frequency in the lateral direction for USE purposes. However, for the VSSA the received data can be focused at any point inside the aperture (highlighted by gray in Fig. 5.1-(c)). To increase the sampling frequency, we consider a grid consisting of nodes with same spatial distance of nodes in axial and lateral direction as $p_d = \frac{c}{2f_s}$. Each receiver element generates an image on that grid as shown in Fig. 5.1-(c). Therefore, we can increase number of data and resolution in lateral direction without interpolation.

### 5.1.5 Data Acquisition and Comparison Metrics

In this section, the data that are utilized in different experiments of the paper are described and then results of HF OVERWIND are compared with Inter. OVERWIND and also LF OVERWIND wherein number of data in lateral direction is equal to number of piezo-electrics. In the Results Section, the CNR metric is used to provide a quantitative value for assessing the proposed method [90]

$$\mathrm{CNR} = 20\ \log_{10}\Big(\frac{2(\bar{s}_b - \bar{s}_t)^2}{\sigma_b^2 + \sigma_t^2}\Big), \tag{5.5}$$

where $\bar{s}_t$ and $\bar{s}_b$ are the spatial strain averages of the target and background, $\sigma_t^2$ and $\sigma_b^2$ are the spatial strain variances of the target and background, respectively [7]. For the simulation results where we know the ground truth, we use Root Mean Square Error (RMSE), Mean of estimation Error (ME) and Variance of estimation Error (VE) as other metrics according to

$$\begin{aligned}
\mathrm{RMSE}\% &= 100 * \frac{\sqrt{m \times n \times \sum_{i=1}^{m}\sum_{j=1}^{n}\left(S_e(i,j) - S_g(i,j)\right)^2}}{\sum_{i=1}^{m}\sum_{j=1}^{n} S_g(i,j)}, \\
\mathrm{ME} &= \frac{\sum_{i=1}^{m}\sum_{j=1}^{n} S_e(i,j) - S_g(i,j)}{m \times n} \\
\mathrm{VE} &= \frac{\sum_{i=1}^{m}\sum_{j=1}^{n}\left(S_e(i,j) - S_g(i,j)\right)^2}{m \times n} - ME^2
\end{aligned} \tag{5.6}$$

where $m$ and $n$ are size of estimated strains. $S_e$ and $S_g$ are estimated and ground truth strains, respectively. For estimating the axial strain, the displacement field should be differentiated. To reduce the impact of noise during differentiating, it is common to use LSQ for strain estimating. For estimating the strain at each sample, a few neighboring samples in a window of size $\rho$ are considered and a line is fitted to their displacements. The tangent of the line is considered as the strain for the middle sample. Considering more data points for least square makes the strain smooth at the cost of losing resolution. Throughout the paper, the size of LSQ window is 5% of total data size.

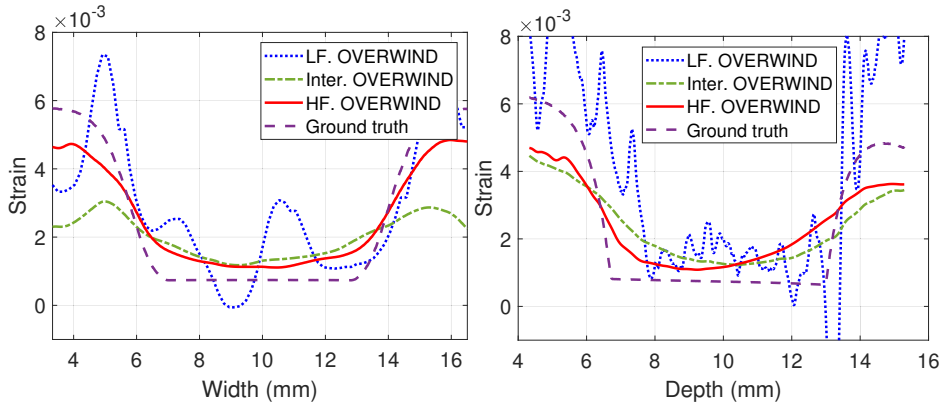


(a) horizontal (b) vertical

Figure 5.3: Edge spread function of the lateral strain in horizontal (a) and vertical line (b).

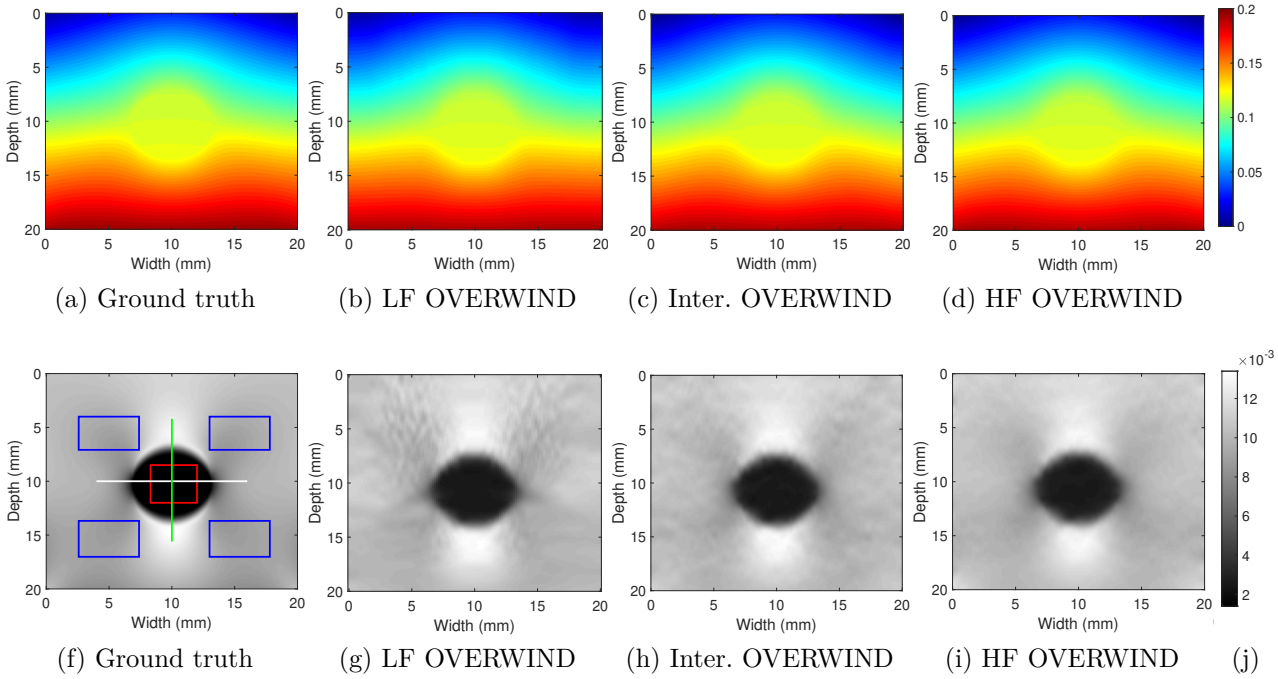


(a) Ground truth (b) LF OVERWIND (c) Inter. OVERWIND (d) HF OVERWIND

(f) Ground truth (g) LF OVERWIND (h) Inter. OVERWIND (i) HF OVERWIND (j)

Figure 5.4: Estimated axial displacement with LF OVERWIND, Inter. OVERWIND and HF OVERWIND for simulation data are shown in (b)-(d), respectively. The second row shows the corresponding strains.

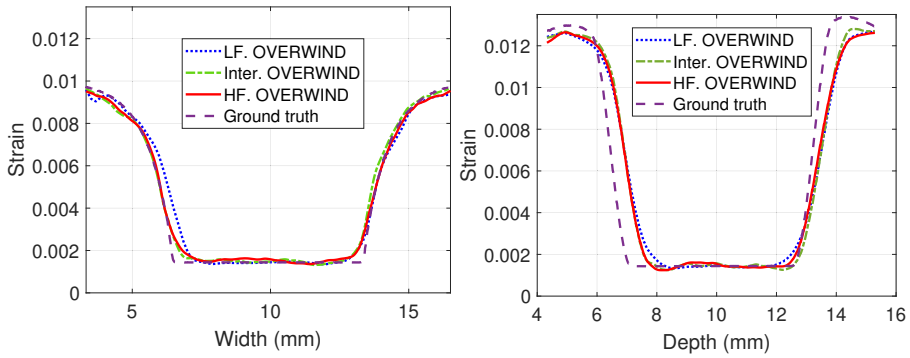


(a) horizontal (b) vertical

Figure 5.5: Edge spread function of the axial strain in horizontal (a) and vertical line (b).

### Simulation Data

A simulated phantom is generated by utilizing the Field II ultrasound simulation software [73] by randomly distributing slightly more than 10 scatterers per resolution cell to satisfy the Rayleigh scattering regime.

The simulated phantom consists of a homogeneous region with a Young's modulus of 4 $kPa$ and one cylindrical inclusion with a Young's modulus of 40 $kPa$. For compressing the phantom and computing its ground truth displacement, Finite Element Method (FEM)-based deformations are computed using the ABAQUS software package (Johnston, RI, USA) with triangular mesh sizes of 0.05 $mm^2$. The probe consists of 128 elements with pitch of 0.15 mm. The center frequency is 7 MHz, while the sampling rate is 100 MHz. The lateral sampling frequency in HF OVERWIND is 19 times higher than LF OVERWIND. Therefore, the data is interpolated by a factor of 19 and using a cubic spline method for Inter. OVERWIND, so that Inter. OVERWIND and HF OVERWIND have the same number of samples.

### Phantom Data

The phantom data is acquired from a tissue mimicking breast phantom (059 tissue mimicking breast phantom, CIRS tissue simulation & phantom technology, Norfolk, VA, USA) using an E-Cube R12 ultrasound machine (Alpinion, Bothell, WA, USA) with a L3-12H probe at the center frequency of 8 MHz and sampling frequency of 40 MHz. The lateral sampling frequency in HF OVERWIND is 8 times higher than LF OVERWIND, therefore, the data is interpolated by a factor of 8 using the cubic spline method for Inter. OVERWIND.

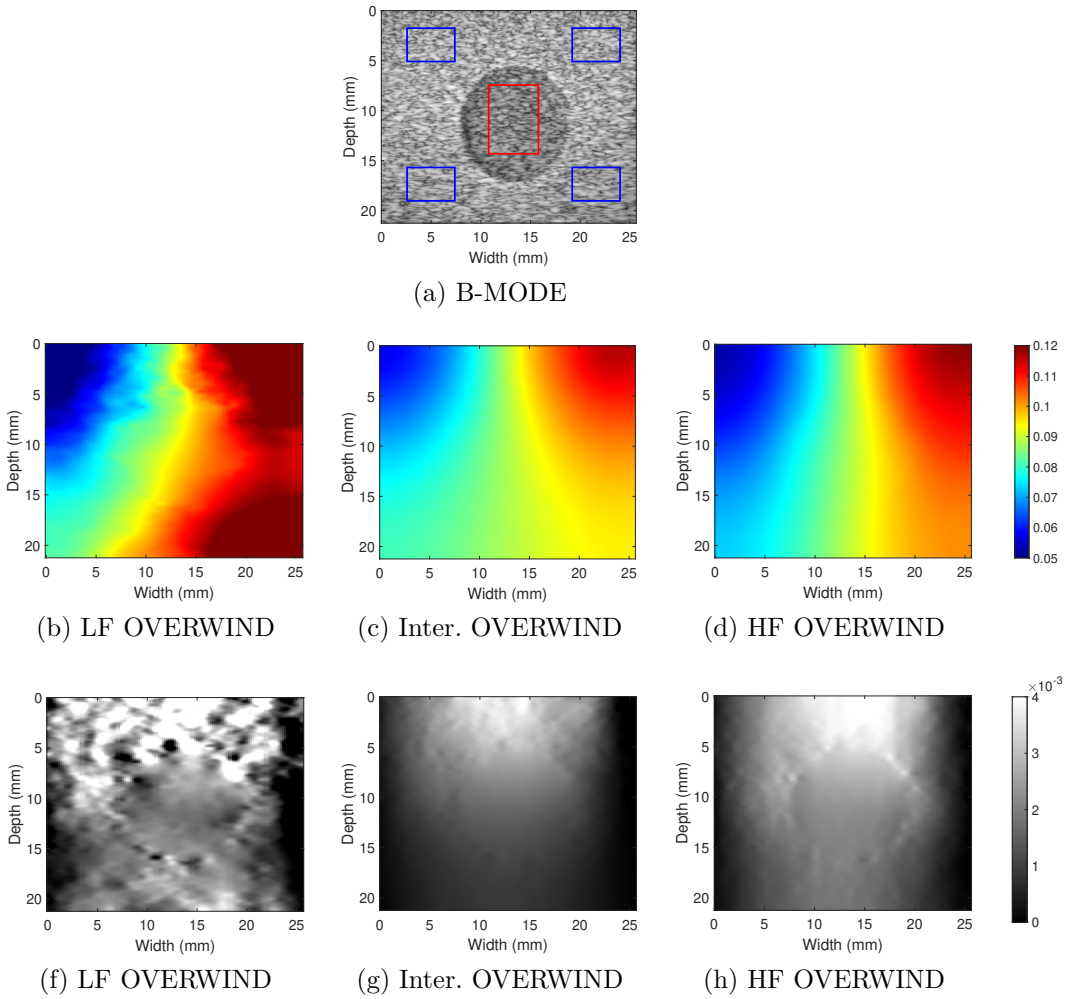


(a) B-MODE

(b) LF OVERWIND (c) Inter. OVERWIND (d) HF OVERWIND

(f) LF OVERWIND (g) Inter. OVERWIND (h) HF OVERWIND

Figure 5.6: Results on a tissue mimicking phantom. B-Mode image is shown in (a). Estimated lateral displacement with LF OVERWIND, Inter. OVERWIND and HF OVERWIND are shown in (b)-(d), respectively. The second row shows the corresponding strains.

Table 5.1: Quantitative comparison of lateral strain estimation on simulated phantom.

| | LF OVERWIND | Inter. OVERWIND | HF OVERWIND |
|---|---|---|---|
| ME | $-1.1 \times 10^{-3}$ | $1.6 \times 10^{-3}$ | $4.33 \times 10^{-4}$ |
| VE | $9.77 \times 10^{-6}$ | $2.18 \times 10^{-6}$ | $6.21 \times 10^{-7}$ |
| RMSE | 85.04% | 56.73% | 23.09% |
| CNR | 0.37 | -1.49 | 21.70 |

Table 5.2: Quantitative comparison of axial strain estimation on simulated phantom.

| | LF OVERWIND | Inter. OVERWIND | HF OVERWIND |
|---|---|---|---|
| ME | $-3.13 \times 10^{-5}$ | $-3.93 \times 10^{-5}$ | $-4.38 \times 10^{-5}$ |
| VE | $5.21 \times 10^{-7}$ | $4.97 \times 10^{-7}$ | $4.96 \times 10^{-7}$ |
| RMSE | 7.99% | 7.82% | 7.81% |
| CNR | 50.76 | 52.56 | 54.09 |

## 5.2 Results

**Simulation Results**

Fig. 5.2 shows the lateral displacement and strain for LF OVERWIND, Inter. OVERWIND and HF OVERWIND. It is clear that USE on data sampled at a higher rate significantly improves the estimations. As anticipated, the interpolation decreases the variance of estimation significantly at the expense of over smoothing compared to low sampled data. The reported RMSE, ME and VE and CNR in table 6.1 also corroborate improvements in lateral estimations. To provide a better comparison, we illustrate the Edge Spread Function (ESF) of the estimated strains across two vertical and horizontal lines shown in Fig. 5.2 (a). As illustrated in Fig. 5.3, the ESF of the HF OVERWIND is substantially closer to the ground truth as compared to those of Inter. OVERWIND and LF OVERWIND.

Fig. 5.4 also shows the axial displacement and axial strain for laterally low sampled data, interpolated data and laterally high sampled data. It is inevitable that correct lateral estimation leads to slightly improved axial estimations. Table 5.2 and Fig. 5.5 show marginal improvement of axial strain.

**Phantom Results**

Estimated lateral displacement and strain for experimental phantom are shown in Fig. 5.6. Similar to the simulation study, the lateral estimation by spline interpolation is over smoothed and HF OVERWIND outperforms the previous methods. Fig. 5.7 shows the axial displacements and strains and it illustrates better performance of HF

Table 5.3: The CNR comparison of different method on the phantom experiment in axial and lateral estimations.

| | CNR | |
|---|---|---|
| | Axial | Lateral |
| LF OVERWIND | 10.80 | -29.89 |
| inter OVERWIND | 10.28 | -1.55 |
| HF OVERWIND | 11.01 | 6.35 |

OVERWIND over both LF OVERWIND and Inter. OVERWIND. The reported CNR values in Table 5.3 also show improvement in both lateral and axial estimations by HF OVERWIND.

## 5.3 Conclusions

Accurate estimation of the tissue mechanical parameters requires accurate strain estimation in all direction. Although USE techniques estimate displacements in both axial and lateral directions, estimation in the axial direction is more accurate than in the lateral direction due to high sampling frequency, improved axial resolution and a carrier signal propagating in the axial direction. In this paper we proposed to use VSSA imaging mode to benefit from advantages of both SA and line by line imaging in a high resolution with high number of A-lines and penetration depth. The beamformed data is fed to our recently developed TDE method, OVERWIND. The results exhibit significant improvement compared to interpolating data in lateral direction as one of the commonly used techniques in estimating lateral strain.

In this paper we proposed to use VSSA as an advanced beamforming technique for time delay estimation in OVERWIND. In this imaging technique multiple piezoelectrics participate in the transmission which improves the beam strength in deep regions. The focused region of the beam can be considered as a virtual element that transmits a beam in tissue. As such, the imaging procedure becomes closer to the operation of the synthetic aperture and received data can be beamformed similar to synthetic aperture. In this imaging mode, the sampling frequency in the lateral direction can be increased as much as the sampling frequency in the axial direction to increase the resolution and addresses two of the major limitations in estimation lateral displacements. Meanwhile, VSSA has fixed and narrow beam width in all imaging field which results in accurate and high-resolution displacement estimation.

Virtual source synthetic aperture assumes the focal point as a beam source that transmits the signal and conducts beamforming according to Eq. (5.3). The $\pm$ term in Eq. (5.3) divides the imaging area into top and bottom regions above and below the virtual source resulting in a discontinuity at the focal depth as shown in Fig. 5.8. This discontinuity is a source of error for USE. Therefore, the focal point should be established in an area outside the region of interest and corresponding data should

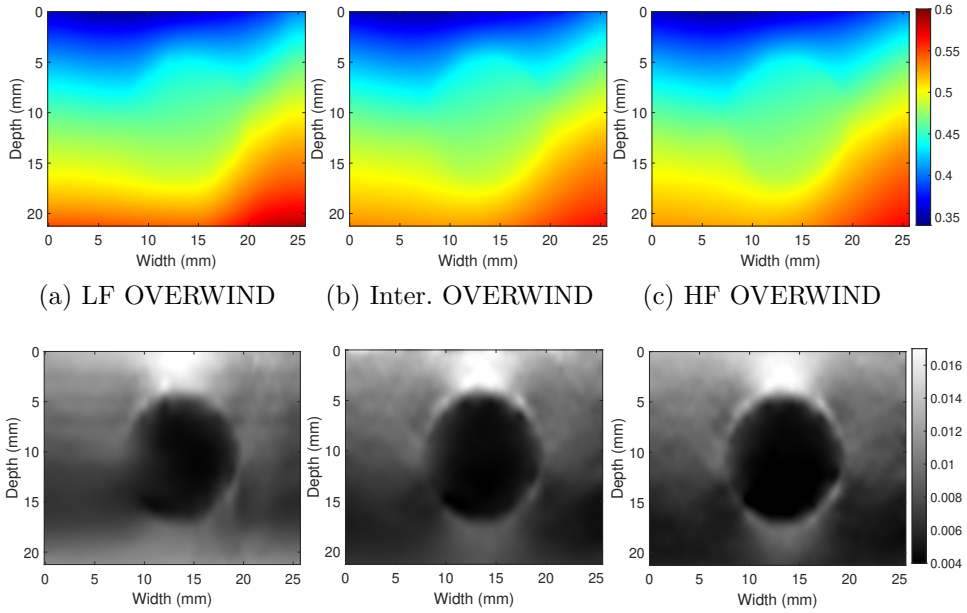


(a) LF OVERWIND (b) Inter. OVERWIND (c) HF OVERWIND

(e) LF OVERWIND (f) Inter. OVERWIND (g) HF OVERWIND

Figure 5.7: Results on a tissue mimicking phantom. Estimated axial displacement with LF OVERWIND, Inter. OVERWIND and HF OVERWIND are shown in (a)-(c), respectively. The second row shows the corresponding strains.

be cropped before USE to avoid this discontinuity.

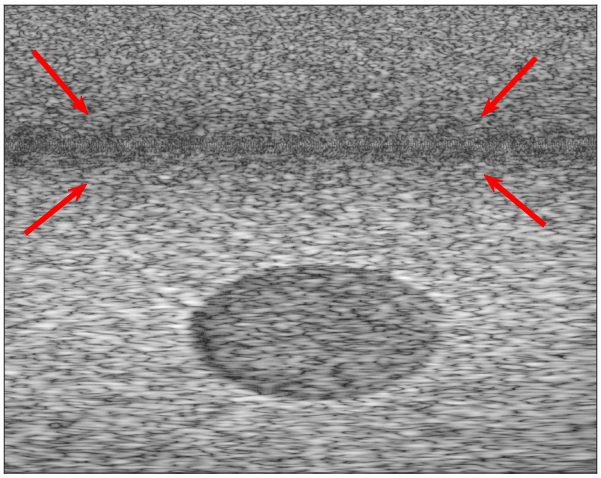

(a)

Figure 5.8: Discontinuity of the VSSA imaging in the focal depth

# Chapter 6

# 2D Displacement Estimation for Qausi-Static Ultrasound Elastography with mechanical constraints.

**The proposed method of this chapter is submitted to IEEE Transaction on Medical Imaging.**

---

Different methods are proposed for 2D displacement estimation including window-based, regularized optimization-based and deep learning approaches. All methods have the capability of estimating displacement in two directions. However, estimation in the axial direction is much more precise and accurate compared to that of lateral direction due to three main reasons [93, 94]: lower sampling frequency, wider point spread function and a lack of carrier signal (i.e. ultrasound beam is an longitudinal beam propagating in axial direction).

Several supplementary techniques are proposed to increase the accuracy of 2D estimation methods in estimating lateral displacement. Interpolating data in lateral direction is one of the most commonly used techniques [95, 96]. It is shown that spline-based interpolation has the best performance compared to other interpolating methods, but the bandwidth of RF signal should be large enough to have sufficient overlap between adjacent Radio Frequency (RF) lines. In a recent work, we proposed beamforming with VSSA for better displacement estimation. The main advantage of VSSA is its capability in increasing sampling rate without interpolation [91]. The other approach for increasing accuracy of estimation is beam steering [106, 107]. In these methods, multiple RF data should be acquired in different angels which requires hardware modification (for rotating the probe with exact angles) or software modification (for steering the transmitted beam). The displacement at each angle should be estimated individually and results should be mapped to extract correct estimation

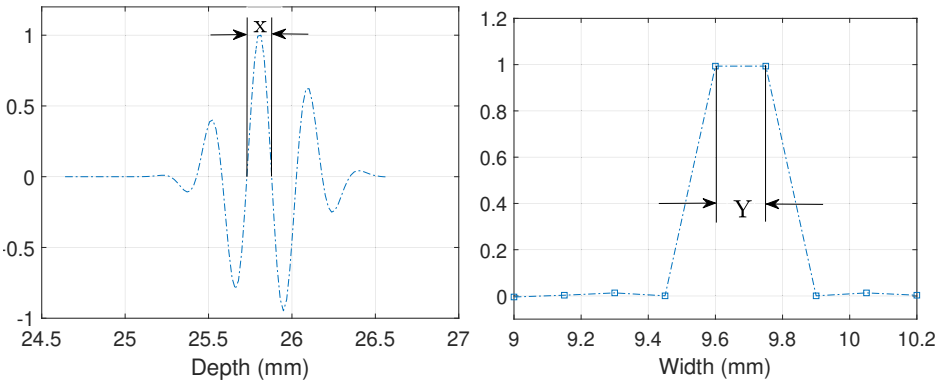


Figure 6.1: Intensity variation of a PSF in axial and lateral directions.

in lateral direction. Finally, the third commonly used techniques are post processing techniques that reconstruct lateral displacement from the initial estimations in both axial and lateral directions and considering some mechanical based constraints like incompressibility or satisfying momentum equation [27, 108, 109]. The reconstructed lateral displacements by these methods are highly affected by initially estimated poor lateral estimations and also solely rely on axial displacements instead of also exploiting the RF data.

In this chapter, we propose a MUSCULAR as a 2D displacement estimation method for more precise and accurate lateral displacement estimation without implementing any of the above mentioned supplementary techniques. In MUSCULAR, we add the mechanical constraints as a regularization part to the cost function as well as absolute intensity differences and displacement continuity of neighboring samples. Regarding the mechanical constraint, it is well known that by assuming tissue to be incompressible, linear plane stress and linear plane strain assumptions could be valid approximations for describing the behavior of the tissue. The force magnitude in the out-of-plane direction determines the choice of plane stress or plane strain [109]. In this paper we focus on plane stress as a thin layer of the tissue in out of plane direction is compressed. MUSCULAR is a displacement estimation method that estimates high accuracy deformation without exploiting supplementary steps and it significantly reduces the computational complexity.

We compare MUSCULAR with the two other 2D displacement estimation methods. The first method is the recently published regularized optimization based USE method OVERWIND [74] and the second one is the commonly used window-based technique that estimates deformation by maximizing NCC. We show that MUSCULAR significantly outperforms OVERWIND and NCC in terms of lateral displacement estimation. We use one set of simulation data, two sets of phantom and two sets of *in-vivo* in our experiments. MUSCULAR is a displacement estimation method and all supplementary techniques for improving lateral estimation can be implemented for MUSCULAR as well as other displacement estimation method. However we show

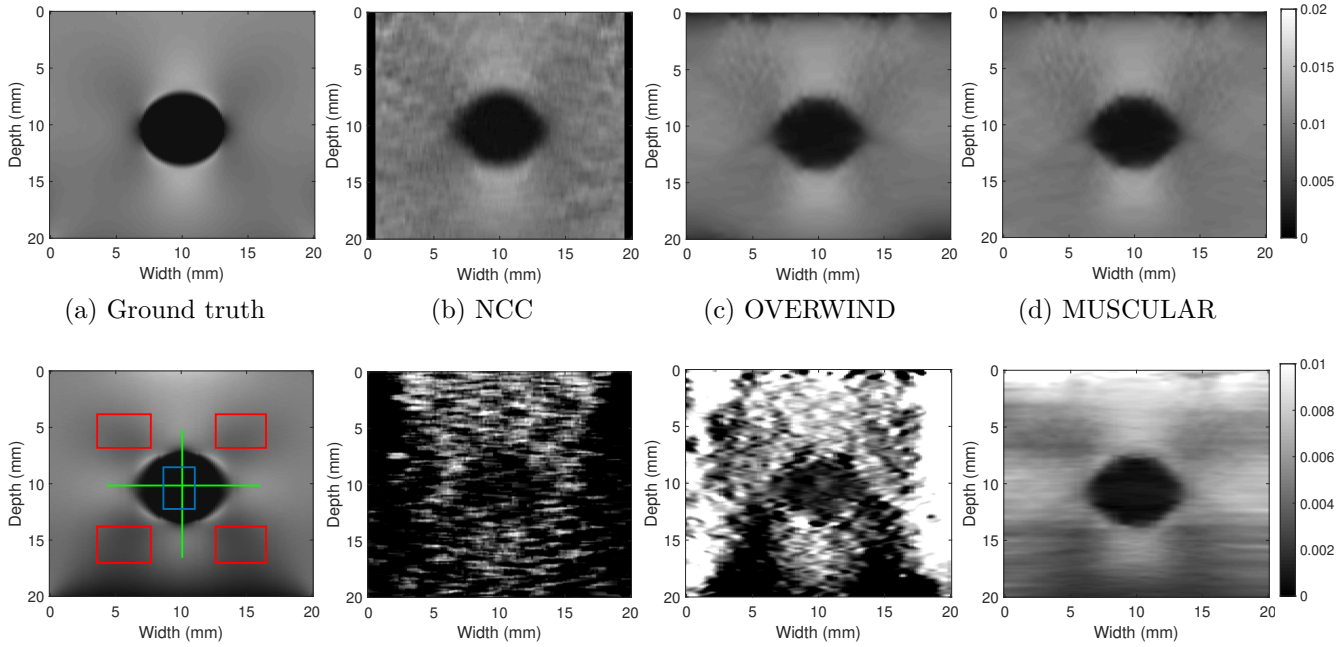


(a) Ground truth (b) NCC (c) OVERWIND (d) MUSCULAR

(f) Ground truth (g) NCC (h) OVERWIND (i) MUSCULAR

Figure 6.2: Ground truth axial and lateral strains are shown in (a) and (f), respectively. Estimated axial strains with NCC, OVERWIND and MUSCULAR for simulation data are shown in (b)-(d), respectively. The estimated lateral strains are shown in (g)-(i).

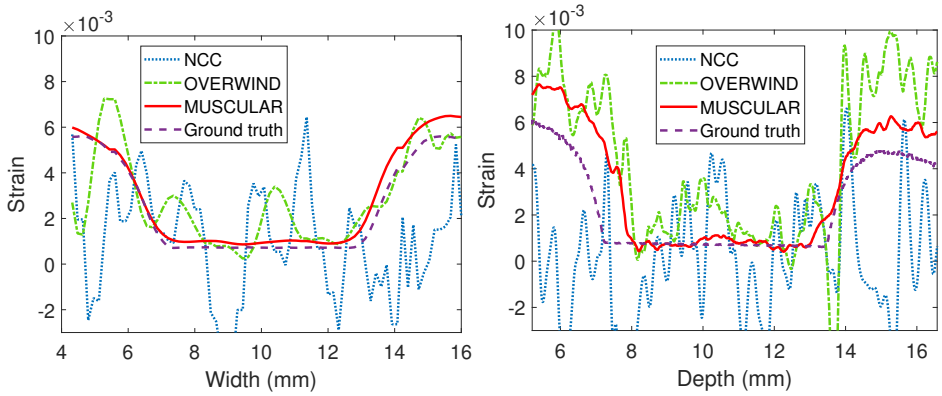


(a) horizontal (b) vertical

Figure 6.3: Edge spread function of the estimated lateral strain for simulated data across vertical and horizontal lines that are shown in Fig. 6.2-(f).

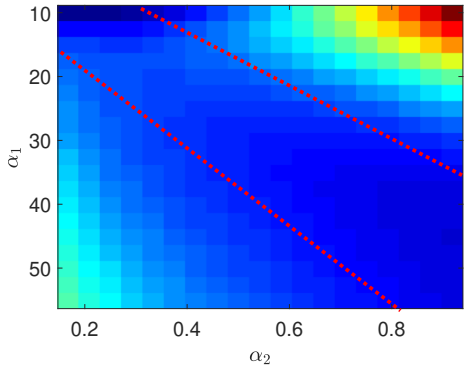


Figure 6.4: Normalized RMSE of simulation results for different combination of $\alpha_1$ and $\alpha_2$. The slope of the main diagonal is 60.

that pure estimation of MUSCULAR (without any supplementary techniques) outperforms the other estimation methods combined with supplementary techniques.

## 6.1 Methods

Let $I_1$ and $I_2$ denote two RF data collected before and after some deformation. The only assumption that USE techniques make to increase the accuracy and robustness of the displacement estimation is the continuity assumption, wherein the neighboring samples -spatially or temporally- are assumed to have similar displacements. In our recent work for USE, we proposed a cost function and added the continuity assumption as norm L1 regularization of the difference between displacements of neighboring samples in both axial and lateral directions. For quasi-static USE, the plane stress assumption is also a valid one [27]. In this paper we consider plane stress assumption as the regularization to the optimization problem.

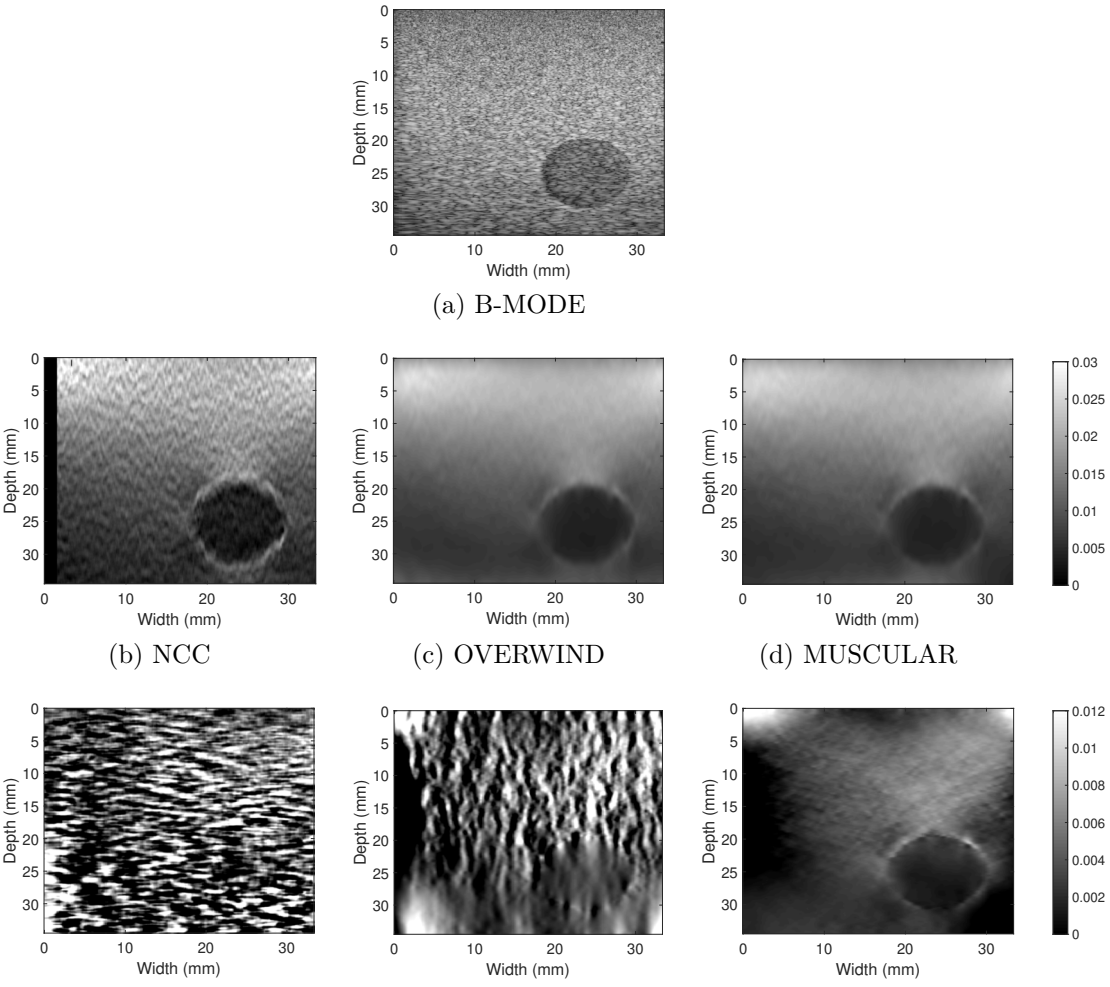


(a) B-MODE

(b) NCC (c) OVERWIND (d) MUSCULAR

(f) NCC (g) OVERWIND (h) MUSCULAR

Figure 6.5: B-mode image of the inclusion one in the phantom is shown in (a). The estimated axial strains by NCC, OVERWIND and MUSCULAR are shown in (b)-(d). Figures (f)-(h) show the estimated lateral strain by NCC, OVERWIND and MUSCULAR, respectively.

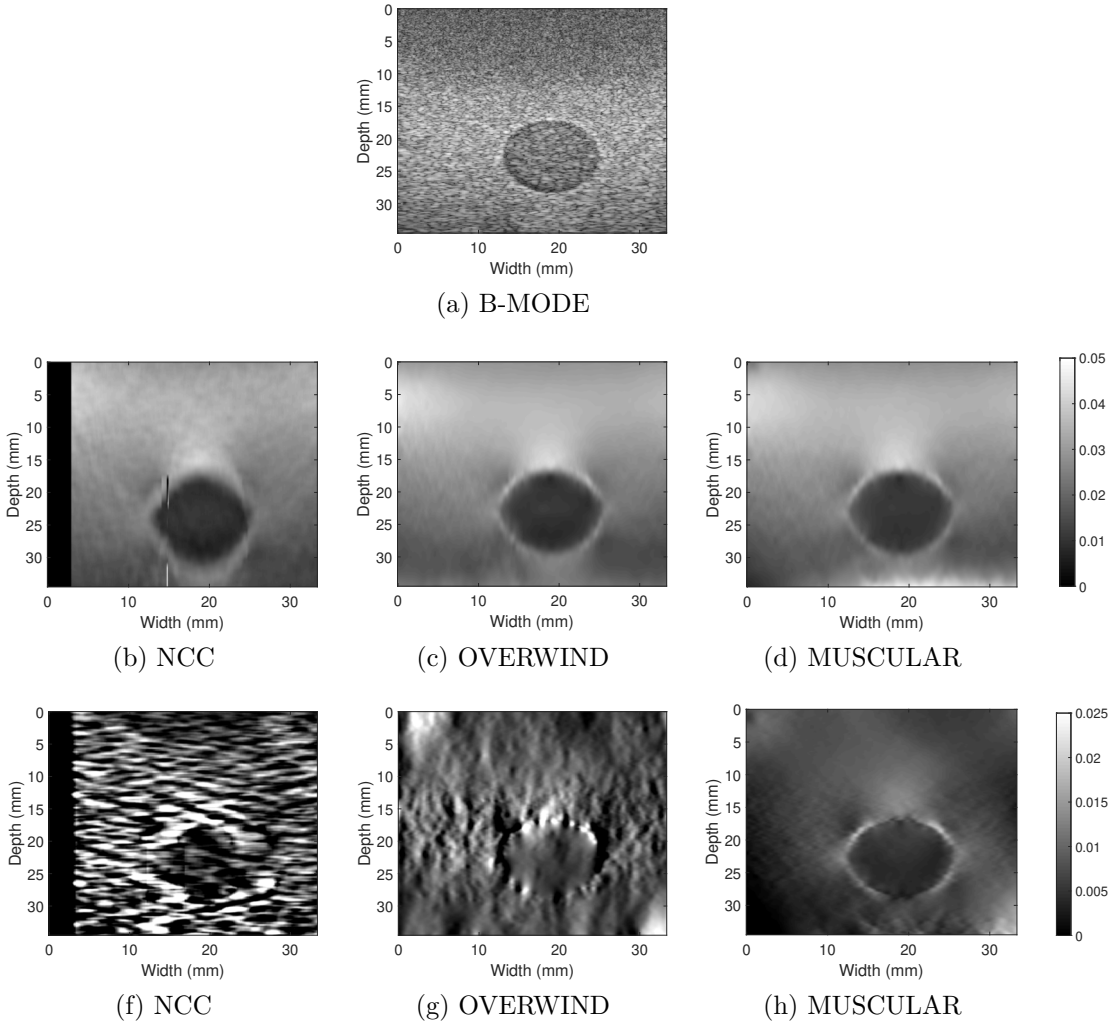


(a) B-MODE

(b) NCC (c) OVERWIND (d) MUSCULAR

(f) NCC (g) OVERWIND (h) MUSCULAR

Figure 6.6: B-mode image of the inclusion two in the phantom is shown in (a). The estimated axial strains by NCC, OVERWIND and MUSCULAR are shown in (b)-(d). (f)-(h) are the estimated lateral strain by NCC, OVERWIND and MUSCULAR, respectively.

### 6.1.1 MUSCULAR: Mechanical_based qUaSi-statiC Ultrasound eLAstogRaphy

$$
\begin{aligned}
D_{i,j} = \; & \tfrac{1}{L}\Sigma_{k,r}\Big(I_1(i+k,j+r) - I_2(i+k+a_{i,j},j+r+l_{i,j}) - \Delta a_{i,j}\frac{\partial I_2(i+k+a_{i,j},j+r+l_{i,j})}{\partial y} \\
& -\Delta l_{i,j}\frac{\partial I_2(i+k+a_{i,j},j+r+l_{i,j})}{\partial x}\Big)^2, \\
R_{i,j} = \; & \alpha_1 \mid \frac{\partial \bar{a}_{i,j}}{\partial y} - \theta_a \mid + \alpha_2 \mid \frac{\partial \bar{a}_{i,j}}{\partial x} \mid + \beta_1 \mid \frac{\partial \bar{l}_{i,j}}{\partial y} \mid + \beta_2 \mid \frac{\partial \bar{l}_{i,j}}{\partial x} - \theta_l \mid .
\end{aligned}
\tag{6.1}
$$

---

In quasi-static USE, loading in the out of plane direction is small, which makes the plane stress approximation a proper assumption for relating the deformations in axial and lateral directions [109]. By considering the displacement vector as $\mathbf{u} = [\bar{a}_{i,j}, \bar{l}_{i,j}]^T$, the plane stress assumption can be modeled as [27]

$$\nabla.\mathbf{A}(\boldsymbol{\varepsilon}_{i,j}) = 0 \tag{6.2}$$

where

$$\mathbf{A}(\boldsymbol{\varepsilon}_{i,j}) = 2tr(\boldsymbol{\varepsilon}_{i,j})\mathbf{I} + 2\boldsymbol{\varepsilon}_{i,j} \tag{6.3}$$

and $\boldsymbol{\varepsilon}_{i,j}$ is the 2D linearized strain tensor as

$$\boldsymbol{\varepsilon}_{i,j} = \frac{\nabla \mathbf{u}_{i,j} + \nabla \mathbf{u}_{i,j}{}^T}{2}. \tag{6.4}$$

The extended form of Eq. (6.2) can be written as

$$
\begin{aligned}
4\frac{\partial^2 \bar{a}_{i,j}}{\partial y^2} + \frac{\partial^2 \bar{a}_{i,j}}{\partial x^2} + 3\frac{\partial^2 \bar{l}_{i,j}}{\partial xy} = 0 \\
4\frac{\partial^2 \bar{l}_{i,j}}{\partial x^2} + \frac{\partial^2 \bar{l}_{i,j}}{\partial y^2} + 3\frac{\partial^2 \bar{a}_{i,j}}{\partial xy} = 0
\end{aligned}
\tag{6.5}
$$

In the MUSCULAR method we add the Eq.(6.5) as regularization parameters to the optimization problem. As optimizing the new cost function makes divergence in the bottom part of the tissue, we add a new term to limit the displacement of the last row to the estimated integer displacement by DP. The proposed cost function for MUSCULAR is as

$$C = \Sigma_{j=1}^{n}\Sigma_{i=1}^{m} D_{i,j} + R_{i,j} + W_{i,j} + \lambda_3 \Delta^2 a_{mj} \tag{6.6}$$

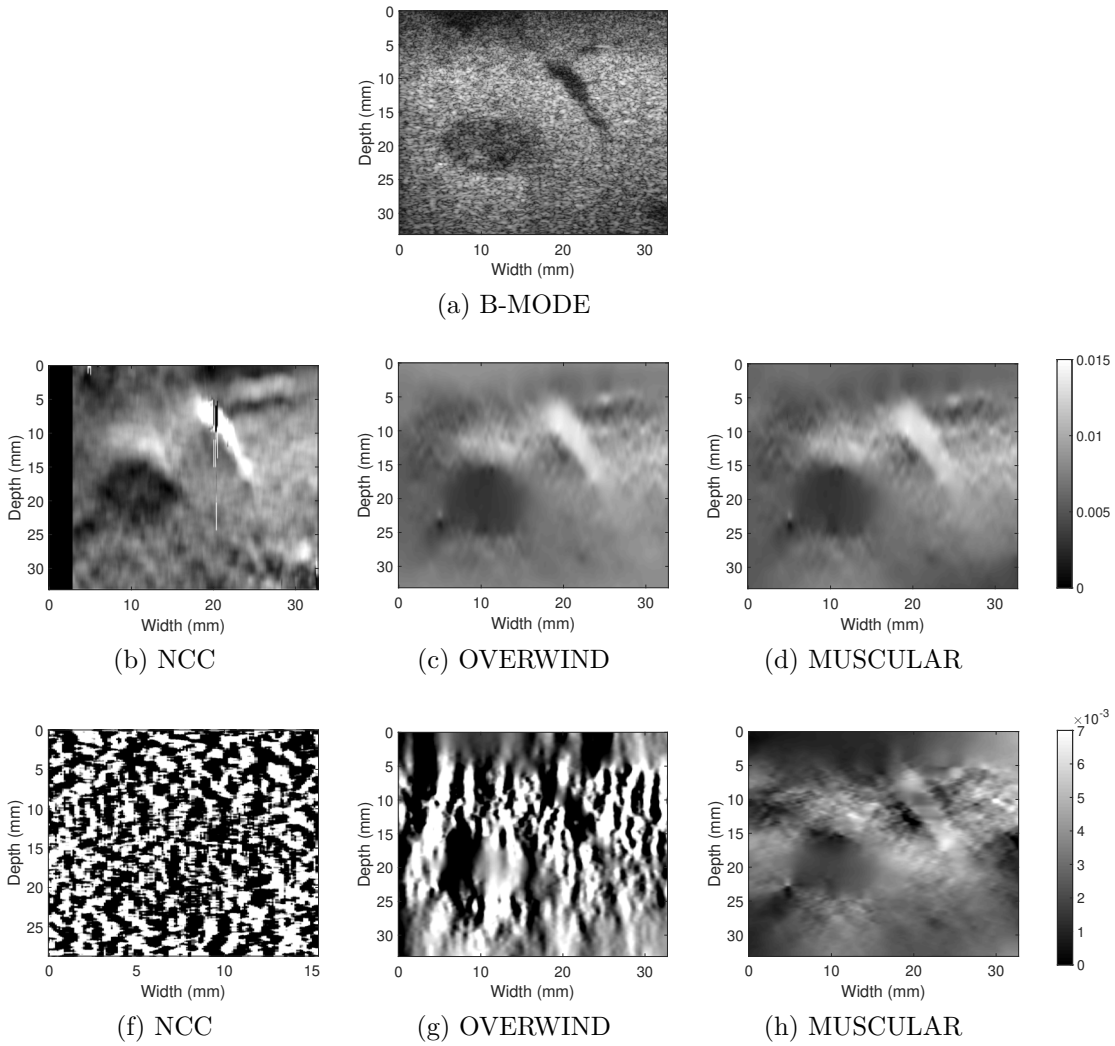


(a) B-MODE

(b) NCC (c) OVERWIND (d) MUSCULAR

(f) NCC (g) OVERWIND (h) MUSCULAR

Figure 6.7: B-mode image of patient 1 is shown in (a). The estimated axial strains by NCC, OVERWIND and MUSCULAR are shown in (b)-(d). (f)-(h) are the estimated lateral strain by NCC, OVERWIND and MUSCULAR, respectively.

where

$$W_{i,j} = \lambda_1(4\frac{\partial^2 a}{\partial y^2} + \frac{\partial^2 a}{\partial x^2} + 3\frac{\partial^2 l}{\partial xy})^2 + \lambda_2(4\frac{\partial^2 l}{\partial x^2} + \frac{\partial^2 l}{\partial y^2} + 3\frac{\partial^2 a}{\partial xy})^2.$$

By differentiating Eq. (6.6) with respect to $\Delta a_{i,j}$ and $\Delta l_{i,j}$ and setting them to zero and stacking all $2mn$ unknown parameters in a vector as $\Delta d_{2mn} = [\Delta a_{1,1}, \Delta l_{1,1}, \Delta a_{1,2}, ..., \Delta l_{m,n}]^T$, we end up with a linear equation as $M\Delta d = b$. By solving this linear equation we obtain the optimal subsample displacements.

### 6.1.2 Tunning the regularization parameters

The proposed cost function of MUSCULAR has seven regularization parameter and by properly tunning these parameters, deformation of any kind of material can be estimated. However, most biological soft tissues can be considered as an almost incompressible tissues [8]. In this section, we describe how regularization parameters of the MUSCULAR can be related to each other for almost incompressible tissues. By relating regularization paramters to each other, seven parameters are reduced to three independent regularization parameters that could be tunned easily.

In incompressible tissues, compression does not change the volume of the tissue. In such materials, the Poisson's ratio as a relationship between compression/extension of tissue in lateral direction and extension/compression in axial direction is about 0.5 [95, 110]. The parameters $\alpha_1$ and $\beta_1$ in Eq.(6.6), represent the regularization of axial and lateral displacements in axial direction, then by assuming the Poisson's ratio for biological tissues about 0.5, we can set $\beta_1 = 0.5\alpha_1$. Similarly, we can set $\beta_2 = 0.5\alpha_2$.

In the next step, we relate $\alpha_1$ and $\alpha_2$ to each other. To this end, the point spread function (PSF) of the ultrasound RF data should be known. Then the size of PSF in axial and lateral direction could be measured as shown in Fig. 6.1. The relationship between $\alpha_1$ and $\alpha_2$ can be represented as

$$\frac{\alpha_1}{\alpha_2} = \frac{Y}{X} \times \frac{S_A}{S_L}, \tag{6.7}$$

where $S_A$ and $S_L$ are sampling rates in axial and lateral directions, respectively.

As mentioned, MUSCULAR can estimate displacement for all imaging modalities, however as the focus of the present manuscript is ultrasound, we can set the $\lambda_2 = 0$. A rough explanation for $\lambda_2 = 0$ is that the number of samples in lateral direction is much less than axial direction and this makes the second order gradient in lateral direction very large compared to axial direction, therefore $\lambda_2$ should be much less than $\lambda_1$ in Eq. (6.6). The remained three regularization parameters can be tuned easily as they do not affect the performance of each other. $\alpha_1$ is smoothing the estimations in axial directions. $\lambda_1$ is for accuracy of lateral displacement and $\lambda_3$ is for prohibiting MUSCULAR from divergence at the bottom part of the estimations. The code of MUSCULAR will be publicly available following the publication of the paper.

### 6.1.3 Data Acquisition and comparison metrics

For validation of better performance of MUSCULAR compared to other USE techniques, we perform simulation, phantom and *in-vivo* experiments. In this section, the data that are utilized in different experiments of the paper are described and then the performance of the MUSCULAR is compared to other methods in Results Section. For quantitative assessing the MUSCULAR method, CNR metric is used [7, 90]

$$\text{CNR} = 20\ \log_{10}\Big(\frac{2(\bar{s}_b - \bar{s}_t)^2}{\sigma_b^2 + \sigma_t^2}\Big), \tag{6.8}$$

where $\bar{s}_t$ and $\bar{s}_b$ are the strain averages and $\sigma_t^2$ and $\sigma_b^2$ are the strain variances of the target and background windows, respectively. For the simulation study, as we know the ground truth strain values, Root Mean Square Error (RMSE) is also calculated as

$$\text{RMSE\%} = 100 * \frac{\sqrt{m \times n \times \sum_{i=1}^{m}\sum_{j=1}^{n}\left(S_e(i,j) - S_g(i,j)\right)^2}}{\sum_{i=1}^{m}\sum_{j=1}^{n} S_g(i,j)}, \tag{6.9}$$

where $m$ and $n$ are size of estimated strains. $S_e$ and $S_g$ are estimated and ground truth strains, respectively.

#### Simulation Data

We have simulated a $20 \times 20\ mm^2$ phantom utilizing Field II ultrasound simulation software [73, 111]. The imaging probe consists of 128 elements with pitch of 0.15 mm operating at the center frequency of 7 MHz and the sampling rate is 100 MHz. The simulated phantom consists of a homogeneous region with a Young's modulus of 4 $kPa$ and one cylindrical inclusion with a Young's modulus of 40 $kPa$. We have compressed the phantom 1% using the ABAQUS software package (Johnston, RI, USA) as Finite Element Method (FEM)-based software with triangular mesh sizes of 0.05 $\text{mm}^2$.

#### Phantom Data

The phantom experiment is carried out at PERFORM centre, Concordia University. Two sets of the phantom data are acquired from a tissue mimicking breast phantom (059 tissue mimicking breast phantom, CIRS tissue simulation & phantom technology, Norfolk, VA, USA) using an E-Cube R12 ultrasound machine (Alpinion, Bothell, WA, USA) in different compression levels. The imaging probe is L3-12H probe operated at the center frequency of 8 MHz and sampling frequency of 40 MHz.

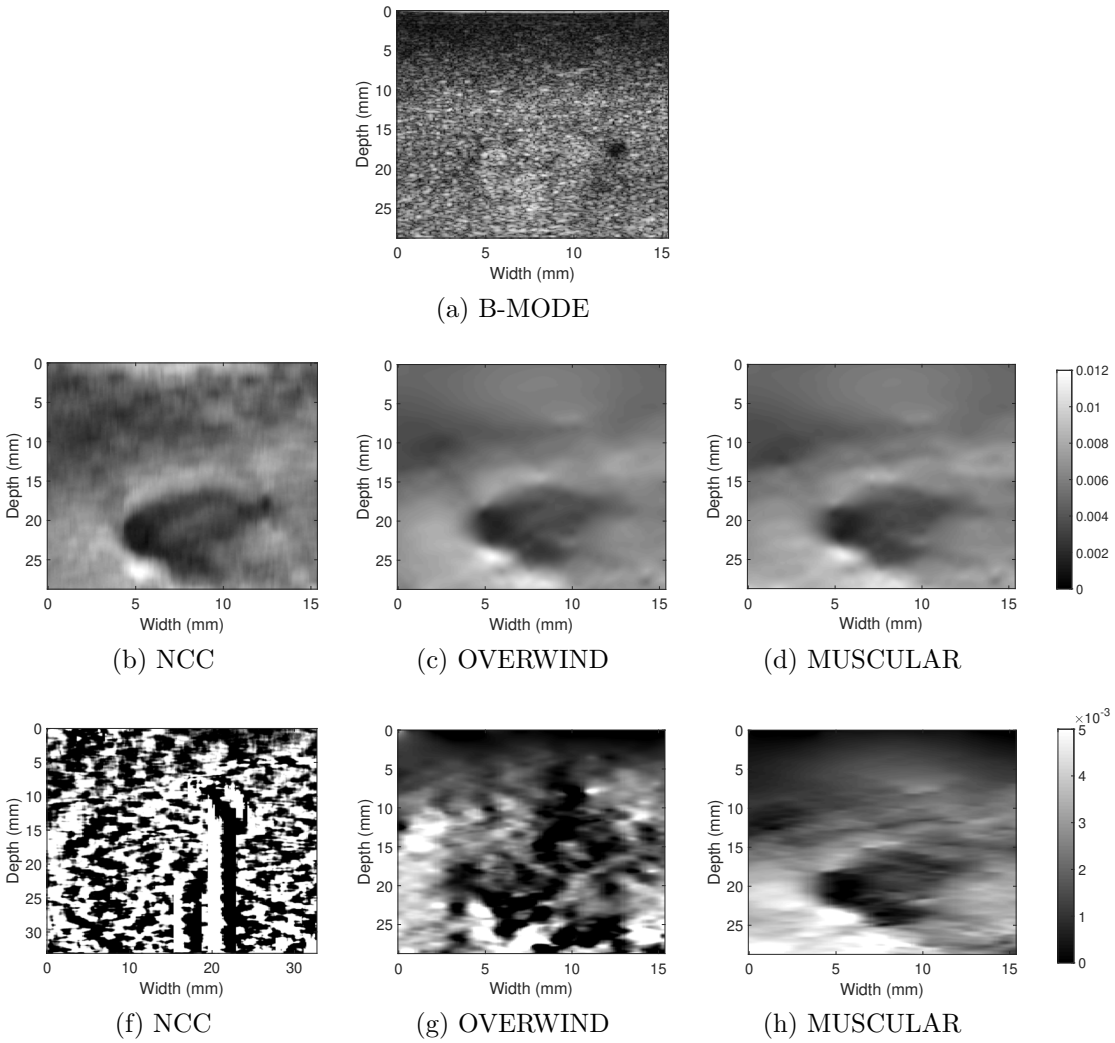


(a) B-MODE

(b) NCC (c) OVERWIND (d) MUSCULAR

(f) NCC (g) OVERWIND (h) MUSCULAR

Figure 6.8: B-mode image of patient 2 is shown in (a). The estimated axial strains by NCC, OVERWIND and MUSCULAR are shown in (b)-(d). Figures (f)-(h) are the estimated lateral strain by NCC, OVERWIND and MUSCULAR, respectively.

### *In-vivo* Data

For *in-vivo* experiment, we have analyzed two data sets collected at the Johns Hopkins hospital from two patients with liver cancer. The RF data are recorded with an Antares ultrasound machine (Siemens, Issaquah, WA, USA) using a VF10-5 linear probe with operating at center frequency of 6.6 MHz and sampling frequency of 40 MHz. The study was approved by the ethics institutional review board at Johns Hopkins University.

## 6.2 Results

### Simulation Results

Displacement of simulated data is estimated by NCC, OVERWIND and MUSCULAR methods. Estimated Displacements are differentiated by the LSQ and strains are shown in Fig. 6.2. Estimated axial strain by MUSCULAR is close to that of OVERWIND. However, the estimated lateral strain by MUSCULAR significantly outperforms other methods. For better visualizing the improved estimated lateral strain by MUSCULAR, we consider two lines shown by green at Fig. 6.2 (f) and plot the Edge Spread Function (ESF) of estimation with different methods across these lines. As shown in Fig. 6.3, results of MUSCULAR are much closer to the ground truth compared to OVERWIND and NCC. Table 6.1 is a quantitative comparison between three methods which indicates a remarkable decrease in RMSE and significant increase in CNR of estimated strain by MUSCULAR.

For the simulated data, $\alpha_1$ should be about 60 times bigger than $\alpha_2$ according to Eq.(6.7). For validating this ratio, we estimate the RMSE of ground truth with the results of MUSCULAR, estimated with different combination of regularizations for $\alpha_1$ and $\alpha_2$ as shown in Fig. 6.4. For better visualization, we have normalized each row of the Fig. 6.4. According to the presented RMSE map, for an arbitrary $\alpha_1$, the lowest RMSE is achieved by setting the $\alpha_2$ to a number that is almost 60 times less than $\alpha_1$.

### Phantom Results

Fig. 6.5 shows the axial and lateral estimation for the first inclusion of the phantom with compression rate about 2%. Similar to the simulation study, axial strain of MUSCULAR is close to the estimated axial strain by OVERWIND, however there is a large improvement in the lateral strain. As there is no ground truth for the phantom study, we can compare the strain value of lateral strain with the axial strain as an accuracy metric for the estimated lateral strain. As shown in Fig. 6.5-(b),(c) the axial strain is in a range of $0\% - 2.5\%$, by assuming the Poisson ratio of 0.5 for the soft tissue, we expect a strain value in range of $0\% - 1.2\%$ for the lateral strain which agrees with the estimated lateral strain by MUSCULAR in Fig. 6.5 (h).

Table 6.1: Quantitative comparison of simulation results.

| | | RMSE(%) | CNR(dB) |
|---|---|---|---|
| Axial | NCC | 34.98 | 23.09 |
| | OVERWIND | 19.01 | 48.53 |
| | **MUSCULAR** | **17.40** | **50.28** |
| Lateral | NCC | 394.72 | -35.90 |
| | OVERWIND | 247.73 | -17.68 |
| | **MUSCULAR** | **64.31** | **16.38** |

Fig. 6.6 is the result of second phantom data with the compression level of about 4%. Similar to the previous experiment axial strains are almost the same, but a significant improvement in the lateral direction. As high resolution, longitudinal behavior and high sampling frequency in the axial direction implies a more accurate estimation in the axial direction, we consider axial strain as a reference with estimated range of $0\% - 4\%$. By assuming the Poisson ratio as 0.5, we expect a lateral strain in the range of $0\% - 2\%$ which agrees with Fig. 6.6(f).

### *In-vivo* Results

Figs. 6.7 and 6.8 are the results of two patients with liver cancer. In both of the data sets, MUSCULAR has estimated lateral strains better than other methods. Besides of visual improvement by MUSCULAR that detects the tumors in lateral strain, the lateral strain value of the MUSCULAR can be validated by assuming the axial strain as a reference, similar to the phantom results. The almost half strain range in the lateral direction compared to axial direction, clarifies that lateral strain is not biased by axial strain which is one the main limitation of the the methods that try to reconstruct lateral strain based on axial strain.

Calculating strain tensor requires differentiating displacement in different directions. In this manuscript we presented only the two axial and lateral strains, but future work can use the output of MUSCULAR to estimate more components of the strain tensor. To decrease the noise effect in differentiating, we have used the well-known LSQ method. The number of samples considered for LSQ determines the smoothness of the calculated strains. In both OVERWIND and MUSCULAR the number of samples we have considered for LSQ is about 5% of the total data size. For a fair comparison the size of LSQ is about 10% of the total data size for NCC method as NCC does not have any regularization in displacement estimation step.

NCC is implemented in MATLAB by considering windows of size $51 \times 9$ samples by 90% overlap between consecutive windows. The proposed TDPE method in [60]

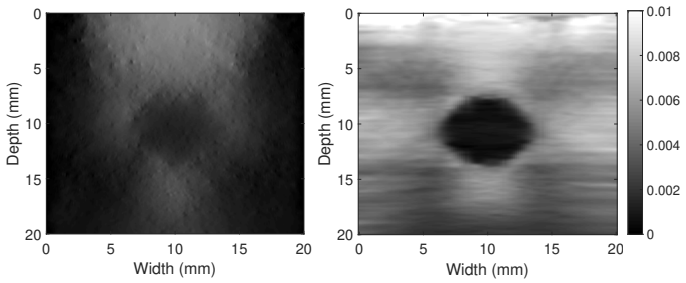


(a) Interpolated OVERWIND (b) MUSCULAR

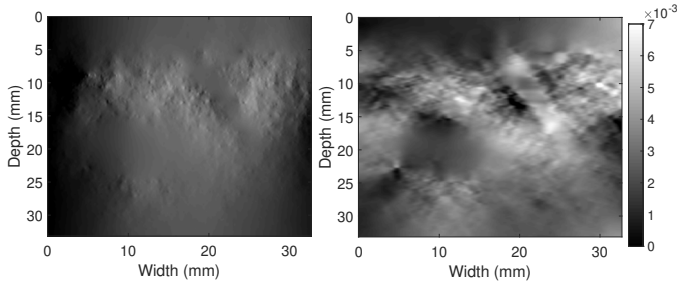


(d) Interpolated OVERWIND (e) MUSCULAR

Figure 6.9: Estimated lateral strain for the simulation (top row) and *in-vivo* data (bottom row). (a) and (d) are the result of OVERWIND on interpolated simulation and *in-vivo* RF data, respectively. (b) and (e) are the result of MUSCULAR on the original simulation and *in-vivo* RF data, respectively.

is also utilized to prevent the false peaks as much as possible by limiting the search range based on displacement of neighboring windows. The position of window by maximum NCC in the post compressed data provides only the integer displacement. Interpolating NCC values of all windows in the search range determined by TPDE by factor of 100 in both directions utilizing spline based interpolation, provides a smooth surface of NCCs. By calculating maximum of the smoothed surface and its corresponding position, the exact displacement is estimated.

## 6.3 Conclusions

We proposed a method called MUSCULAR for estimating lateral displacement with high accuracy which is an important step in quasi static USE for estimating Young's modulus. MUSCULAR calculates the displacement by optimizing a regularized cost function. The cost function involves intensity similarity of pre- and post-compressed data, continuity of displacement for neighboring samples and also plane stress approximation for making a link between deformation in axial and lateral directions. The improvement of estimation is significant compared to two powerful methods as regularized optimization based and window based techniques.

Interpolating data, beam steering and reconstructing displacement based on initial estimations are some supplementary techniques that can be implemented for all 2D estimation methods including MUSCULAR to increase accuracy of estimation. In contrast with other 2D displacement estimation methods that computationally complex pre- or post-processing techniques are essential for improving the lateral estimation, MUSCULAR estimates high accuracy deformation without exploiting supplementary steps and it significantly reduces the computational complexity. Besides outperforming other estimations techniques as shown in Results Section, MUSCULAR has a better performance compared to these techniques even by implementing additional steps. Fig. 6.9 compares the performance of MUSCULAR implemented on original RF data with the performance of OVERWIND implemented on spline-based interpolated RF data by factor of 10 in lateral direction. As shown in Fig. 6.9, interpolating data improves the results of OVERWIND, but MUSCULAR still has a much better performance.

# Chapter 7

# Conclusions and Future Work

## 7.1 Conclusions

USE is a well-known technique for extracting pathological information of the tissue by estimating strain distribution and Lamé constants. It is a non-invasive technique that has untapped potential in early diagnosis and treatment of diseases that change the mechanical properties of the tissue. Ablation guidance and monitoring, differentiating benign thyroid nodules from malignant ones and breast lesion characterization are some of the evolving clinical applications of USE.

Different classifications for USE are proposed in the literature, however, it can be broadly grouped into dynamic and quasi-static USE. The main difference in the two USE groups is how the tissue is deformed with the quasi-static approaches applying a static compression of the tissue, while the dynamic approaches typically propagating mechanical waves in the tissue. However, in both methods, TDE between pre- and post-deformed tissue should be estimated as the first step. In this thesis, we developed novel methods for increasing the accuracy of TDE which is crucial for estimating Lamé constants as the next step of USE. The proposed TDE techniques (except for MUSCULAR in Chapter 6) can be utilized for both dynamic and quasi-static USE. However, all the experiments of this thesis are for quasi-static USE, wherein, tissues are slowly compressed by simply pressing the probe against the tissue.

Even though, the probe is pressed uniformly in axial direction, deformation of tissue in both lateral and out-of-plane directions is inevitable. An ideal TDE technique should estimate deformation in 3D, but would require 3D ultrasound imaging. To make TDE methods compatible with conventional 2D ultrasound imaging, we neglect the deformation in out-of-plane direction and assume each sample moves in a 2D plane. Even after neglecting out-of-plane motion, each sample has two unknown variables that should be estimated. As the intensity of each sample is the only known parameter, TDE becomes an ill-posed problem. Different techniques and assumptions based on the continuity and very similar displacement of neighboring samples are proposed to make TDE a well-posed problem.

Window-based tracking methods are among the oldest and most popular techniques for TDE. For estimating displacement of one sample, a window is considered around the sample assuming that all samples inside the window have exactly the same displacement. A window of samples in the post-deformed data with maximum similarity would provide the displacement of the sample in the center of window. One of the main disadvantage of these techniques is high sensitivity to de-correlation of samples in pre- and post-deformed data which is inevitable due to different factors such as blood flow and other biological motions common in *in-vivo* data. Increasing the size of window makes these techniques more robust to signal de-correlation at the cost of over-smoothing the estimated displacement and loosing useful information. Experimental study in [112, 113] demonstrate the windows with size of $10\lambda$ in axial direction, where $\lambda$ is the wavelength of ultrasound signal has the optimum performance. In Chapter 2, we proposed two methods to extend the assumption of spatial continuity to temporal continuity or using channel data instead of RF data. The proposed methods keep the spatial size of windows fixed, but increase size of windows by adding non-spatial information and makes the TDE more robust to signal de-correlation without spatial over-smoothing.

The first proposed method is STNCC (introduced in Chapter 2) wherein the information of the temporally neighbors is utilized for TDE. In this method, we benefit from the high frame rate of ultrasound imaging which is about 30 frame per seconds for traditional ultrasound imaging. Therefore, we can assume that temporally neighboring samples have close displacement. The second proposed method is CNCC (introduced in Chapter 2) which increases the size of windows by considering pre-beamformed data instead of beamformed RF data. The underlying idea for CNCC is that for generating one sample, several channels collect data and after applying appropriate time-delay, they sum up to generate the sample. We proposed to increase size of windows by considering all information collected by different channels.

Regularized optimization-based techniques are another class of TDE methods. The main concept behind these techniques is minimizing a cost function that comprises a data term and a regularization term. The data term compares intensities of pre- and post-compressed data, while the regularization term penalize displacement of neighboring samples to be close to each other. In Chapter 3, a method named OVERWIND is proposed for TDE as a regularized optimization-based techniques. Inspired by window-based techniques, the data term of OVERWIND compares intensities of windows in pre- and post-compressed data which enhances the robustness of the TDE. The second novelty of OVERWIND is utilizing total variation regularization (L1 norm) instead of commonly used squared regularization (L2 norm). Squared regularization is a popular choice for optimization as it is differentiable and makes the optimization straight forward, however it causes over-smoothing especially at the borders of the inclusions. We used L1 norm for the regularization term of OVERWIND which assigns a smaller penalty to discontinuities. This modification added nonlinear terms to the cost function, and therefore, we used iterative methods to optimize the cost function.

To the best of our knowledge, all previously proposed TDE techniques used RF data for displacement estimation. In Chapter 2, we proposed CNCC and used pre-beamformed channel data for the first time for window-based techniques resulting in significant improvement in the results. Inspired by CNCC, we used pre-beamformed channel data for regularized optimization-based technique in Chapter 4 and named the method CGLUE. In contrast with CNCC, there is a closed form solution for CGLUE which allows us to analytically compare its accuracy with other regularized optimization-based methods. We analytically compared CGLUE with a recently published method GLUE and proved that the error of estimated displacement by CGLUE in less than estimation of GLUE. This comparison directly focuses on the advantage of utilizing pre-beamformed channel data since that is the only difference between GLUE and CGLUE.

Previously proposed methods estimate displacement in both axial and lateral directions. However estimation in the axial direction is notably more accurate than lateral direction. Low accuracy of lateral displacement estimation is one of the most important challenges for USE, as the Lamé parameters are calculated based on estimated displacements. The main reasons for poor lateral estimation are low sampling rate, low resolution and lack of carrier signal in this direction. Interpolating data in lateral direction is the main approach proposed in the literature for addressing the first limitation. In Chapter 5, we proposed to use VSSA as an advanced beamforming technique for TDE to address the first and second limiting factors. In a nutshell, VSSA is the combination of SA and line-by-line imaging, which enables increased resolution and sampling rate in lateral direction as well as improving the beam strength in deep regions. The results presented in Chapter 5 show the outstanding performance of VSSA compared to interpolation.

Although the idea of utilizing VSSA helped us in improving accuracy of lateral displacement estimation, still it is not compatible with axial estimation. Moreover, VSSA increases computational cost of TDE by increasing size of data. In Chapter 6, we proposed a method named MUSCULAR to increase the estimation accuracy in lateral direction without increasing data size. In this method, we benefit form the mechanical behavior of the compressed biological tissue in quasi-static USE. On one hand, the biological tissues are nearly in-compressible and on the other hand, pressure of the probe in free-hand palpation quasi-static USE is approximately uniform, and the size of probe in out-of-plane direction is typically small. The mechanical information makes the plane stress approximation a valid one for modeling the deformation of the tissue. In the MUSCULAR method, we modified the regularization term of previously developed OVERWIND by adding the information of plane stress approximation.

## 7.2 Future Work

USE is an interesting research subject with numerous clinical applications that has attracted a lot of researchers. Although a large number of papers get published in

this field every year, there is still room for increasing the accuracy of USE and TDE. The limiting factors of the TDE are mostly known, but an interesting question is the impact of each limiting factor on the accuracy of TDE. A wide simulation study that studies different limitations and their impact on TDE would be very interesting and helpful. Moreover, addressing some high-impact limitations like low resolution of ultrasound data do not necessarily guarantee enhanced accuracy of the TDE as increasing resolution would lead to a decreased signal-to-noise ratio of the data. An interesting research work is studying the relation of resolution and signal-to-noise ratio with TDE. The aforementioned research could expedite developing high accuracy TDE methods.

One of the challenges of TDE is validating metrics, especially for experimental data that does not have ground truth. Although the relation of CNR and accuracy of TDE is studied in the literature, it is also shown that CNR as the only metric of TDE is not a very strong metric. Developing better metrics instead of CNR for validation of experimental results is a vary interesting research area. Recent work has investigated how experimental data can be selected for TDE methods [114]. The correct data for any TDE methods assures the best performance of TDE method, but still the main question for validating and comparing performance of different TDE methods are remained.

Estimating Lamé constants requires calculating strain tensor. The present pipeline of estimating strain tensor is estimating motion and differentiating displacement in different directions. The artifacts and noise in motion estimation is inevitable and their impact would be magnified in differentiating step. The most popular technique for reducing the noise in strain tensor is utilizing LSQ. However it reduce the impact of noise by smoothing the result which highly affects the precision. Developing techniques that directly estimate strain tensor is of high impact in USE.

Deep learning is a fast developing tool for addressing variety of problems including registration and motion estimation. Few studies have trained deep networks and more specifically CNN networks for TDE. However, the accuracy of the proposed networks still is not compatible with classical methods of TDE. One of main limitations for deep learning techniques in all medical applications including TDE is limited data sets. Developing deep learning methods that can estimated motion of tissue is another interesting research topic.

Aberration correction is an interesting research field to compensates difference of sound wave in different part of a heterogeneous tissue [115]. The aberration is a source of error in the elastography that is not addressed. The CGLUE project that utilizes channel data for elastography can be modified to find the speed of sound as well as displacement in different parts of tissue.

# Bibliography


[1] J. Bamber, D. Cosgrove, C. Dietrich, J. Fromageau, J. Bojunga, F. Calliada, V. Cantisani, J.-M. Correas, M. D'onofrio, E. Drakonaki, *et al.*, "Efsumb guidelines and recommendations on the clinical use of ultrasound elastography. part 1: Basic principles and technology," *Ultraschall in der Medizin-European Journal of Ultrasound*, vol. 34, no. 02, pp. 169–184, 2013.

[2] H. Rivaz, E. M. Boctor, M. A. Choti, and G. D. Hager, "Real-time regularized ultrasound elastography," *IEEE transactions on medical imaging*, vol. 30, no. 4, pp. 928–945, 2011.

[3] J. L. Prince and J. M. Links, *Medical imaging signals and systems*. Pearson Prentice Hall Upper Saddle River, 2006.

[4] R. S. Cobbold, *Foundations of biomedical ultrasound*. Oxford university press, 2006.

[5] M. Halliwell, "A tutorial on ultrasonic physics and imaging techniques," *Proceedings of the Institution of Mechanical Engineers, Part H: Journal of Engineering in Medicine*, vol. 224, no. 2, pp. 127–142, 2010.

[6] N. Wagner, Y. C. Eldar, and Z. Friedman, "Compressed beamforming in ultrasound imaging," *IEEE Transactions on Signal Processing*, vol. 60, no. 9, pp. 4643–4657, 2012.

[7] J. Ophir, S. K. Alam, B. Garra, F. Kallel, E. Konofagou, T. Krouskop, and T. Varghese, "Elastography: ultrasonic estimation and imaging of the elastic properties of tissues," *Proceedings of the Institution of Mechanical Engineers, Part H: Journal of Engineering in Medicine*, vol. 213, no. 3, pp. 203–233, 1999.

[8] A. Skovoroda, S. Emelianov, and M. O'donnell, "Tissue elasticity reconstruction based on ultrasonic displacement and strain images," *IEEE transactions on ultrasonics, ferroelectrics, and frequency control*, vol. 42, no. 4, pp. 747–765, 1995.

[9] X. Pan, K. Liu, J. Bai, and J. Luo, "A regularization-free elasticity reconstruction method for ultrasound elastography with freehand scan," *Biomedical engineering online*, vol. 13, no. 1, p. 132, 2014.

[10] M. Pernot, K. Fujikura, S. D. Fung-Kee-Fung, and E. E. Konofagou, "Ecg-gated, mechanical and electromechanical wave imaging of cardiovascular tissues in vivo," *Ultrasound in medicine & biology*, vol. 33, no. 7, pp. 1075–1085, 2007.

[11] E. E. Konofagou, J. Luo, D. Saluja, D. O. Cervantes, J. Coromilas, and K. Fujikura, "Noninvasive electromechanical wave imaging and conduction-relevant velocity estimation in vivo," *Ultrasonics*, vol. 50, no. 2, pp. 208–215, 2010.

[12] J. Luo, K. Fujikura, L. S. Tyrie, M. D. Tilson, and E. E. Konofagou, "Pulse wave imaging of normal and aneurysmal abdominal aortas in vivo," *IEEE transactions on medical imaging*, vol. 28, no. 4, pp. 477–486, 2008.

[13] J. Bercoff, M. Tanter, and M. Fink, "Supersonic shear imaging: a new technique for soft tissue elasticity mapping," *IEEE transactions on ultrasonics, ferroelectrics, and frequency control*, vol. 51, no. 4, pp. 396–409, 2004.

[14] T. Gallot, S. Catheline, P. Roux, J. Brum, N. Benech, and C. Negreira, "Passive elastography: shear-wave tomography from physiological-noise correlation in soft tissues," *IEEE transactions on ultrasonics, ferroelectrics, and frequency control*, vol. 58, no. 6, pp. 1122–1126, 2011.

[15] K. Nightingale, S. McAleavey, and G. Trahey, "Shear-wave generation using acoustic radiation force: in vivo and ex vivo results," *Ultrasound in medicine & biology*, vol. 29, no. 12, pp. 1715–1723, 2003.

[16] D. M. Dumont and B. C. Byram, "Robust tracking of small displacements with a bayesian estimator," *IEEE transactions on ultrasonics, ferroelectrics, and frequency control*, vol. 63, no. 1, pp. 20–34, 2015.

[17] L. Sandrin, M. Tanter, J.-L. Gennisson, S. Catheline, and M. Fink, "Shear elasticity probe for soft tissues with 1-d transient elastography," *IEEE transactions on ultrasonics, ferroelectrics, and frequency control*, vol. 49, no. 4, pp. 436–446, 2002.

[18] J. Ophir, I. Cespedes, H. Ponnekanti, Y. Yazdi, and X. Li, "Elastography: a quantitative method for imaging the elasticity of biological tissues," *Ultrasonic imaging*, vol. 13, no. 2, pp. 111–134, 1991.

[19] G. Treece, J. Lindop, L. Chen, J. Housden, R. Prager, and A. Gee, "Real-time quasi-static ultrasound elastography," *Interface focus*, vol. 1, no. 4, pp. 540–552, 2011.

[20] C. Schneider, A. Baghani, R. Rohling, and S. Salcudean, "Remote ultrasound palpation for robotic interventions using absolute elastography," in *International Conference on Medical Image Computing and Computer-Assisted Intervention*, pp. 42–49, Springer, 2012.

[21] T. Adebar, S. Salcudean, S. Mahdavi, M. Moradi, C. Nguan, and L. Goldenberg, "A robotic system for intra-operative trans-rectal ultrasound and ultrasound elastography in radical prostatectomy," in *International Conference on Information Processing in Computer-Assisted Interventions*, pp. 79–89, Springer, 2011.

[22] R. Xia, G. Tao, and A. Thittai, "Dynamic frame pairing in real-time freehand elastography," *IEEE transactions on ultrasonics, ferroelectrics, and frequency control*, vol. 61, no. 6, pp. 979–985, 2014.

[23] T. J. Hall, Y. Zhu, and C. S. Spalding, "In vivo real-time freehand palpation imaging," *Ultrasound in medicine & biology*, vol. 29, no. 3, pp. 427–435, 2003.

[24] S. Bharat, T. Varghese, E. L. Madsen, and J. A. Zagzebski, "Radio-frequency ablation electrode displacement elastography: A phantom study," *Medical physics*, vol. 35, no. 6Part1, pp. 2432–2442, 2008.

[25] H. Rivaz, I. Fleming, L. Assumpcao, G. Fichtinger, U. Hamper, M. Choti, G. Hager, and E. Boctor, "Ablation monitoring with elastography: 2d in-vivo and 3d ex-vivo studies," in *International Conference on Medical Image Computing and Computer-Assisted Intervention*, pp. 458–466, Springer, 2008.

[26] H. Rivaz, P. Foroughi, I. Fleming, R. Zellars, E. Boctor, and G. Hager, "Tracked regularized ultrasound elastography for targeting breast radiotherapy," in *International Conference on Medical Image Computing and Computer-Assisted Intervention*, pp. 507–515, Springer, 2009.

[27] O. A. Babaniyi, A. A. Oberai, and P. E. Barbone, "Recovering vector displacement estimates in quasistatic elastography using sparse relaxation of the momentum equation," *Inverse problems in science and engineering*, vol. 25, no. 3, pp. 326–362, 2017.

[28] S. R. Mousavi, H. Rivaz, A. Sadeghi-Naini, G. J. Czarnota, and A. Samani, "Breast ultrasound elastography using full inversion-based elastic modulus reconstruction," *IEEE Transactions on Computational Imaging*, vol. 3, no. 4, pp. 774–782, 2017.

[29] A. Bruhn, J. Weickert, and C. Schnörr, "Lucas/kanade meets horn/schunck: Combining local and global optic flow methods," *International journal of computer vision*, vol. 61, no. 3, pp. 211–231, 2005.

[30] A. Zayed and H. Rivaz, "Fast approximate time-delay estimation in ultrasound elastography using principal component analysis," in *2019 41st Annual International Conference of the IEEE Engineering in Medicine and Biology Society (EMBC)*, pp. 6204–6207, IEEE, 2019.

[31] J. Wulff and M. J. Black, "Efficient sparse-to-dense optical flow estimation using a learned basis and layers," in *Proceedings of the IEEE Conference on Computer Vision and Pattern Recognition*, pp. 120–130, 2015.

[32] R. M. Pohlman and T. Varghese, "Dictionary representations for electrode displacement elastography," *IEEE transactions on ultrasonics, ferroelectrics, and frequency control*, vol. 65, no. 12, pp. 2381–2389, 2018.

[33] H. S. Hashemi and H. Rivaz, "Global time-delay estimation in ultrasound elastography," *IEEE transactions on ultrasonics, ferroelectrics, and frequency control*, vol. 64, no. 10, pp. 1625–1636, 2017.

[34] D. Sun, X. Yang, M.-Y. Liu, and J. Kautz, "Pwc-net: Cnns for optical flow using pyramid, warping, and cost volume," in *Proceedings of the IEEE Conference on Computer Vision and Pattern Recognition*, pp. 8934–8943, 2018.

[35] A. Dosovitskiy, P. Fischer, E. Ilg, P. Hausser, C. Hazirbas, V. Golkov, P. Van Der Smagt, D. Cremers, and T. Brox, "Flownet: Learning optical flow with convolutional networks," in *Proceedings of the IEEE international conference on computer vision*, pp. 2758–2766, 2015.

[36] A. Ranjan and M. J. Black, "Optical flow estimation using a spatial pyramid network," in *Proceedings of the IEEE Conference on Computer Vision and Pattern Recognition*, pp. 4161–4170, 2017.

[37] M. G. Kibria and H. Rivaz, "Gluenet: ultrasound elastography using convolutional neural network," in *Simulation, Image Processing, and Ultrasound Systems for Assisted Diagnosis and Navigation*, pp. 21–28, Springer, 2018.

[38] A. K. Tehrani and H. Rivaz, "Displacement estimation in ultrasound elastography using pyramidal convolutional neural network," *IEEE Transactions on Ultrasonics, Ferroelectrics, and Frequency Control*, 2020.

[39] R. M. Sigrist, J. Liau, A. El Kaffas, M. C. Chammas, and J. K. Willmann, "Ultrasound elastography: review of techniques and clinical applications," *Theranostics*, vol. 7, no. 5, p. 1303, 2017.

[40] Y. Hong, X. Liu, Z. Li, X. Zhang, M. Chen, and Z. Luo, "Real-time ultrasound elastography in the differential diagnosis of benign and malignant thyroid nodules," *Journal of Ultrasound in Medicine*, vol. 28, no. 7, pp. 861–867, 2009.

[41] P. Trimboli, R. Guglielmi, S. Monti, I. Misischi, F. Graziano, N. Nasrollah, S. Amendola, S. N. Morgante, M. G. Deiana, S. Valabrega, *et al.*, "Ultrasound sensitivity for thyroid malignancy is increased by real-time elastography: a prospective multicenter study," *The Journal of Clinical Endocrinology & Metabolism*, vol. 97, no. 12, pp. 4524–4530, 2012.

[42] A. E. Samir, M. Dhyani, A. Anvari, J. Prescott, E. F. Halpern, W. C. Faquin, and A. Stephen, "Shear-wave elastography for the preoperative risk stratification of follicular-patterned lesions of the thyroid: diagnostic accuracy and optimal measurement plane," *Radiology*, vol. 277, no. 2, pp. 565–573, 2015.

[43] T. J. Hall, Y. Zhu, C. S. Spalding, and L. T. Cook, "In vivo results of real-time freehand elasticity imaging," in *2001 IEEE Ultrasonics Symposium. Proceedings. An International Symposium (Cat. No. 01CH37263)*, vol. 2, pp. 1653–1657, IEEE, 2001.

[44] M. M. Doyley, J. C. Bamber, F. Fuechsel, and N. L. Bush, "A freehand elastographic imaging approach for clinical breast imaging: system development and performance evaluation," *Ultrasound in medicine & biology*, vol. 27, no. 10, pp. 1347–1357, 2001.

[45] N. Uniyal, H. Eskandari, P. Abolmaesumi, S. Sojoudi, P. Gordon, L. Warren, R. N. Rohling, S. E. Salcudean, and M. Moradi, "Ultrasound rf time series for classification of breast lesions," *IEEE transactions on medical imaging*, vol. 34, no. 2, pp. 652–661, 2015.

[46] H. Rivaz, E. M. Boctor, M. A. Choti, and G. D. Hager, "Ultrasound elastography using multiple images," *Medical image analysis*, vol. 18, no. 2, pp. 314–329, 2014.

[47] W. Yang, M. Alexander, N. Rubert, A. Ingle, M. Lubner, T. Ziemlewicz, J. Hinshaw, F. Lee, J. Zagzebski, and T. Varghese, "Monitoring microwave ablation for liver tumors with electrode displacement strain imaging," in *2014 IEEE International Ultrasonics Symposium*, pp. 1128–1131, IEEE, 2014.

[48] N. Frulio and H. Trillaud, "Ultrasound elastography in liver," *Diagnostic and interventional imaging*, vol. 94, no. 5, pp. 515–534, 2013.

[49] S. Selladurai and A. K. Thittai, "Towards quantitative quasi-static ultrasound elastography using a reference layer for liver imaging application: A preliminary assessment," *Ultrasonics*, vol. 93, pp. 7–17, 2019.

[50] M. Friedrich-Rust, M.-F. Ong, S. Martens, C. Sarrazin, J. Bojunga, S. Zeuzem, and E. Herrmann, "Performance of transient elastography for the staging of liver fibrosis: a meta-analysis," *Gastroenterology*, vol. 134, no. 4, pp. 960–974, 2008.

[51] E. Tsochatzis, K. Gurusamy, S. Ntaoula, E. Cholongitas, B. Davidson, and A. Burroughs, "Elastography for the diagnosis of severity of fibrosis in chronic liver disease: a meta-analysis of diagnostic accuracy," *Journal of hepatology*, vol. 54, no. 4, pp. 650–659, 2011.

[52] A. Lorenz, H. Sommerfeld, M. Garcia-Schurmann, S. Philippou, T. Senge, and H. Ermert, "A new system for the acquisition of ultrasonic multicompression strain images of the human prostate in vivo," *IEEE transactions on ultrasonics, ferroelectrics, and frequency control*, vol. 46, no. 5, pp. 1147–1154, 1999.

[53] J. Correas, E. Drakonakis, A. Isidori, O. Hélénon, C. Pozza, V. Cantisani, N. Di Leo, F. Maghella, A. Rubini, F. Drudi, *et al.*, "Update on ultrasound elastography: miscellanea. prostate, testicle, musculo-skeletal," *European journal of radiology*, vol. 82, no. 11, pp. 1904–1912, 2013.

[54] A. Sãftoiu and P. Vilman, "Endoscopic ultrasound elastography-a new imaging technique for the visualization of tissue elasticity distribution," *Journal of Gastrointestinal and Liver Diseases*, vol. 15, no. 2, p. 161, 2006.

[55] T. Selbekk, J. Bang, and G. Unsgaard, "Strain processing of intraoperative ultrasound images of brain tumours: initial results," *Ultrasound in medicine & biology*, vol. 31, no. 1, pp. 45–51, 2005.

[56] T. Selbekk, R. Brekken, O. Solheim, S. Lydersen, T. A. Hernes, and G. Unsgaard, "Tissue motion and strain in the human brain assessed by intraoperative ultrasound in glioma patients," *Ultrasound in medicine & biology*, vol. 36, no. 1, pp. 2–10, 2010.

[57] M. Mirzaei, A. Asif, M. Fortin, and H. Rivaz, "3d normalized cross-correlation for estimation of the displacement field in ultrasound elastography," *Ultrasonics*, vol. 102, p. 106053, 2020.

[58] X. Pan, K. Liu, J. Shao, J. Gao, L. Huang, J. Bai, and J. Luo, "Performance comparison of rigid and affine models for motion estimation using ultrasound radio-frequency signals," *IEEE transactions on ultrasonics, ferroelectrics, and frequency control*, vol. 62, no. 11, pp. 1928–1943, 2015.

[59] T. Varghese, E. Konofagou, J. Ophir, S. Alam, and M. Bilgen, "Direct strain estimation in elastography using spectral cross-correlation," *Ultrasound in medicine & biology*, vol. 26, no. 9, pp. 1525–1537, 2000.

[60] R. Zahiri-Azar and S. E. Salcudean, "Motion estimation in ultrasound images using time domain cross correlation with prior estimates.," *IEEE Trans. Biomed. Engineering*, vol. 53, no. 10, pp. 1990–2000, 2006.

[61] J. Wang, Q. Huang, and X. Zhang, "Ultrasound elastography based on the normalized cross-correlation and the pso algorithm," in *Systems and Informatics (ICSAI), 2017 4th International Conference on*, pp. 1131–1135, IEEE, 2017.

[62] X. Chen, M. J. Zohdy, S. Y. Emelianov, and M. O'Donnell, "Lateral speckle tracking using synthetic lateral phase," *IEEE transactions on ultrasonics, ferroelectrics, and frequency control*, vol. 51, no. 5, pp. 540–550, 2004.

[63] L. Yuan and P. C. Pedersen, "Analytical phase-tracking-based strain estimation for ultrasound elasticity," *IEEE transactions on ultrasonics, ferroelectrics, and frequency control*, vol. 62, no. 1, pp. 185–207, 2015.

[64] P. Chaturvedi, M. F. Insana, and T. J. Hall, "Testing the limitations of 2-d companding for strain imaging using phantoms," *IEEE transactions on ultrasonics, ferroelectrics, and frequency control*, vol. 45, no. 4, pp. 1022–1031, 1998.

[65] L. Zhang, N. Snavely, B. Curless, and S. M. Seitz, "Spacetime faces: High-resolution capture for modeling and animation," in *Data-Driven 3D Facial Animation*, pp. 248–276, Springer, 2008.

[66] I. Céspedes, Y. Huang, J. Ophir, and S. Spratt, "Methods for estimation of subsample time delays of digitized echo signals," *Ultrasonic imaging*, vol. 17, no. 2, pp. 142–171, 1995.

[67] J. Jiang and T. J. Hall, "A coupled subsample displacement estimation method for ultrasound-based strain elastography," *Physics in Medicine & Biology*, vol. 60, no. 21, p. 8347, 2015.

[68] R. Z. Azar, O. Goksel, and S. E. Salcudean, "Sub-sample displacement estimation from digitized ultrasound rf signals using multi-dimensional polynomial fitting of the cross-correlation function," *IEEE transactions on ultrasonics, ferroelectrics, and frequency control*, vol. 57, no. 11, pp. 2403–2420, 2010.

[69] M. T. Islam, A. Chaudhry, and R. Righetti, "A robust method to estimate the time constant of elastographic parameters," *IEEE transactions on medical imaging*, vol. 38, no. 6, pp. 1358–1370, 2019.

[70] M. Sridhar and M. F. Insana, "Ultrasonic measurements of breast viscoelasticity," *Medical physics*, vol. 34, no. 12, pp. 4757–4767, 2007.

[71] K. Nightingale, M. S. Soo, R. Nightingale, and G. Trahey, "Acoustic radiation force impulse imaging: in vivo demonstration of clinical feasibility," *Ultrasound in medicine & biology*, vol. 28, no. 2, pp. 227–235, 2002.

[72] E. Turgay, S. Salcudean, and R. Rohling, "Identifying the mechanical properties of tissue by ultrasound strain imaging," *Ultrasound in medicine & biology*, vol. 32, no. 2, pp. 221–235, 2006.

[73] J. A. Jensen and N. B. Svendsen, "Calculation of pressure fields from arbitrarily shaped, apodized, and excited ultrasound transducers," *IEEE transactions on ultrasonics, ferroelectrics, and frequency control*, vol. 39, no. 2, pp. 262–267, 1992.

[74] M. Mirzaei, A. Asif, and H. Rivaz, "Combining total variation regularization with window-based time delay estimation in ultrasound elastography," *IEEE transactions on medical imaging*, vol. 38, no. 12, pp. 2744–2754, 2019.

[75] T. J Hall, P. E Barboneg, A. A Oberai, J. Jiang, J.-F. Dord, S. Goenezen, and T. G Fisher, "Recent results in nonlinear strain and modulus imaging," *Current medical imaging reviews*, vol. 7, no. 4, pp. 313–327, 2011.

[76] C. Pellot-Barakat, F. Frouin, M. F. Insana, and A. Herment, "Ultrasound elastography based on multiscale estimations of regularized displacement fields," *IEEE transactions on medical imaging*, vol. 23, no. 2, pp. 153–163, 2004.

[77] E. Brusseau, J. Kybic, J.-F. Déprez, and O. Basset, "2-d locally regularized tissue strain estimation from radio-frequency ultrasound images: Theoretical developments and results on experimental data," *IEEE Transactions on Medical Imaging*, vol. 27, no. 2, pp. 145–160, 2008.

[78] H. Rivaz, E. Boctor, P. Foroughi, R. Zellars, G. Fichtinger, and G. Hager, "Ultrasound elastography: a dynamic programming approach," *IEEE transactions on medical imaging*, vol. 27, no. 10, pp. 1373–1377, 2008.

[79] A. Kuzmin, A. M. Zakrzewski, B. W. Anthony, and V. Lempitsky, "Multiframe elastography using a handheld force-controlled ultrasound probe," *IEEE transactions on ultrasonics, ferroelectrics, and frequency control*, vol. 62, no. 8, pp. 1486–1500, 2015.

[80] L. Guo, Y. Xu, Z. Xu, and J. Jiang, "A pde-based regularization algorithm toward reducing speckle tracking noise: A feasibility study for ultrasound breast elastography," *Ultrasonic imaging*, vol. 37, no. 4, pp. 277–293, 2015.

[81] X. Pan, J. Gao, S. Tao, K. Liu, J. Bai, and J. Luo, "A two-step optical flow method for strain estimation in elastography: Simulation and phantom study," *Ultrasonics*, vol. 54, no. 4, pp. 990–996, 2014.

[82] M. Ashikuzzaman, C. J. Gauthier, and H. Rivaz, "Global ultrasound elastography in spatial and temporal domains," *IEEE transactions on ultrasonics, ferroelectrics, and frequency control*, vol. 66, no. 5, pp. 876–887, 2019.

[83] J. Weickert and C. Schnörr, "A theoretical framework for convex regularizers in pde-based computation of image motion," *International Journal of Computer Vision*, vol. 45, no. 3, pp. 245–264, 2001.

[84] Y. Wang, E. Helminen, and J. Jiang, "Building a virtual simulation platform for quasistatic breast ultrasound elastography using open source software: A preliminary investigation," *Medical physics*, vol. 42, no. 9, pp. 5453–5466, 2015.

[85] M. Mirzaei, A. Asif, and H. Rivaz, "Accurate and precise time-delay estimation for ultrasound elastography with pre-beamformed channel data," *IEEE Transactions on Ultrasonics, Ferroelectrics, and Frequency Control*, 2020.

[86] M. Mirzaei, A. Asif, and H. Rivaz, "Ultrasound elastography utilizing pre-beamformed data," in *2019 IEEE 16th International Symposium on Biomedical Imaging (ISBI 2019)*, pp. 1725–1728, IEEE, 2019.

[87] C. E. Shannon, "Communication in the presence of noise," *Proceedings of the IEEE*, vol. 86, no. 2, pp. 447–457, 1998.

[88] W. Long, N. Bottenus, and G. E. Trahey, "Lag-one coherence as a metric for ultrasonic image quality," *IEEE transactions on ultrasonics, ferroelectrics, and frequency control*, vol. 65, no. 10, pp. 1768–1780, 2018.

[89] M. A. Kutay, A. P. Petropulu, and C. W. Piccoli, "On modeling biomedical ultrasound rf echoes using a power-law shot-noise model," *IEEE transactions on ultrasonics, ferroelectrics, and frequency control*, vol. 48, no. 4, pp. 953–968, 2001.

[90] T. Varghese and J. Ophir, "An analysis of elastographic contrast-to-noise ratio," *Ultrasound in medicine & biology*, vol. 24, no. 6, pp. 915–924, 1998.

[91] M. Mirzaei, A. Asif, and H. Rivaz, "Virtual source synthetic aperture for accurate lateral displacement estimation in ultrasound elastography," *IEEE Transactions on Ultrasonics, Ferroelectrics, and Frequency Control*, 2020.

[92] A. K. Tehrani, M. Mirzaei, and H. Rivaz, "Semi-supervised training of optical flow convolutional neural networks in ultrasound elastography," in *International Conference on Medical Image Computing and Computer-Assisted Intervention*, pp. 504–513, Springer, 2020.

[93] J. Luo and E. E. Konofagou, "Effects of various parameters on lateral displacement estimation in ultrasound elastography," *Ultrasound in medicine & biology*, vol. 35, no. 8, pp. 1352–1366, 2009.

[94] Q. He, L. Tong, L. Huang, J. Liu, Y. Chen, and J. Luo, "Performance optimization of lateral displacement estimation with spatial angular compounding," *Ultrasonics*, vol. 73, pp. 9–21, 2017.

[95] E. Konofagou and J. Ophir, "A new elastographic method for estimation and imaging of lateral displacements, lateral strains, corrected axial strains and poisson's ratios in tissues," *Ultrasound in medicine & biology*, vol. 24, no. 8, pp. 1183–1199, 1998.

[96] Z. Liu, C. Huang, and J. Luo, "A systematic investigation of lateral estimation using various interpolation approaches in conventional ultrasound imaging," *IEEE transactions on ultrasonics, ferroelectrics, and frequency control*, vol. 64, no. 8, pp. 1149–1160, 2017.

[97] E. S. Ebbini, "Phase-coupled two-dimensional speckle tracking algorithm," *IEEE transactions on ultrasonics, ferroelectrics, and frequency control*, vol. 53, no. 5, pp. 972–990, 2006.

[98] S. Korukonda and M. M. Doyley, "Estimating axial and lateral strain using a synthetic aperture elastographic imaging system," *Ultrasound in medicine & biology*, vol. 37, no. 11, pp. 1893–1908, 2011.

[99] S. Korukonda, R. Nayak, N. Carson, G. Schifitto, V. Dogra, and M. M. Doyley, "Noninvasive vascular elastography using plane-wave and sparse-array imaging," *IEEE transactions on ultrasonics, ferroelectrics, and frequency control*, vol. 60, no. 2, pp. 332–342, 2013.

[100] R. Nayak, S. Huntzicker, J. Ohayon, N. Carson, V. Dogra, G. Schifitto, and M. M. Doyley, "Principal strain vascular elastography: Simulation and preliminary clinical evaluation," *Ultrasound in medicine & biology*, vol. 43, no. 3, pp. 682–699, 2017.

[101] J. Luo and E. E. Konofagou, "Fundamental analysis of lateral displacement estimation quality in ultrasound elastography," in *2009 IEEE International Symposium on Biomedical Imaging: From Nano to Macro*, pp. 462–465, IEEE, 2009.

[102] J. Luo and E. E. Konofagou, "Key parameters for precise lateral displacement estimation in ultrasound elastography," in *2009 Annual International Conference of the IEEE Engineering in Medicine and Biology Society*, pp. 4407–4410, IEEE, 2009.

[103] C. H. Frazier and W. D. O'Brien, "Synthetic aperture techniques with a virtual source element," *IEEE transactions on ultrasonics, ferroelectrics, and frequency control*, vol. 45, no. 1, pp. 196–207, 1998.

[104] C. Passmann and H. Ermert, "A 100-mhz ultrasound imaging system for dermatologic and ophthalmologic diagnostics," *IEEE transactions on ultrasonics, ferroelectrics, and frequency control*, vol. 43, no. 4, pp. 545–552, 1996.

[105] N. Bottenus, B. C. Byram, J. J. Dahl, and G. E. Trahey, "Synthetic aperture focusing for short-lag spatial coherence imaging," *IEEE transactions on ultrasonics, ferroelectrics, and frequency control*, vol. 60, no. 9, pp. 1816–1826, 2013.

[106] U. Techavipoo, Q. Chen, T. Varghese, and J. A. Zagzebski, "Estimation of displacement vectors and strain tensors in elastography using angular insonifications," *IEEE transactions on medical imaging*, vol. 23, no. 12, pp. 1479–1489, 2004.

[107] M. Tanter, J. Bercoff, L. Sandrin, and M. Fink, "Ultrafast compound imaging for 2-d motion vector estimation: Application to transient elastography," *IEEE transactions on ultrasonics, ferroelectrics, and frequency control*, vol. 49, no. 10, pp. 1363–1374, 2002.

[108] A. R. Skovoroda, M. A. Lubinski, S. Y. Emelianov, and M. O'Donnell, "Nonlinear estimation of the lateral displacement using tissue incompressibility," *IEEE transactions on ultrasonics, ferroelectrics, and frequency control*, vol. 45, no. 2, pp. 491–503, 1998.

[109] D. T. Seidl, A. A. Oberai, and P. E. Barbone, "The coupled adjoint-state equation in forward and inverse linear elasticity: Incompressible plane stress," *Computer Methods in Applied Mechanics and Engineering*, vol. 357, p. 112588, 2019.

[110] E. J. Chen, J. Novakofski, W. K. Jenkins, and W. D. O'Brien, "Young's modulus measurements of soft tissues with application to elasticity imaging," *IEEE Transactions on ultrasonics, ferroelectrics, and frequency control*, vol. 43, no. 1, pp. 191–194, 1996.

[111] J. A. Jensen, "Field: A program for simulating ultrasound systems," in *10th nordicbaltic conference on biomedical imaging, vol.4, supplement 1, part 1: 351–353*, Citeseer, 1996.

[112] R. Righetti, J. Ophir, and P. Ktonas, "Axial resolution in elastography," *Ultrasound in medicine & biology*, vol. 28, no. 1, pp. 101–113, 2002.

[113] J. Luo and E. E. Konofagou, "A fast normalized cross-correlation calculation method for motion estimation," *IEEE transactions on ultrasonics, ferroelectrics, and frequency control*, vol. 57, no. 6, pp. 1347–1357, 2010.

[114] A. Zayed and H. Rivaz, "Fast strain estimation and frame selection in ultrasound elastography using machine learning," *IEEE transactions on ultrasonics, ferroelectrics, and frequency Control*, 2021.

[115] M. Sharifzadeh, H. Benali, and H. Rivaz, "Phase aberration correction: A convolutional neural network approach," *IEEE Access*, vol. 8, pp. 162252–162260, 2020.